ADAPTIVE IMAGE INTERPOLATION AND APPLICATIONS

ADAPTIVE IMAGE INTERPOLATION AND APPLICATIONS

By

XIANGJUN ZHANG, B.Eng., M.Eng.

A Thesis

Submitted to the School of Graduate Studies

In Partial Fulfilment of the Requirements

for the Degree

Doctor of Philosophy

McMaster University

DOCTOR OF PHILOSOPHY (2009) McMaster University
(Electrical and Computer Engineering) Hamilton, Ontario

TITLE: Adaptive Image Interpolation and Applications

AUTHOR: Xiangjun Zhang
B.Eng., (Electrical Engineering)
Xi'an Jiaotong University, Xi'an, China
M.Eng, (Electrical Engineering)
Tsinghua University, Beijing, China

SUPERVISOR: Dr. Xiaolin Wu

NUMBER OF PAGES: xv, 141

Abstract

In this thesis we systematically reexamine the classical problem of image interpolation with an aim to better preserve the structural information, such as edges and textures, in the interpolated image. We take on the technical challenge of faithfully reconstructing high frequency components because this is critical to the perceptual quality. To achieve the above goal we develop three new adaptive image interpolation methods: 1) a classification-based method that is driven by contextual information of the low resolution image and the prior knowledge extracted from a training set of high resolution images; 2) An adaptive soft-decision block estimation method that learns and adapts to varying scene structures, guided by a two-dimension piecewise autoregressive model; 3) A model-based non-linear image restoration scheme in which the model parameters and high resolution pixels are jointly estimated through non-linear least squares estimation.

The latter part of this thesis is devoted to the research of interpolation-based image compression, which is a relatively new topic. Our research is motivated by two important applications of visual communication: low bit-rate image coding and multiple description coding. We succeed in developing standard-compliant interpolation-based compression techniques for the above two applications. In their respective categories, these techniques exceed the best rate-distortion performance reported so far in the literature.

Acknowledgement

I would like to take this opportunity to thank all those who have made the completion of this thesis possible.

First and foremost, I would like to express my appreciation to my supervisor Dr. Xiaolin Wu. This thesis would not have been possible without his guidance, encouragement and patience.

Special thanks to my supervisory committee members: Dr. S. Shirani and Dr. S. Sirouspour, for their valuable feedbacks. I would also like to thank Dr. E. Younglai and Dr. W. El-dakhakhni for being on my examination committee and Dr. W. Lin for being my external examiner.

My gratitude particularly goes to my colleagues Xiaohan, Zhe, Lei, Ning, Ting, Mingkai, Huazhong, Amin, Reza, and Ali. Their help and friendship have made my Ph.D study a happy experience. Also, I would like to acknowledge Cheryl, Helen, Cosmin and Terry for their friendly assistance and expert technical support.

Last but not least, I would like to express my grateful thanks to my father, my mother and my husband, Kai. Thank you for your unconditional love and support.

Contents

List of Figures

List of Tables

List of Abbreviations

2D	Two-dimension
AR	Autoregressive
ARMA	Autoregressive moving average
bpp	bit per pixel
CADU	Collaborative adaptive down-sampling and upconversion
CADU-JPG	CADU method coupled with DCT-based JPEG
CADU-J2K	CADU method coupled with JPEG 2000
CALIC	Context-based adaptive lossless codec [1]
CCD	Charged couple device
CMOS	Multiple Description Lattice Vector Quantization
dB	Decibel
DCT	Discrete cosine transform
dpi	Dot per inch
FIR	Finite impulse response
HR	High resolution
JPEG	Joint photographic experts group
JPEG 2000	A compression standard by JPEG [2]
KFD	Kernel fisher discriminant
LR	Low resolution

MA	Moving average
MD	Multiple description
MDC	Multiple description coding
MMSE	Minimum mean square error
NEDI	New edge directed interpolation [3]
NEARU	Non-linear estimation for adaptive resolution upconversion
PAR	Piecewise autoregressive
POCS	Projection onto convex sets
PSF	Point spread function
PSNR	Peak signal-to-noise ratio
SAI	Soft-decision adaptive interpolation
SMMD	Spatial multiplexing multiple description
SNR	Signal-to-noise ratio
STLS	Structure total least square
TMW	A lossless compression method in [4]
TOM	Texture orientation map

Chapter 1

Introduction

1.1 The Problem and Motivation

Digital images have, in both still and moving forms, become a main medium of information, knowledge, and communication in our modern technology era. People in all walks of life now truly appreciate the connotation of the old saying "a picture is worth a thousand words". Many may find digital images/videos too informative, too convenient, too timely and too rich to do without. Compared to their counterparts on paper and film, digital images are vastly more convenient and inexpensive to generate, communicate, process, store and retrieve. With intensive research and heavy investment in sensor technologies, the spatial resolution and color fidelity of digital images are steadily improving and now can match those of traditional film.

One of the most important quality metrics of digital images is and will continue to be the spatial resolution. High spatial resolution is necessary to reveal fine structural information on the imaged objects and scenes. High resolution directly translates to high precision in computerized image analysis, which is paramount in medical, scientific and military applications. Even in consumer electronics, entertainment industry, and other commercial applications, users desire high image resolution because resolution is in general proportional to perceived image quality. To appreciate this

the reader is invited to compare two images of the same scene but of different spatial resolutions in Fig. 1.1.

In an ideal world, one can always increase the sensor resolution of image acquisition devices to obtain a desired spatial resolution. However, several limiting factors nullify this approach. First, the cost of image sensors increases drastically in resolution. For instance, in today's consumer market, digital cameras of ten million pixels typically cost more than twice as much as those of seven million pixels. Second, there exist hard physical limits on how high a spatial resolution that an imaging device can achieve. Most digital images are acquired by an array of semiconductor sensors such as charged couple device (CCD) or complementary metal-oxide-semiconductor (CMOS). Ultra-high spatial resolution means that the size of pixel (i.e., the cross section of a sensor area) diminishes. However, the signal-to-noise ratio (SNR) of the acquired image is proportional to its size [5]. Too small a pixel will render an image useless due to insufficient SNR. Moreover, electronic interferences are inevitable between neighboring sensors. The closer the neighboring sensors are, the larger the interference become. Therefore, given an SNR requirement, either the size of the sensor or the distance between neighboring sensors can not be below a hard threshold. Third, in some cases the imaging process itself incurs a penalty to the imaged object, which limits the number of samples (pixels) to be acquired. For example, for certain medical imaging technologies, high resolution is associated with large dosage of radiation that is harmful to the patient. Finally, no matter how high the native sensor resolution of an imaging device is, new, more exciting or more exotic applications will always present themselves that demand even higher spatial resolution. As one can imagine, researchers in medicine, space, and sciences all have insatiable appetite for imaging ever more minuscule details. This is even the case for more mundane application of digital photo finishing. Nowadays the resolution of photo printers can be 2400 dot per inch (dpi) or higher. Even for inexpensive home printers of a resolution of 1200 dpi, a photo print of size 4 inch by 6 inch contains $4 \times 1200 \times 6 \times 1200 = 34$ million

(a) Low resolution

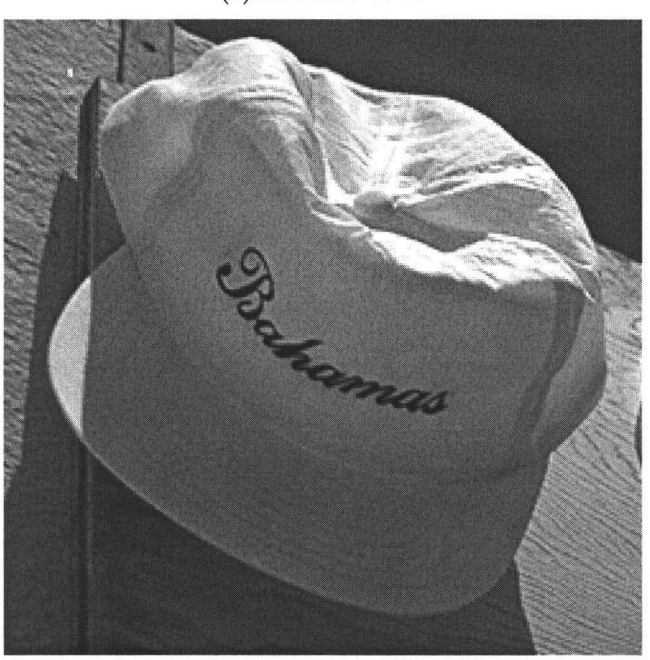

(b) High resolution

Figure 1.1: Images with different resolutions

pixels, which far exceeds the resolution of even most expensive professional digital cameras.

Image interpolation, or image resolution upconversion, is a technology to improve the native sensor resolution by reconstructing an image of higher resolution from a lower resolution version. Interpolation of a discrete signal is a classic problem in applied mathematics and signal processing. The goal is to reconstruct a continuous function from a set of discrete data (samples). A digital signal is typically generated by sampling the corresponding continuous signal in space or time. A digital image of different resolutions corresponds to different sampling schemes of the same continuous signal. To increase the resolution, the interpolation is performed to estimate the continuous image signal from the observed low resolution image. The high resolution image can then be obtained by re-sampling the continuous image signal. In this thesis, we focus on the interpolation problem of recovering a high resolution (HR) image from its associated low resolution (LR) image.

The challenge to image interpolation is the reconstruction of high frequency components of an image, such as edges and fine textures. Low frequency components of an HR image can be recovered from a corresponding LR image more easily than the high frequency components. According to Nyquist sampling theory [6], only those components that have frequency below the Nyquist frequency can be exactly reconstructed. All interpolation methods can do a comparable good job in reconstructing smooth two-dimension (2D) waveforms. It is the interpolation accuracy on spatial structures of high frequency that differentiates the good image interpolation methods from the poor ones. Inferior interpolation methods are prone to artifacts in the areas of edges and fine textures. The common visual defects due to interpolation errors are blurred or/and jaggy edges and aliasing. To aggravate the difficulty of reconstructing edges, the human vision system is highly sensitive to noises accompanying edges. This is because edges convey much of the image semantics. Edges signify vital attributes of an object such as shape, size, and surface characteristics, as well as spatial relation-

ship between the objects. As a result, small amount of errors in reconstructing edges can disproportionably degrade the visual quality of the entire image. Fig. 1.2 shows such an example. The two images in the figure are the interpolation results of two different methods: Bicubic interpolation [7] and soft-decision adaptive interpolation [8]. Fig. 1.2(b) is visually far more pleasing than Fig. 1.2(a) with edges faithfully reconstructed without jaggies. Therefore, the key and determining factor for interpolation performance is how well edges and other high frequency image constructs can be preserved.

Image interpolation technology has a wide range of applications spanning from consumer electronics to visual arts and to cutting edge medical and scientific research. Familiar examples can be found in our surroundings: the reproduction of images captured by digital cameras for high quality prints (e.g., those in magazines, catalogs, posters, or office/home decorations), and the upconversion of standard-definition video frames for playback on high-definition television receivers and computer monitors. In addition to its role in image enhancement to please our eyes, image interpolation is an indispensable enabling technology in computer vision, surveillance, medical imaging, remote sensing, and other fields, whenever the desired measurement precision exceeds the sensor resolution.

In this thesis we also investigate a relatively new and important application of image interpolation: low bit-rate image and video compression. In some modern information technology areas, such as wireless multimedia communication and sensor networks, the communication bandwidth is at a premium. The image/video signals have to be coded and transmitted at low bit rates. However, the existing image/video compression standards can cause severe image quality degradation, such as blurring, jaggies, or/and blocking artifacts when the bit budget is too low. Such an example is shown in Fig. 1.3, where Fig. 1.3(b) is the compressed version of Fig. 1.3(a) by JPEG 2000 standard [2] at 0.2 bpp. One technique to alleviate the compression artifacts is to down sample an image before compression at the encoder. The decoder employs image

(a) Bicubic interpolation

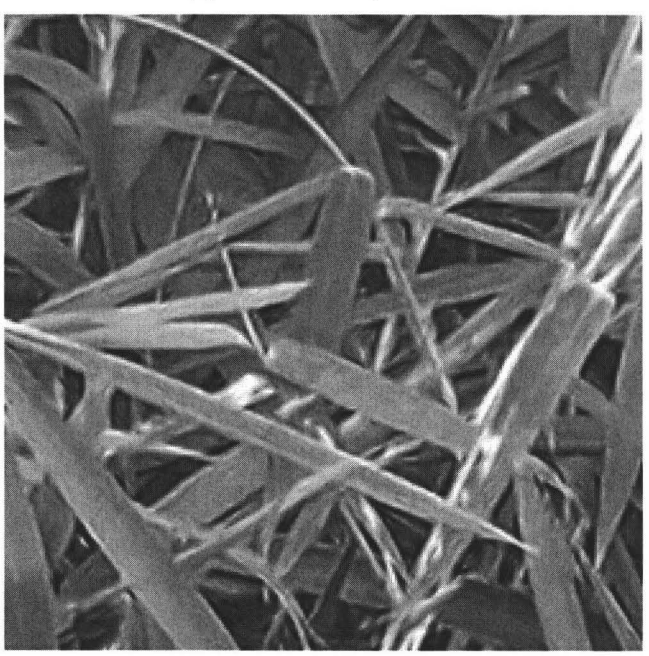

(b) Soft-decision adaptive interpolation

Figure 1.2: Images interpolated by different methods.

(a) Original image

(b) Compressed by JPEG 2000

Figure 1.3: Original image and the compressed version at 0.2 bpp.

interpolation to upconvert the decompressed image back to the original resolution.

Image interpolation can also be used as a technique for multiple description coding (MDC) of images. MDC is an effective methodology for signal communication over unreliable diversity channels, to which a great deal of research efforts have been devoted in the past decade. In image MDC an input image is encoded into several bit streams or multiple descriptions and transmitted through independent lossy channels. The decoder can reconstruct the original image if any subset of the transmitted descriptions can be received. The more descriptions arrive at the decoder, the higher the reconstruction quality. A straightforward way of generating multiple descriptions of an image is to spatially partition the image into two or more subimages. An example of this spatial multiplexing scheme is shown in Fig. 1.4. In the figure, four descriptions are generated by uniformly down-sampling the original image. Each description is a LR version of the original image. When any descriptions are lost, the decoder has to reconstruct the original image from the received descriptions (LR images), which is exactly an interpolation problem.

1.2 Contributions

In this thesis, we developed three new adaptive interpolation methods with a main design objective of preserving the spatial structures of edges and textures. Our design principle is motivated by the importance of edges and textures in image semantics and perceptual visual quality, as mentioned above. We have implemented these methods and carried out extensive experiments to evaluate their merits and limits in comparison with the existing techniques. We present convincing evidence that the proposed new techniques outperform their predecessors in both perceptual quality and objective measure. We also investigate the use of image interpolation techniques in low bit-rate image compression and in multiple description image coding, and obtain promising results for these two applications of visual communication. The original contributions

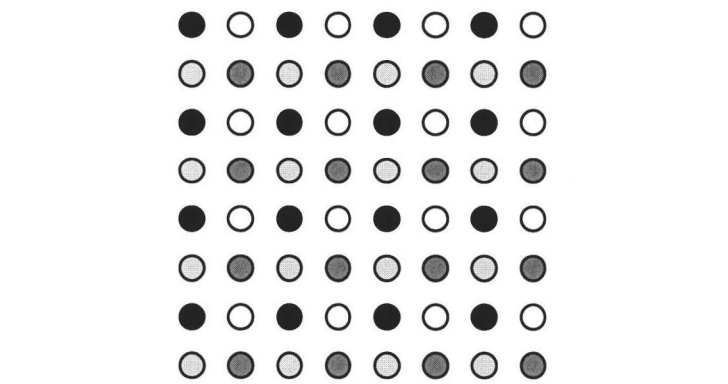

(a) Original Image

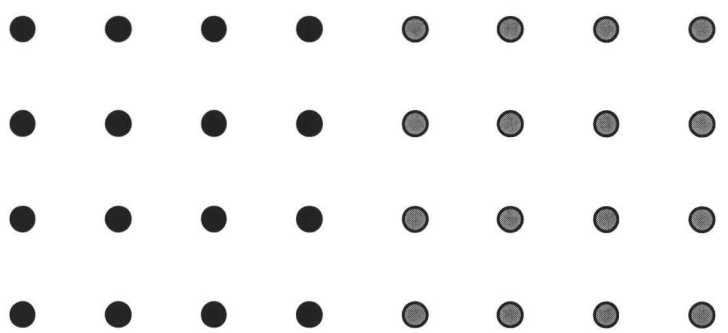

(b) Description 1

(c) Description 2

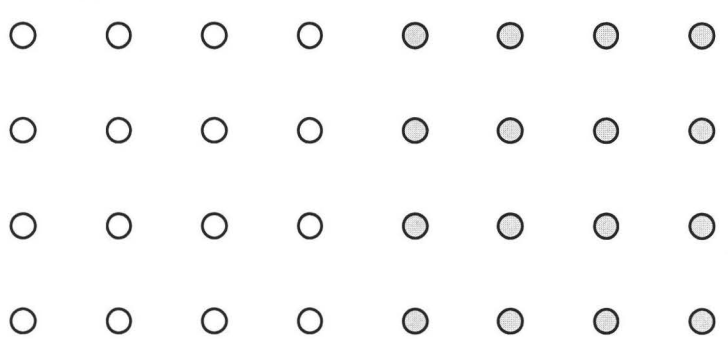

(d) Description 3

(e) Description 4

Figure 1.4: Generating four descriptions by spatially multiplexing.

of this thesis are summarized as follows.

- A new adaptive non-linear image interpolation approach is proposed that chooses an interpolation direction based on contextual information of the LR image. The selection of the best interpolation direction among all possible candidate directions is converted to a classification problem. The classifier is designed using a training set of HR images. This new classification-based method achieves higher peak signal-to-noise ratio (PSNR) and better visual quality than previous methods. It can correctly solve some of the very difficult cases for which the traditional methods fail.

- Our second new image interpolation technique is called soft-decision adaptive interpolation (SAI). The SAI technique learns and adapts to varying scene structures using a 2D piecewise autoregressive model. The model parameters are estimated in a moving window in the input low resolution image. And the pixel structure dictated by the learnt model is enforced by the soft-decision estimation process onto a block of HR pixels, including both observed and estimated. This new image interpolation technique produces some of the best results so far by preserving spatial coherence of interpolated images better than the existing methods.

- Our third new, the most sophisticated image interpolation technique is a model-based non-linear image restoration scheme. The task of image resolution upconversion is formulated as a problem of adaptive piecewise autoregressive modeling and estimation, where the model parameters and the HR pixels are jointly estimated through non-linear least squares estimation. The new method offers a unified general framework for image upsampling and deconvolution, and the upsampling can be carried out at an arbitrary scale. The method outperforms convincingly the current methods in both PSNR and subjective visual quality, and its advantage becomes greater for larger scaling factors.

- We investigate the use of image interpolation as a technique for low bit-rate image compression, and propose a collaborative adaptive down-sampling and upconversion (CADU) approach to image compression. In this approach, the input images are adaptively prefiltered, uniformly down sampled, and compressed at the encoder. The decoder upconverts the decoded LR images to the original resolution in a constrained least squares restoration process, using a 2D piecewise autoregressive model and the knowledge of directional low-pass prefiltering. The CADU approach achieves the highest PSNR and best visual quality up to now for low bit rates, and it is completely compatible with any existing compression standards.

- We are among the first to study the application of image interpolation in multiple description image coding. Our contribution to this new subject is a spatial multiplexing multiple description (SMMD) scheme. Multiple descriptions of an image are generated in the spatial domain by an adaptive prefiltering and uniform down sampling process. The resulting side descriptions are conventional square sample grids and can be coded by any of the existing image compression methods. The side decoder and central decoder reconstruct the input image by first decompressing the down-sampled image and then solving a least-squares inverse problem, guided by a 2D piecewise autoregressive model. Compared with the existing image MDC methods in the literatures, the proposed SMMD technique offers the lowest encoder complexity, complete standard compliance, competitive rate-distortion performance, and superior subjective quality.

These contributions are contained in the remaining chapters of this thesis as well as four conference and three journal papers. Our first new adaptive interpolation method was presented in *IEEE ICIP* 2005 [9]. The second method, SAI, was published in *IEEE Transactions on Image Processing* [8]. An earlier exposition of this method was presented in *IEEE ICIP* 2007 [10]. Our third interpolation method, the model-based nonlinear image restoration scheme, was submitted to *IEEE Transactions on Image*

Processing for review [11]. The CADU technique for low-rate image compression was presented in *IEEE DCC* 2008 [12], and a journal paper will appear in *IEEE Transactions on Image Processing* [13]. The SMMD scheme was presented in *IEEE MMSP* 2008 [14].

1.3 Organization

The remaining of this thesis is organized as follows. Chapter 2 reviews existing works on image interpolation and the interpolation based low-rate image compression methods. Our first adaptive non-linear image interpolation method is described in Chapter 3. Chapter 4 presents the new soft-decision adaptive image interpolation method. Our most sophisticated interpolation technique, the model-based nonlinear image restoration scheme, is proposed in Chapter 5. Chapter 6 develops the CADU approach for low bit-rate image compression, and the SMMD scheme is studied in Chapter 7. The thesis closes with conclusions and suggested future works in Chapter 8.

Chapter 2

Review of Existing Works

Interpolation as a topic of mathematics has a very long history. A chronological overview of the developments in interpolation theory since ancient time was presented in [15]. The first application of interpolation in image processing was reported in early 1970s. From then, many image interpolation techniques have been developed. Depending on whether they are adaptive to the image signals, these techniques can be classified in two groups: non-adaptive methods and adaptive methods. The non-adaptive image interpolation methods have the advantages of low complexity and low cost of hardware implementation. Their common drawback is the inability to adapt to varying pixel structures in a scene, due to the use of scene-independent interpolators. As a result, they are all susceptible to defects such as jaggies, blurring, and ringing. The adaptive interpolation methods generally have higher interpolation accuracy or/and better visual quality in the expense of higher computation complexity than the non-adaptive methods. In this chapter, we will review some representative and popular image interpolation algorithms in both groups, as well as some existing interpolation based low-rate image compression methods.

2.1 Non-adaptive Interpolation Methods

The simplest interpolation methods are nearest neighbor interpolation and bilinear interpolation [16]. Nearest neighbor interpolation simply duplicates the nearest pixel for each missing pixel in the high resolution image. Bilinear interpolation is also very simple. It reconstructs a missing pixel as an average of its neighboring low resolution pixels. These two methods are very fast, but their performance leaves much to be desired. Nearest neighbor interpolation produces objectionable checkerboard effect, particularly for large scaling factors; and bilinear interpolation severely blurs edges and textures.

More complicated methods were developed to improve the interpolation accuracy. One popular technique is cubic convolution. It uses a sinc-like kernel composed of piecewise cubic polynomials and significantly improves the interpolation accuracy of the nearest neighbor and bilinear interpolation methods. Cubic convolution technique was first mentioned in the early 1970s and was analyzed in detail by Keys [7] in 1981 for digital image interpolation. The technique was also examined by Park and Schowengerdt in frequency domain [17]. The cubic convolution interpolation is also known as bicubic interpolation when applied to images since it interpolates pixels in two separate directions: horizontal and vertical. Motivated by the statistical nonseparable property of real natural images, nonseparable 2D interpolation filters were designed [18, 19, 20]. In [19], Reichenbach and Geng derived a 2D nonseparable cubic convolution kernel with two parameters and showed that it produced higher interpolation accuracy than separable cubic convolution. Later, Shi and Reichenbach relaxed the constraints in [19] and derived another two nonseparable cubic convolution kernels with three and five parameters respectively, and improved somewhat on the interpolation accuracy [20]. The improvements made by the non-separable 2D interpolation kernels were obtained at the expense of higher complexity.

Splines were also used in image interpolation. The earliest and popular method was developed by Hou and Andrews in 1978 [21]. The method is known as B-spline

interpolation or cubic spline interpolation. Maeland compared the cubic spline interpolation with cubic convolution interpolation, and concluded that cubic spline interpolation had superior performance but higher complexity [22]. Unser *et al.* designed an optimal spline algorithm and claimed that the method could achieve the closest approximation of the original signal in the L_2-norm [23]. The splines were also thoroughly studied as an effective tool for signal and image processing in [24]. To reduce the complexity, Vrcelj and Vaidyanathan replaced the B-Spline filter with a short finite impulse response (FIR) filter and proposed a simplified implementation of the B-splines based image interpolation methods [25].

Besides cubic convolution and cubic splines, many other kernels were proposed for image interpolation. Some of these kernels were described and compared by Lehmann and Spizter in [26]. In particular, they analyzed B-spline interpolation techniques of degree 2, 4, and 5 in [27]. They concluded that high-degree B-splines had higher interpolation accuracy and comparable complexity compared with lower degree B-splines.

2.2 Adaptive Interpolation Methods

With ever increasing computation power in image and video processing, more sophisticated adaptive image interpolation methods were proposed to improve the non-adaptive interpolation methods.

To adapt interpolators to local properties of images, many researchers proposed modifications on conventional cubic convolution interpolation and cubic spline interpolation methods [28, 29, 30, 31]. In [28], Ramponi proposed a warped distance-based adaptive image interpolation method. The main idea of this method is to modify the Euclidean distances to reflect some local property of the image signal. This method can be easily combined with conventional image interpolation methods such as bilinear, bicubic, or cubic spline interpolation. Han and Baek [29] adaptively modified the

parametes of the parametric cubic convolution kernel and reported better results than traditional bicubic method. In [30], Shi and Ward proposed a postprocessing method to improve the visual quality of the interpolated images. The values of pixels near edges were modified to reduce jaggies caused by non-adaptive interpolation methods. Hwang and Lee applied an inverse gradient to the structure of conventional bilinear and bicubic interpolation to sharpen edges[31]. In [32], the authors applied splines as image model to interpolate the high resolution images from nonuniformly sampled images. The interpolation problem was formulated in spline domain and an adaptive smoothness prior was used as regularization term.

As discussed in the previous chapter, edges play important role in human vision system. Non-adaptive interpolation methods tend to blur edges and/or introduce artifacts in edge area due to their isotropic interpolation kernels. In fact, edges have asymmetric spectrum since the frequency is low along edges and high perpendicular to edges. To exploit this property, many researchers advocated the approach of edge-guided interpolation. Jensen and Anastassiou published a scheme that detects edges and fits them with some templates to improve the visual perception of interpolated images [33]. Allebach and Wong detected the edges of the original image first and then used the generated edge map to emphasize the visual integrity of the detected edges [34]. Method in [35] first estimated the local characteristics of the image by performing block classification and then applied different filters to reconstruct the high resolution images. Carrato and Tenze used some predetermined edge patterns to optimize the parameters in the interpolation operator [36]. Malgouyres and Guichard theoretically and experimentally analyzed some edge-guided image enlargement methods in [37]. In [38], an edge-directed interpolation method was proposed with emphasizing on the fidelity and sharpness of edges in the interpolated images. In [39], Muresan proposed a fast edge-directed polynomial interpolation method. Edge pixels were interpolated along the edge direction, and non-edge pixels were interpolated by fusing the multi-directional estimates. Wang and Ward [40] detected step edges or ridges, and then

applied bilinear method with an orientation-adaptive parallelogram to reconstruct the missing high resolution pixels on those edges or ridges.

Instead of explicitly detecting edges prior to interpolation, many edge-guided interpolation methods rely on implicit edge information. Li and Orchard proposed to estimate the covariance of high resolution image from the covariance of the low resolution image, and then interpolate the missing pixels based on the estimated covariance [3]. Since the edge information is built into the algorithm, the method preserves edge structures well. This edge-directed interpolation work was cast by Muresan and Parks into the framework of adaptive optimal recovery [41]. Alternatively, Zhang and Wu proposed to interpolate a missing pixel in multiple directions, and then fuse the directional interpolation results by minimum mean square error (MMSE) estimation [42]. Also, Cha and Kim proposed a postprocessing method to estimate the high resolution image based on a system of nonconvex nonlinear partial differential equations [43]. They reported that clear edges were formed after 2 to 3 iterations. They further extended the method to interpolate color images where the three channels were jointly interpolated [44]. Another edge-guided method was proposed in [45]. In this method, the edge directions were implicitly estimated and were indicated by length-16 weighting vectors, and these weighting vectors were implicitly used to formulate geometric regularity constraint which was imposed on the interpolated image through a Markov random field model.

Wavelets were also used in image interpolation. The interpolation is done by predicting the high-resolution details from the low resolution observations [46, 47, 48, 49, 50]. Carey *et al.* proposed a method that estimated the regularity of edges by measuring the decay of wavelet transform coefficients across scales and preserved the underlying regularity by extrapolating a new subband to be used in image resynthesis [46]. In [47], an MMSE estimator was constructed to synthesize the detailed wavelet coefficients as well as to minimize the mean squared error for high-resolution signal recovery. Based on the behavior of edges across scales in the scale-space domain,

Muresan and Parks estimated the coefficients of the fine scale from a set of known coefficients at the coarser scales [48]. Chang and Cvetković used the wavelet transform to extract information about sharp variations in the low resolution images, and then implicitly applied interpolation that adapts to the image local characteristics [49]. In [50], Temizel and Vlachos exploited wavelet coefficient correlation in a local neighborhood and employed linear least-squares regression to estimate the unknown detail coefficients.

The problem of image interpolation has been also studied in the field of the computer vision [51, 52, 53, 54, 55]. In [51], a set of deformable contours were used to define the boundaries between regions in an image and were evolved by a gradient flow. The goal of the interpolation in this method is to smooth the boundaries while maintain sharp transitions across region boundaries. Freeman *et al.* [52] selected high-resolution patches from training set according to local low-frequency details and adjacent, previously determined high-frequency patches. Similar method was further developed in [53] and [54]. In [53], Baker and Kanada focused on the reconstruction of high-resolution face images from training set. Sun *et al.* [54] first detected the contours of the objects and then reconstructed high resolution image primitives along contours from the training set. In this method, contour smoothness constraints were also enforced by a Markov chain based inference algorithm. In [55], Lin *et al.* classified the image into human perception nonsensitive class and sensitive class according to the characteristics of the human vision system. A trained neural network was used to interpolate the sensitive region along the edge directions.

Other techniques were also developed for image interpolation. In [56], the image was modeled as a Markov random field, and the high resolution image was estimated by maximum a posterior estimation. Iterative methods, such as projection onto convex sets (POCS) schemes [57, 58], were also proposed for image interpolation. Fekri *et al.* applied vector quantization method to the interpolation of text images [59]. Woods *et al.* [60] proposed algorithms for reconstructing high resolution image

from multiple low resolution images. The authors developed two algorithms based on the expectation maximization and maximum a posteriori respectively. In [61], a kernel function was added in the regression to give the nearby samples higher weight than samples farther away when estimating parameters in the regression function. In [62], Kopf *et al.* used bilateral filters to reconstruct a better high resolution image from the available high resolution image and the associated low resolution image.

2.3 Interpolation Based Low-Rate Image Compression Methods

In this section, we will review interpolation based low-rate image compression methods. In these methods, the input image is downsampled before compression, and the decoder applies image interpolation methods to upconvert the LR image to original resolution. Such a scheme first appeared in literature in 1993 [63], and was further studied by some researchers in recent years [64, 65, 66, 67, 68]. In [64] Bruckstein *et al.* explained analytically why it is advantageous to downsample an image prior to JPEG compression and then upsample the JPEG-decoded image. The authors developed a model for expected distortion of discrete cosine transform (DCT) based JPEG codec and gave an expression to determine the rate-distortion optimal downsampling factor. Segall *et al.* extended the interpolation based compression scheme to low-rate video coding [65]. Following up on [64], Tsaig *et al.* proposed an image-dependent algorithm to find optimal filters for decimation and interpolation [66]. Lin and Dong studied the so-called critical bit rate, below which it pays to downsample an image prior to DCT-based JPEG compression [67]. In addition they proposed a downsampling technique that adapts downsampling factor, direction and DCT quantization step size to local image characteristics. Gan *et al.* also proposed undersampled boundary pre- and post-filters to subdue blocking artifacts of DCT-based block codecs at low bit rates [68].

Chapter 3

Method of Texture Orientation Map and Kernel Fisher Discriminant

In this chapter we present our first new adaptive non-linear image interpolation method. In this method, a texture orientation map (TOM) of the LR image is generated by directional Gabor filters to estimate the edge directions. The interpolation direction for each missing HR pixel is determined initially by TOM in a local window, and is then refined by a kernel Fisher discriminant. This allows the interpolator to exploit prior knowledge gained from a training set. After the interpolation direction is determined, the missing HR pixels are estimated by interpolating along that direction.

3.1 Overview

As in the exiting literature, we model a LR image as a down-sampled version of the associated HR image, as illustrated in Fig. 3.1. The task of image interpolation is to estimate the values of those pixels that are missing in the HR image based on the

available neighboring pixels of the LR image. The interpolation can be done fairly easily in smooth regions, which constitute the most part of a natural continuous-tone image for it has an exponentially decay power spectrum. However, the interpolation becomes error prone in regions of edges and textures where the HR image signal may exceed the Nyquist limit of the LR image. Although these errors may be statistical outliers, their adverse effects on the visual quality of the reconstructed HR image can be disproportionally large to their small population. Therefore, the most critical issue in image interpolation is how to handle these worst cases, i.e., reconstructing edges and textures as accurately as possible.

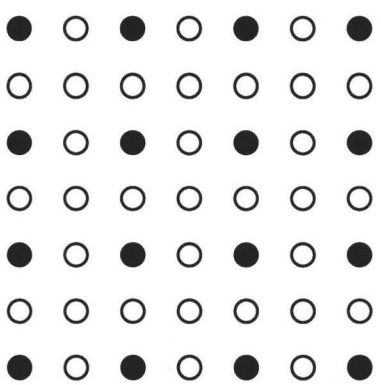

Figure 3.1: Formation of a LR image from a HR image by down-sampling. The black dots are the LR image pixels and the white dots are the missing HR pixels.

To reconstruct a two-dimensional image signal that is insufficiently sampled, we have two venues to explore. Firstly, if the HR signal does not exceed the Nyquist limit of the LR image in all directions, then an interpolation in a low-pass direction can succeed in reconstructing the original. To determine the interpolation direction the key is the estimation of the orientation of edges and textures at the missing pixels. We take a new approach of high order context to solving this estimation problem. An input LR image is first analyzed by a bank of directional Gabor filters, and the filter responses at LR pixels are used to generate a so-called texture orientation map of the LR image. In the context of TOM each missing HR pixel is classified

either as smooth or textural. In smooth regions the interpolation can be done by any existing method. For the textural pixels the interpolation direction is carefully chosen by examining TOM in local windows of different orientations and measuring the directional variations.

Secondly, even if the HR signal is beyond the Nyquist limit in all directions, we can still hope for good estimate of the missing samples by using some suitable prior knowledge. One possibility is to use training data to learn edge/ texture orientation hence the correct interpolation direction in a context of TOM of the LR image. We cast the determination of correct interpolation direction into an optimal classification problem, in which the observable features fed to the classifier are drawn from TOM. The technique of kernel Fisher discriminant (KFD) is used to design the classifier. This classification-driven interpolation technique is able to resolve some of very difficult cases for which the existing methods fail.

This chapter is organized as follows. The texture orientation map is defined in Sec. 3.2, followed by discussions on how to use TOM to estimate interpolation directions in Sec. 3.3. Sec. 3.4 develops the kernel Fisher discriminant technique to refine the interpolation directions using prior knowledge of a training set. Sec. 3.5 reports experimental results. This chapter closes with a summary in Sec. 3.6.

3.2 Texture Orientation Map

Adaptive directional interpolation in reconstructing a HR image needs to be anchored on contextual information from the observed LR image. To this end we build a so-called texture orientation map that presents the texture orientation of each pixel in the LR image. A bank of Gabor filters is applied to detect the presence or lack of an edge at each LR pixel, and determine the direction of the edge, if it exists. We

choose the following bank of Gabor filters:

$$\begin{aligned} g_m(i,j) &= \frac{1}{2\pi\sigma_i\sigma_j} e^{-\frac{1}{2}(\frac{i_m^2}{\sigma_i^2}+\frac{j_m^2}{\sigma_j^2})} cos(2\pi f i_m) \\ i_m &= icos(\theta_m) + jsin(\theta_m); \\ j_m &= -isin(\theta_m) + jcos(\theta_m); \\ \theta_m &= \frac{(m-1)\pi}{8};\ m = 1, 2, \ldots, 8 \end{aligned} \tag{3.1}$$

where σ_i and σ_j are standard deviations of the Gaussian envelope, and f is the frequency of the sinusoid. Although filters of arbitrary orientations are analytically possible, we use only eight uniformly quantized discrete orientations for ease of implementation and because such an angular resolution is sufficient for an expansion factor of two from LR image to HR image (see Fig. 3.1). The scale parameters σ_i and σ_j should be properly chosen to make the detected texture orientation more robust to noises. In fact, this is the main reason for choosing Gabor filters instead of conventional gradient operator. For the application of image interpolation, we are mainly concerned about the direction of high frequency signal, and hence choose $f = \sqrt{2}/4\, cycles/pixel$, which is the highest frequency suggested in [69]. In order to have low redundancy, the filters are normalized to have zero dc response.

Given an LR image I_l, we define its TOM $T(i,j)$ by the magnitudes $g_m(i,j)$ of the responses of Gabor filters $G_m(i,j)$, $1 \leq m \leq 8$, as the follows:

$$T(i,j) = \begin{cases} \phi, \text{ if } \max\limits_m g_m(i,j) - \min\limits_m g_m(i,j) < \epsilon \\ \perp\theta_j,\ j = \max_m^{-1} g_m(i,j) \end{cases} \tag{3.2}$$

where ϵ is a threshold for smoothness, and $\perp\theta$ stands for the angle perpendicular to θ. Namely, for the pixel position (i,j), if the responses of all eight directional filters are close to each other in magnitude, then $T(i,j) = \phi$, indicating that the image waveform is smooth at (i,j); otherwise, the pixel is deemed textural and the texture orientation $T(i,j)$ is set to be perpendicular to the direction in which the Gabor filter has the maximum response.

3.3 TOM-based Decision Discrimination

In adaptive image interpolation the key issue is the choice of interpolation direction. In this section we develop a procedure to determine the interpolation direction in the context of TOM. We treat two different geometric configurations of the LR and HR pixels separately in the following two subsections.

3.3.1 Case of 4-connected LR neighbors

First, let us consider the situations that the HR pixel $x(i,j)$ to be interpolated has two 4-connected neighboring LR pixels, as illustrated in Fig. 3.2. Since the discrete geometries of Fig. 3.2(a) and Fig. 3.2(b) are symmetric to each other, it suffices for us to only examine the horizontal case.

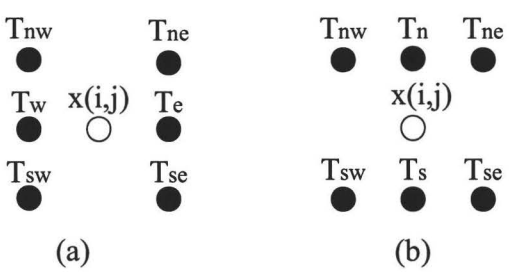

Figure 3.2: A missing pixel with 4-connected LR neighbors: (a) horizontal case; (b) vertical case.

For convenient denotation in further discussions, let the eight different orientations of TOM be signed angles (see Fig. 3.3):

$$T(\cdot,\cdot) \in \{0, \pm\pi/8, \pm\pi/4, \pm 3\pi/8, \pi/2\}. \tag{3.3}$$

Referring to Fig. 3.2(a) for notations, if $T_w = T_e = \phi$, then $x(i,j)$ is classified as smooth, and the cubical interpolation is used to interpolate $x(i,j)$ horizontally. In fact, interpolation direction in a smooth area is not critical. Also, for the sake of unification we can treat $T(\cdot,\cdot) = \phi$ as though $T(\cdot,\cdot) = 0$ since in this case we interpolate

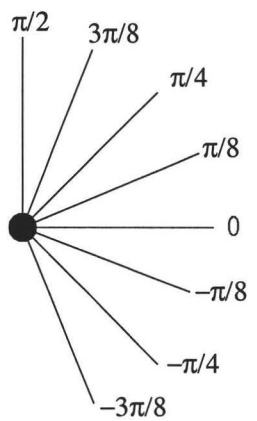

Figure 3.3: Illustration of TOM value as signed angles.

horizontally anyways in smooth areas.

If $|T_w| \leq \pi/8$ and $|T_e| \leq \pi/8$, then $x(i,j)$ is classified as having horizontal orientation, and it will be cubically interpolated in horizontal direction.

For all other possible combinations of T_w and T_e, we first determine if the interpolation direction $\theta(i,j)$ should be positive or negative. To make this decision let us examine the two directional contexts of $x(i,j)$:

$$C_+ = \{T_w, T_e, T_{ne}, T_{sw}\},\ C_- = \{T_w, T_e, T_{nw}, T_{se}\} \tag{3.4}$$

where $T_{ne}, T_{sw}, T_{nw}, T_{se}$ are the TOM values of the LR pixels in the northeast, southwest, northwest, and southeast directions (see Fig. 3.2). If all TOM values in C_+ are non-negative, or if all TOM values in C_- are non-positive, written as $C_+ \geq 0$ and $C_- \leq 0$, then we set $\theta(i,j) > 0$ or $\theta(i,j) < 0$ respectively.

If none of the above tests passes, then we compute the variances of the two sets C_+ and C_-, denoted by σ_+ and σ_-, and set $\theta(i,j) > 0$ if $\sigma_+ < \sigma_-$, or $\theta(i,j) < 0$ if $\sigma_+ > \sigma_-$.

The above procedure, whose flowchart is given in Fig. 3.4, decides whether $\theta(i,j) = 0$, $\theta(i,j) > 0$, or $\theta(i,j) < 0$ in interpolating $x(i,j)$. For the latter two cases, a more elaborated classification process is needed, which will be the subject of Sec. 3.4.

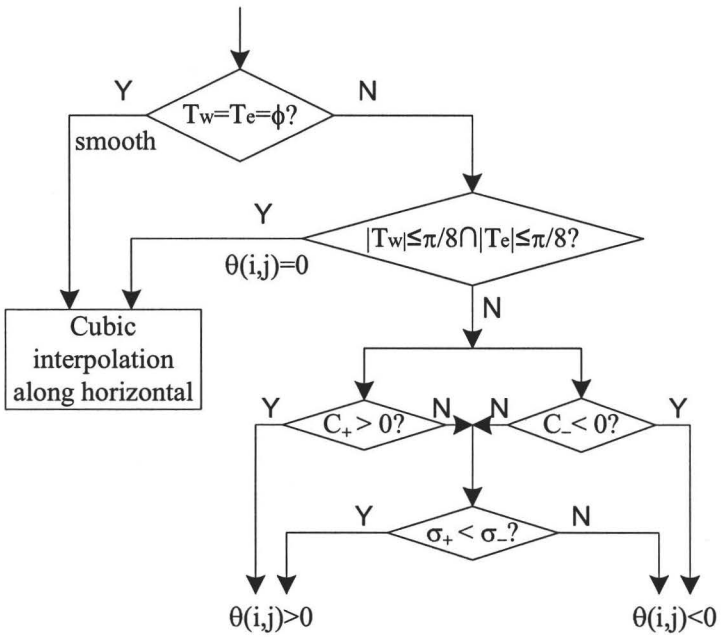

Figure 3.4: Decision of interpolation direction.

3.3.2 Case of 8-connected LR neighbors

Next we proceed to the case where the HR pixel $x(i,j)$ has four 8-connected neighboring LR pixels as depicted by Fig. 3.5. Similarly to the 4-connected case, a stepwise decision process is carried out to determine if $\theta(i,j) = \pm\pi/4$, $\theta(i,j) > 0$, or $\theta(i,j) < 0$, which is depicted by the flow chart in Fig. 3.6. In the flow chart,

the two directional contexts of $x(i,j)$ are defined as:

$$C_+ = \{T_{nw}, T_{ne}, T_{sw}, T_{se}, T_{nne}, T_{nee}, T_{ssw}, T_{sww}\} \tag{3.5}$$
$$C_- = \{T_{nw}, T_{ne}, T_{sw}, T_{se}, T_{nww}, T_{nnw}, T_{see}, T_{sse}\}.$$

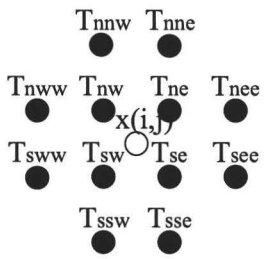

Figure 3.5: A missing pixel with 8-connected LR neighbors.

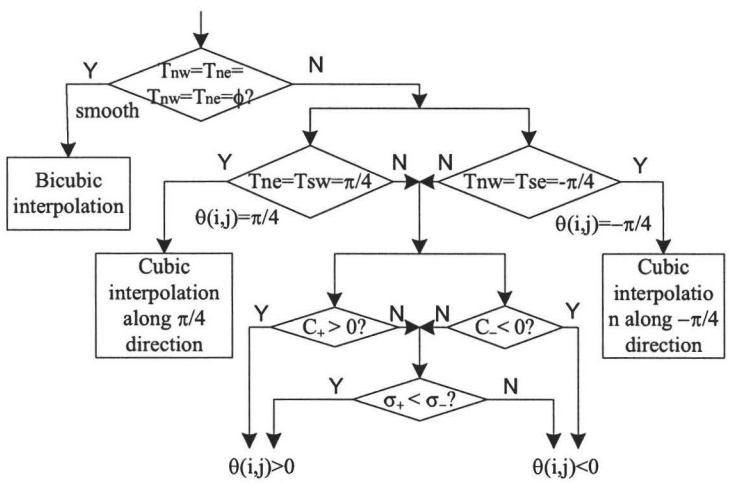

Figure 3.6: Decision of interpolation direction for a missing pixel with 8-connected LR neighbors.

3.4 Direction Refinement via Kernel Fisher Discriminant

In the previous section we see how the interpolation direction can be chosen by the technique of variation analysis of TOM. However, the discrimination power of TOM is theoretically restricted by the Nyquist limit of the LR image. For any hope of exceeding this limit, one has to bring in additional information. In this section we propose an approach of using prior knowledge learnt from a training set to refine interpolation direction. Specifically, we cast the problem into one of optimal classifier

design and solve it using KFD.

Different geometric configurations of LR and HR pixels need to be treated separately. Without loss of generality, we sketch our main idea for a concrete configuration as illustrated in Fig. 3.7. Other configurations can follow easily via symmetry. Referring to Fig. 3.7 for the geometry and notations, if a TOM-based analysis yields $\theta(i,j) > 0$, we come to assess two estimates of $x(i,j)$:

$$\begin{aligned} I_1 &= \sum_{i=1,2,3,4} a_i L_i, \\ I_2 &= \sum_{i=1,2,5,6} b_i L_i \end{aligned} \tag{3.6}$$

where a_i and b_i are interpolation coefficients that can be obtained by the least-square method from a training set. In pursue of a better angular resolution we now face a decision problem of choosing between I_1 and I_2. Let the decision whether I_1 or I_2 is a better estimate of $x(i,j)$ be a binary random variable Y. Consider $\mathbf{f} = (L_1, L_2, \cdots, L_6)$ as a vector of features that Y exhibits. If $P(Y|\mathbf{f})$ is known, then the optimal decision corresponds to the value of Y that maximizes the posterior probability $P(Y|\mathbf{f})$. But $P(Y|\mathbf{f})$ is generally unknown, we alternatively convert the decision problem to one of binary classification in the feature space of $\mathbf{f}$. Given a suitable training set Z, the value of Y partitions the set Z into two subsets Z_0 and Z_1. Set Z_i consists of all the training feature vectors associated with $Y = i$, $i = 0, 1$. Our task is to design a classifier to separate Z_0 from Z_1 with the minimum number of misclassifications. We applied both linear Fisher discriminant and KFD [70][71] to this classification problem, and found that the former is ineffective but the latter is.

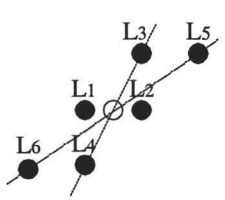

Figure 3.7: Two competing interpolation directions when $\theta(i,j) > 0$.

KFD first maps the feature vectors into some new feature space F in which different classes are better separable. A linear discriminant is computed to separate input classes in F. Implicitly, this process constructs a non-linear classifier of high discriminating power in the original feature space. Let $\Phi(\mathbf{f})$ be the nonlinear mapping from original feature space to some high-dimensional Hilbert space F. The goal is to find the projection line $\mathbf{p}$ in F such that the F-ratio validity index $J(\mathbf{p})$

$$J(\mathbf{p}) = \frac{\mathbf{p}^T S_B^\Phi \mathbf{p}}{\mathbf{p}^T S_W^\Phi \mathbf{p}} \tag{3.7}$$

is maximized, where S_B^Φ and S_W^Φ are the between-class and within-class covariance matrices. Since the space F is of very high dimensions, the function $\Phi(\mathbf{f})$ is infeasible. A technique to overcome this difficulty is the Mercer kernel function $k(i,j) = \Phi(i) \cdot \Phi(j)$, the dot product in Hilbert feature space F. A popular choice for the kernel function k that has been proved useful(e.g. in support vector machines) is the Gaussian RBF(radio base function), $k(i,j) = exp(-\|i-j\|^2/2\sigma^2)$. Under some mild assumptions on S_B^Φ and S_W^Φ, any solution $\mathbf{p} \in F$ maximizing (3.7) can be written as the linear span of all N mapped samples

$$\mathbf{p} = \sum_{j=1}^{N} \beta_j \Phi(\mathbf{f}_j) \tag{3.8}$$

As a result, the F-ratio $J(\mathbf{p})$ can be reformulated as:

$$J(\mathbf{p}) = \frac{\mathbf{p}^T S_B^\Phi \mathbf{p}}{\mathbf{p}^T S_W^\Phi \mathbf{p}} = \frac{\beta^T \mathbf{A} \beta}{\beta^T \mathbf{B} \beta} \tag{3.9}$$

where $\mathbf{A}$ and $\mathbf{B}$ are $N \times N$ matrices:

$$\begin{aligned} \mathbf{A} &= \sum_{j=1}^{M} n_j (\bar{\mu} - \mu_j)(\bar{\mu} - \mu_j)^T, \\ \mathbf{B} &= \mathbf{K}\mathbf{K}^T - \sum_{j=1}^{M} n_j \mu_j \mu_j^T \end{aligned} \tag{3.10}$$

where $\mathbf{K}$ is the kernel matrix, $\mathbf{K}_{ij} = \Phi(\mathbf{f}_i) \cdot \Phi(\mathbf{f}_j)$, $\mu_j = \mathbf{K} \cdot \mathbf{1}_j / n_j$, $\bar{\mu} = \mathbf{K} \cdot \mathbf{1}/N, \mathbf{1}_j \in (0,1)^N$ are membership vectors corresponding to class labels, and $\mathbf{1}$ is the vector of

all ones. The projection of a test image feature sample $\mathbf{f}$ onto the discriminant is given by the inner product

$$(\mathbf{p}, \Phi(\mathbf{f})) = \sum_{j=1}^{N} \beta_j k(\mathbf{f}, \mathbf{f}_j) \tag{3.11}$$

In practise, maximizing (3.9) requires to solve the $N \times N$ matrix eigenvalue problem, which is intractable for large N. As in [70], instead of using (3.8), we express $\mathbf{p}$ in the subspace:

$$\mathbf{p} = \sum_{j=1}^{l} \beta_j \Phi(\mathbf{f}_j) \tag{3.12}$$

where $l \ll N$, and samples $\mathbf{f}_j$ are selected from all raw training vectors.

Given the dimension l of the subspace of F, the partial expansion (3.12) presents an approximation of the optimal KFD solution. This approximation can be incrementally improved by adding a new sample vector one at a time to the existing expansion. The projection value of a vector $\mathbf{f}$ is given by the inner product

$$(\mathbf{p}, \Phi(\mathbf{f})) = \sum_{j=1}^{l} \beta_j k(\mathbf{f}, \mathbf{f}_j) \tag{3.13}$$

We build the KFD classifier in two steps: First, given a training set of feature vectors, we find the projection direction $\mathbf{p}$ as above. Second, we compute the projection values of all training feature vectors and find the threshold ξ between the two classes to minimize the classification error. Although the KFD design process is computationally expensive, it is done off line once for all, given a training set. Applying KFD to interpolation is simple: the feature vector $\mathbf{f}$ of the pixel in question is projected by (3.11). Then the projected value is threshold by ξ to decide the optimal interpolation direction (i.e., $Y = 1$ or $Y = 0$).

3.5 Experimental Results and Remarks

The proposed image interpolation method based on TOM and KFD is implemented and compared with three other methods: bilinear interpolation, bicubic interpolation

[7] and subpixel edge localization [33]. The first two methods are representatives of linear interpolation methods. The last one is relevant to this work in that the subpixel edge localization technique also guides interpolation along estimated edge direction.

Fig. 3.8 shows a part of the original Baboon image and the reconstructed that part by the above mentioned interpolation methods. The Baboon image presents a challenge to interpolation algorithms due to its fine edge/texture details. Our informal human subject study seemed to indicate that the viewers prefer the proposed method by a significant margin. The edges reconstructed by the new method are sharper and have less ringing effect. The comparison of the PSNR results for other well-known test images between these methods is presented in Table 3.1, which shows that our method also obtains the highest PSNR.

Table 3.1: The PSNR(dB) results

Image	**Lena**	**Airplane**	**Baboon**
Bilinear Interpolation	33.37	28.95	22.52
Bicubic Interpolation	33.92	29.67	22.58
Method in [33]	33.09	28.39	22.48
Proposed Method	34.28	29.95	23.41

The performance of KFD-based image interpolation naturally depends on the match of statistics of the input image and the training set. The reported experimental results were obtained using a general training set that consists of ten natural images. All images used to generate the reported experimental results are outside of the training set.

3.6 Summary

A new adaptive nonlinear image interpolation method was proposed in this chapter. The interpolation direction of missing HR pixels was estimated with the guidance of a

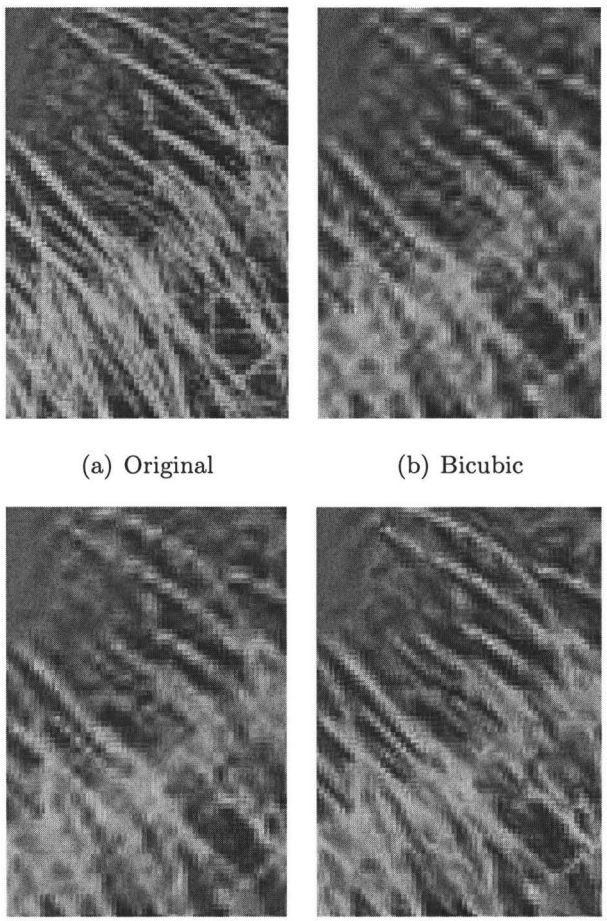

(a) Original (b) Bicubic

(c) Method in [33] (d) Proposed

Figure 3.8: Reconstructed Baboon images by different methods.

TOM generated from known LR image. The refinement of the estimated direction was converted to a classification problem. The classifier was designed using kernel Fisher discriminant technique with a training set of HR images. This new classification-based method achieves higher PSNR and better visual quality than previous methods. It can correctly solve some of very difficult cases for which the traditional methods fail.

Chapter 4

Soft-decision Adaptive Interpolation

In previous chapter, we described an adaptive nonlinear interpolation method that assumes and uses some prior knowledge learnt from a training set of HR images. But the performance of the learning approach degrades if there is a statistical mismatch between the input image and the training set. Unless the input images are confined to a narrow known class (e.g., faces), it is prudent to estimate the HR image using primarily the statistics available in the input LR image. In this and subsequent chapters we develop adaptive image interpolation methods without the use of training HR images. Instead we boost the performance of these methods by introducing a class of versatile parametric image models: 2D piecewise autoregressive process. The model parameters are estimated in a moving window in the input LR image. The pixel structure dictated by the learnt model is enforced by a soft-decision estimation process onto a block of pixels, including both observed and estimated.

4.1 Overview

The reproduction quality of any image interpolation algorithm primarily depends on its adaptability to varying pixel structures across an image. In fact, modeling of non-stationarity of image signals is a common challenge facing many image processing tasks, such as compression, restoration, denoising, and enhancement. Wu *et al.* [72] had a measured success in this regard in a research on predictive lossless image compression. In that work a natural image is modeled as a piecewise 2D autoregressive process. The model parameters are estimated on the fly for each pixel using sample statistics of a local window, assuming that the image is piecewise stationary. In this work we extend this approach to image interpolation. An obvious difference is in that the sample set for parameter estimation has to be causal to the current pixel for predictive coding, but does not need to be so for interpolation, which is to the advantage of the latter task. On the other hand, for image interpolation the fit of the model to the true high-resolution image signal is made more difficult by the fact that only a low-resolution version of the original can be observed.

All image interpolation methods involve fitting missing pixels to some sample structure learnt from the low resolution image. This is best accomplished by estimating a block of missing pixels in relation to the nearby known pixels rather than estimating the individual missing pixels in isolation as done in the literature up to now. The main result of this chapter is a new image interpolation technique, called soft-decision adaptive interpolation (SAI). The SAI technique, via a natural integration of piecewise two-dimensional autoregressive modeling and block estimation, achieves superior image interpolation results to those reported in the literature. It is shown that the new SAI technique is equivalent to interpolation using an adaptive non-separable 2D filter of high order.

The rest of the chapter is structured as follows. Section 4.2 defines a two-dimensional piecewise autoregressive (PAR) image model to facilitate the subsequent development. Section 4.3 presents the most important result of this work: a soft-

decision estimation technique for adaptive image interpolation. Section 4.4 discusses how to estimate the PAR model parameters in the low-resolution image. Implementation details of the SAI algorithm are presented in Section 4.5, where the reader can also gain an insight into the inner work of the SAI technique. Experimental results and a comparison study with some existing popular image interpolation techniques are presented in Section 4.6. Section 4.7 concludes.

4.2 Piecewise Stationary Autoregressive Model

For the purpose of adaptive image interpolation, we model the image as a piecewise autoregressive process:

$$X(i,j) = \sum_{(u,v)\in T} a_{u,v} X(i-u, j-v) + \upsilon_{i,j} \tag{4.1}$$

where T is a spatial template for the regression operation. The term $\upsilon_{i,j}$ is a random perturbation independent of spatial location (i,j) and the image signal, and it accounts for both fractal-like fine details of image signal and measurement noise. The validity of the PAR model hinges on a mechanism that adjusts the model parameters $a_{u,v}$ to local pixel structures. The fact that semantically meaningful image constructs, such as edges and surface textures, are formed by spatially coherent contiguous pixels, suggests piecewise statistical stationarity of the image signal. In other words, in the setting of the PAR model, the parameters $a_{u,v}$ remain constant or near constant in a small locality, although they may and often do vary significantly in different segments of a scene. The piecewise stationarity makes it possible to learn pixel structures such as edges and textures by fitting samples of a local window to the PAR model.

The validity of the PAR model with locally adaptive parameters is corroborated by the success of this modeling technique in lossless image compression. Among all known lossless image coding methods, including CALIC (context-based adaptive lossless codec) [1], TMW [4], and invertible integer wavelets [73], those that employ

the PAR model with adjusted parameters on a pixel-by-pixel basis have delivered the lowest lossless bit rates [72, 74]. In the principle of Kolmogorov complexity, the true model of a stochastic process is the one that yields the minimum description length. Thus we have strong empirical evidence to support the appropriateness and usefulness of the PAR model for natural images.

In the next section, we will integrate the PAR model into a soft-decision estimation framework for the purpose of image interpolation, and develop the SAI algorithm.

4.3 Adaptive Interpolation with Soft Decision

First we introduce some notations that are necessary for the description of the SAI algorithm. Let I_h be the HR image to be estimated by interpolating the observed LR image I_l. Same as in the previous chapter, the LR image I_l is a down sampled version of the HR image I_h by a factor of two. Let $y_i \in I_l$ and $x_i \in I_h$ be the pixels of images I_l and I_h respectively. We write the neighbors of pixel location i in the HR image as $x_{i\diamond t}$, $t = 1, 2, \cdots$. Since $y_i \in I_l$ implies $y_i \in I_h$, we also write an HR pixel $x_i \in I_h$ as y_i (likewise, $x_{i\diamond t}$ as $y_{i\diamond t}$) when it is in the LR image, $x_i \in I_l$, as well.

The SAI algorithm interpolates the missing pixels in I_h in two passes in a coarse to fine progression. The work of the two passes is shown by Fig. 4.1, in which the solid dots are known LR pixels, the shaded dots are those missing pixels to be interpolated in the first pass, and the empty dots are the remaining missing pixels to be interpolated in the second pass. The pixels generated by the first pass and the known LR pixels form a quincunx sublattice of the HR image (the union of solid and shaded dots). The second pass completes the reconstruction of the HR image by interpolating the other quincunx sublattice of empty dots.

Fig. 4.2(a) illustrates the spatial configuration of known and missing pixels involved in the first pass. To avoid intricate notations, from now on we use a single position index to denote a pixel location instead of two dimensional coordinates. For

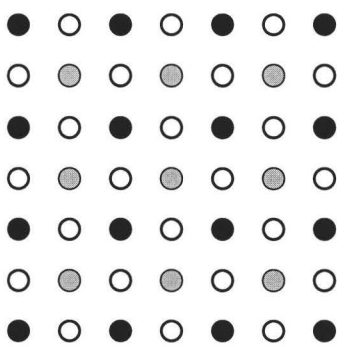

Figure 4.1: Formation of a low resolution image from a high resolution image by down-sampling. The solid black dots are the LR image pixels and the circles are the missing HR pixels. Interpolation is done in two passes: The first pass interpolates the missing pixels marked by shaded circles, and the second pass interpolates the remaining missing pixels marked by empty circles.

a missing pixel $x_i \in I_h$, its four 8-connected neighbors are available LR pixels, denoted by $y_{i\diamond t}^{(8)} \in I_l$, and its four 4-connected neighbors are missing HR pixels, denoted by $x_{i\diamond t}^{(4)} \in I_h$, $t = 1, 2, 3, 4$. Here the relative subscript t is a generic notation to index a two-dimensional neighbor with respect to position i. Similarly, for a pixel $y_i \in I_l$, its four 8-connected neighbors are missing HR pixels, written as $x_{i\diamond t}^{(8)} \in I_h$, and its four 4-connected neighbors are available LR pixels written as $y_{i\diamond t}^{(4)} \in I_l$, $t = 1, 2, 3, 4$.

To interpolate a missing pixel $x_i \in I_h$ in the first pass, we use a PAR model of parameters $\boldsymbol{\chi} = (\chi_1, \chi_2, \chi_3, \chi_4)$ to characterize the diagonal correlations of the image signal in a local window W (see Fig. 4.2(b)). Using the simplified notations to replace $a_{\cdot,\cdot}$, we rewrite (4.1) as

$$x_i = \sum_{1 \le t \le 4} \chi_t y_{i\diamond t}^{(8)} + \upsilon_i. \tag{4.2}$$

With the PAR model we interpolate n missing pixels $\boldsymbol{x} = (x_1, x_2, \cdots, x_n)$ in window W by a least-squares block estimation:

$$\hat{\boldsymbol{x}} = \arg\min_{\boldsymbol{x}} \Big\{ \sum_{i \in W} \Big\| x_i - \sum_{1 \le t \le 4} \chi_t y_{i\diamond t}^{(8)} \Big\| + \sum_{i \in W} \Big\| y_i - \sum_{1 \le t \le 4} \chi_t x_{i\diamond t}^{(8)} \Big\| \Big\} \tag{4.3}$$

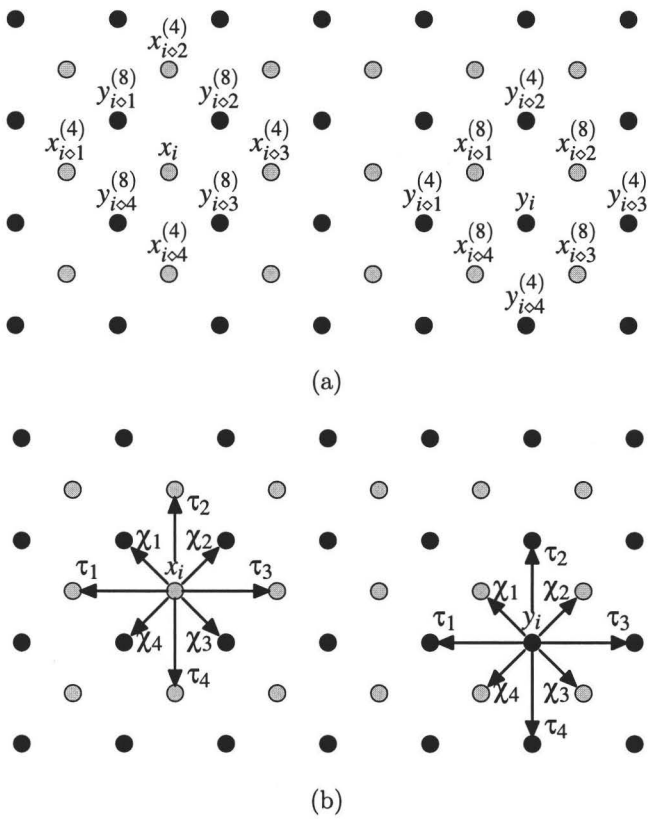

Figure 4.2: (a) Spatial configuration in the first pass. (b) The PAR model parameters $\boldsymbol{\chi} = (\chi_1, \chi_2, \chi_3, \chi_4)$ and $\boldsymbol{\tau} = (\tau_1, \tau_2, \tau_3, \tau_4)$ in relationship to spatial correlations of pixels.

The above image interpolation approach has an important distinction from its predecessors (e.g., [21, 3]). Existing image interpolation methods estimate each missing pixel independently from others, which we characterize as hard-decision estimation. In contrast, we adopt a strategy of soft-decision estimation in resemblance to block decoding of error correction codes. Rather than estimating one sample at a time in isolation, the objective function of (4.3) requires all missing pixels in a local window W to be estimated jointly. Moreover, the soft-decision estimation approach brings in a new feedback mechanism that is the second term in (4.3). This additional term requires the estimates of the missing HR pixels $\boldsymbol{x} \in I_h$ to fit the known LR pixels

$\boldsymbol{y} \in I_l$ with the very same PAR model that fits $\boldsymbol{y} \in I_l$ to $\boldsymbol{x} \in I_h$. Aided by the feedback mechanism that accounts for mutual influences between the estimates of the missing pixels in a local window W, the SAI algorithm can mitigate errors of hard-decision estimation by preventing the PAR model, when applied to estimated HR pixels $x \in I_h$, from being violated on neighboring known LR pixels $y \in I_l$.

To include horizontal and vertical correlations into the SAI algorithm, we introduce four more parameters $\boldsymbol{\tau} = (\tau_1, \tau_2, \tau_3, \tau_4)$ whose geometric meanings are shown in Fig. 4.2(b). These parameters $\boldsymbol{\tau}$ are used to impose the same directional correlation between LR pixels y_i and $y_{i\diamond t}^{(4)}$ on between HR pixels x_i and $x_{i\diamond t}^{(4)}$, namely

$$x_i = \sum_{1 \le t \le 4} \left\| \tau_t x_{i\diamond t}^{(4)} \right\| + \upsilon_i. \tag{4.4}$$

The soft-decision estimation technique can incorporate (4.4) into (4.3). But one should practise caution since the pixels x_i and $x_{i\diamond t}^{(4)}$ in (4.4) are all unknown. By using a Lagrangian multiplier λ to regulate the contribution of (4.4), we extend (4.3) to the following constrained optimal block estimation problem:

$$\begin{aligned} J(\lambda) = \min_{\boldsymbol{x}} \Big\{ & \sum_{i \in W} \Big\| x_i - \sum_{1 \le t \le 4} \chi_t y_{i\diamond t}^{(8)} \Big\| \\ & + \sum_{i \in W} \Big\| y_i - \sum_{1 \le t \le 4} \chi_t x_{i\diamond t}^{(8)} \Big\| + \lambda \sum_{i \in W} \Big\| x_i - \sum_{1 \le t \le 4} \tau_t x_{i\diamond t}^{(4)} \Big\| \Big\} \end{aligned} \tag{4.5}$$

subject to

$$\sum_{i \in W} \Big\| x_i - \sum_{1 \le t \le 4} \tau_t x_{i\diamond t}^{(4)} \Big\| \approx \sum_{i \in W} \Big\| y_i - \sum_{1 \le t \le 4} \tau_t y_{i\diamond t}^{(4)} \Big\|$$

In minimizing $J(\lambda)$ the value of λ is chosen such that $\sum_W \| x_i - \sum_{1 \le t \le 4} \tau_t x_{i\diamond t}^{(4)} \| \approx \sum_W \| y_i - \sum_{1 \le t \le 4} \tau_t y_{i\diamond t}^{(4)} \|$. The SAI algorithm iterates on λ until the constraint is satisfactorily met, by decreasing λ if the left side of the constraint is less than the right side and vise versa. This constraint holds if the sample statistics is shift invariant in the window W. We observe that the value of λ is in the range of $0.2 \sim 0.7$ when meeting the constraint. For most natural images, one can simply choose $\lambda = 0.5$ with no material loss of performance compared with the iteratively computed λ.

Compared to existing autoregressive methods that use parameters χ only [3, 42], the SAI algorithm expands the model parameter space by using two sets of parameters τ and χ. The expanded PAR model has the potential of representing the high-resolution image more accurately than in [3, 42]. However, to circumvent the risk of data overfitting, we do not directly use an autoregressive model of order 8, but rather split model parameters χ and τ in two separate terms of the objective function (4.5). In fact, in separation from χ, the parameters τ can be better estimated than parameters χ using samples in the LR image, as we will see in the next section.

With the block-based soft-decision estimation and the increased order in piecewise autoregressive modeling, the new SAI algorithm achieves unprecedented interpolation accuracy. More importantly it performs consistently well over a wide range of images, and the performance is far less sensitive to feature scales than existing techniques. We will return to these points in Section 4.6 when the experimental results are presented and discussed.

Up to now we have only described the interpolation process of the first pass. Once the missing HR pixels in the first pass are interpolated as described above, half of the HR pixels are obtained. The remaining half of the missing HR pixels are to be interpolated in the second pass. The interpolation problem in the second pass is essentially the same as in the first pass. The only difference is that the SAI algorithm now interpolates the missing HR pixels $x_i \in I_h$ using their four 4-connected neighbors, which are either known in I_l or estimated in the first pass. The problem has the same formulation as in (4.5), if we simply rotate the spatial configuration of Fig. 4.2(a) by 45 degrees (see Fig. 4.3).

4.4 Model Parameter Estimation

A key to the success of the SAI algorithm is how well the model parameters χ and τ in (4.5) can be estimated using LR image samples. Referring to the spatial relation

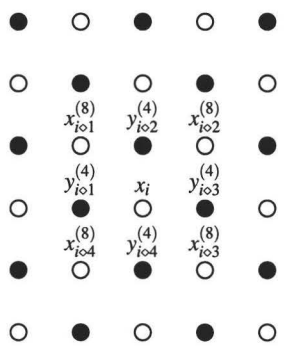

Figure 4.3: Spatial configuration in the second pass of interpolation.

between the samples in Fig. 4.4(b), one gets a linear least-square estimator of the model parameter vector $\boldsymbol{\tau}$:

$$\hat{\boldsymbol{\tau}} = \arg\min_{\boldsymbol{\tau}} \sum_{i \in W} \Big(y_i - \sum_{1 \le t \le 4} \tau_t y_{i\diamond t}^{(4)} \Big)^2 \tag{4.6}$$

where $y_{i\diamond t}^{(4)}$ are the four 4-connected neighbors of the location i in I_l as labeled in Fig. 4.4(b). Note that the estimates of $\boldsymbol{\tau}$ in (4.6) are made using the LR pixels $y_i \in I_l$ that have the same spatial orientation and the same scale as the way the HR pixels $x_i \in I_h$ are related by $\boldsymbol{\tau}$ in (4.5) (this is also clear in Fig. 4.2(b)). Hence the resulting estimates $\hat{\boldsymbol{\tau}}$ are optimal in the least-square sense under the assumption that the sample covariances do not change in the local window W, which is generally true for natural images.

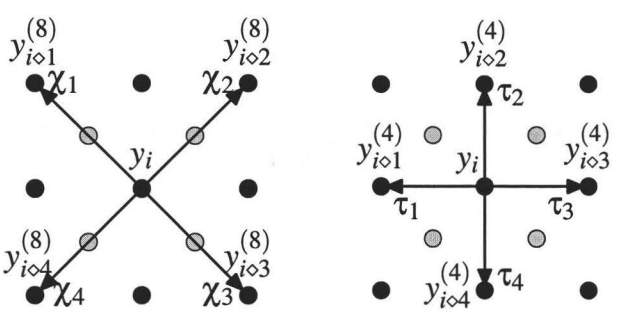

(a) Parameter $\boldsymbol{\chi}$ (b) Parameter $\boldsymbol{\tau}$

Figure 4.4: Sample relations in estimating model parameters.

However, the estimation of the model parameters $\boldsymbol{\chi}$ is more problematic. One can simply, as proposed by Li and Orchard [3], compute $\boldsymbol{\chi}$ via the following linear least-square estimation

$$\hat{\boldsymbol{\chi}} = \arg\min_{\boldsymbol{\chi}} \sum_{i \in W} \Big(y_i - \sum_{1 \le t \le 4} \chi_t y_{i \diamond t}^{(8)} \Big)^2 \tag{4.7}$$

where $y_{i \diamond t}^{(8)}$ are the four 8-connected neighbors of the location i in I_l as labeled in Fig. 4.4(a). The accuracy of (4.7) relies on a stronger assumption that the correlation between pixels is unchanged in different scales. This is because the distance between y_i and $y_{i \diamond t}^{(8)}$ in (4.7) is twice the distance between x_i and $y_{i \diamond t}^{(8)}$ in (4.5).

As argued in [3], the above assumption holds if the window in question has edge(s) of a fixed orientation and of sufficiently large scale. But experiments show (see results in Section 4.6) that previous edge-based interpolation methods are prone to artifacts on small-scale spatial features of high curvature, for which the second order statistics may differ from LR to HR images. In such cases the soft-decision estimation strategy of (4.5) can moderate the effects of estimation errors of (4.7), making the proposed SAI approach considerably more robust.

4.5 Algorithm Details

To perform soft-decision estimation the SAI algorithm needs to operate on blocks of pixels. The neighboring blocks should have some overlaps to prevent possible block visual artifacts. Many spatial configurations of the overlapped blocks can be used. To be concrete let us consider a particular configuration as illustrated in Fig. 4.5. As shown in the figure, a block of 12 unknown pixels $x_1, x_2, \cdots, x_{12}$, arranged in an octagonal window (bounded by the solid line in Fig. 4.5), are jointly estimated, constrained by the 21 available LR pixels $y_1, y_2, \cdots, y_{21}$. Solving the least-squares problem of (4.5) in the octagonal window will yield a group of 12 estimated missing pixels. However, the SAI algorithm will only output the interpolated values of the 4

innermost unknown pixels x_1, x_2, x_3, x_4. In other words, the estimation is done in a moving octagonal window with one layer of perimeter pixels being overlapped with neighboring windows.

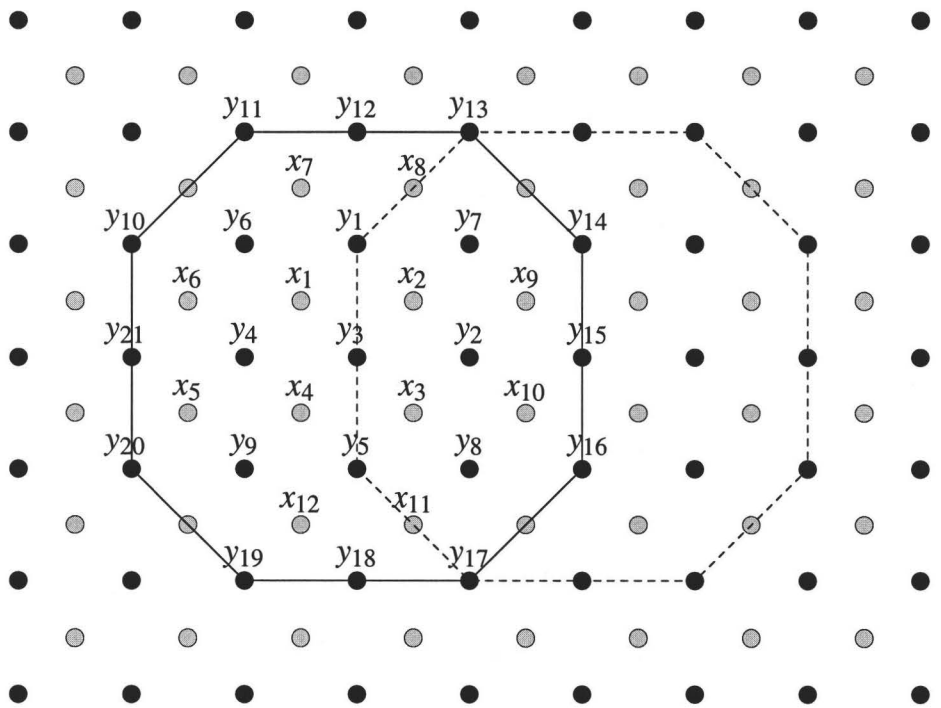

Figure 4.5: A possible configuration used in the soft-decision interpolation algorithm

The choice of window size and the degree of spatial overlap are design details related to implementation complexity and viewer preference on image appearance. Since the algorithm interpolates one block of missing pixels at a time by solving (4.5), the larger the block and the smaller the overlap, the faster the algorithm runs. But the large block size may reduce the adaptability of the PAR model if there are varying features of small scale in a locality. Although higher degree of spatial overlap of neighboring windows means less likelihood of block artifacts, particularly near the boundaries of different features, it may cause some blurring of sharp edges.

If L_2 norm is used, the SAI algorithm involves solving three least-squares problems, namely the determination of model parameters $\boldsymbol{\tau}$, the determination of model

parameters χ, and the minimization problem of (4.5). For each block we can compute τ and χ in the closed form solutions of (4.6) and (4.7). Namely,

$$\hat{\tau} = (\mathbf{B}^T\mathbf{B})^{-1}\mathbf{B}^T\mathbf{b} \tag{4.8}$$

where the column vector $\mathbf{b}$ is composed of all LR pixels y_i inside the block. The i^{th} row of matrix $\mathbf{B}$ consists of the four 4-connected neighbors $y_{i\diamond t}^{(4)}$ of y_i, $t = 1, 2, 3, 4$. And,

$$\hat{\chi} = (\mathbf{A}^T\mathbf{A})^{-1}\mathbf{A}^T\mathbf{b} \tag{4.9}$$

where the i^{th} row of matrix $\mathbf{A}$ consists of the four 8-connected neighbors $y_{i\diamond t}^{(8)}$ of y_i, $t = 1, 2, 3, 4$.

We rewrite (4.5) in matrix form:

$$\min_{\boldsymbol{x}} \Big\{ \|\boldsymbol{C}\boldsymbol{x} - \boldsymbol{D}\boldsymbol{y}\| \Big\} \tag{4.10}$$

where $\boldsymbol{x} = (x_1, x_2, \cdots, x_{12})$ is the vector of the 12 unknown pixels in the current octagon window as labeled in Fig. 4.5, $\boldsymbol{y} = (y_1, y_2, \cdots, y_{21})$ is the vector of the 21 available LR pixels inside and on the boundary of the octagon window in Fig. 4.5, and

$$\boldsymbol{C} = \begin{bmatrix} \mathbf{I}_{12} \\ \mathbf{C}_1 \\ \lambda\mathbf{C}_2 \end{bmatrix} \qquad \boldsymbol{D} = \begin{bmatrix} \mathbf{D}_1 \\ \mathbf{D}_2 \\ \mathbf{0}_{4\times 21} \end{bmatrix} \tag{4.11}$$

where $\mathbf{I}$ is the identity matrix with the subscript being its dimension, $\mathbf{0}$ is the zero matrix whose dimension is indicated by the subscript, λ is the Lagrangian factor in (4.5), and

$$C_1^T = \begin{bmatrix} \hat{\chi}_4 & 0 & \hat{\chi}_1 & \hat{\chi}_2 & 0 \\ \hat{\chi}_3 & \hat{\chi}_1 & \hat{\chi}_2 & 0 & 0 \\ 0 & \hat{\chi}_4 & \hat{\chi}_3 & 0 & \hat{\chi}_2 \\ 0 & 0 & \hat{\chi}_4 & \hat{\chi}_3 & \hat{\chi}_1 \\ 0 & 0 & 0 & \hat{\chi}_4 & 0 \\ 0 & 0 & 0 & \hat{\chi}_1 & 0 \\ \hat{\chi}_1 & 0 & 0 & 0 & 0 \\ \hat{\chi}_2 & 0 & 0 & 0 & 0 \\ 0 & \hat{\chi}_2 & 0 & 0 & 0 \\ 0 & \hat{\chi}_3 & 0 & 0 & 0 \\ 0 & 0 & 0 & 0 & \hat{\chi}_3 \\ 0 & 0 & 0 & 0 & \hat{\chi}_4 \end{bmatrix} \quad C_2^T = \begin{bmatrix} 1 & -\hat{\tau}_4 & 0 & -\hat{\tau}_1 \\ -\hat{\tau}_2 & 1 & -\hat{\tau}_1 & 0 \\ 0 & -\hat{\tau}_3 & 1 & -\hat{\tau}_2 \\ -\hat{\tau}_3 & 0 & -\hat{\tau}_4 & 1 \\ 0 & 0 & 0 & -\hat{\tau}_4 \\ -\hat{\tau}_4 & 0 & 0 & 0 \\ -\hat{\tau}_1 & 0 & 0 & 0 \\ 0 & -\hat{\tau}_1 & 0 & 0 \\ 0 & -\hat{\tau}_2 & 0 & 0 \\ 0 & 0 & -\hat{\tau}_2 & 0 \\ 0 & 0 & -\hat{\tau}_3 & 0 \\ 0 & 0 & 0 & -\hat{\tau}_3 \end{bmatrix} \tag{4.12}$$

$$D_2 = \begin{bmatrix} \mathbf{I}_5 & \mathbf{0}_{5\times 16} \end{bmatrix}$$

$D_1 = \{d_1(i,j)\}$, $i = 1, 2, ..., 12$, $j = 1, 2, ..., 21$;

where

$$d_1(i,j) = \begin{cases} \hat{\chi}_t \text{ if } y_j \text{ is the neighbor } y_{i\circ t}^{(8)} \text{ of } x_i,\ t = 1,2,3,4. \\ 0, \text{ Otherwise} \end{cases}$$

Therefore, the estimated block of pixels are, as the solution of (4.10):

$$\boldsymbol{x} = \mathbf{F}\boldsymbol{y}, \quad \text{where} \quad \mathbf{F} = (\mathbf{C}^T\mathbf{C})^{-1}\mathbf{C}^T\mathbf{D} \tag{4.13}$$

As can be seen from (4.13), each missing pixel x_i is estimated as a linear combination of all the available LR pixels $\boldsymbol{y}$ in the block, where the weights are specified by the i^{th} row of the matrix $\mathbf{F}$ which is constructed by matrices C and D. Although the autoregression model parameters $\boldsymbol{\chi}$ and $\boldsymbol{\tau}$ appear to relate x_i to its immediate 8-connected or 4-connected neighbors only, the net effect of soft-decision block estimation is to interpolate x_i using all known pixels $\boldsymbol{y}$ in a local window. This is

equivalent to an adaptive non-separable two dimensional interpolation filter whose order is the same as the block size of soft-decision estimation, which distinguishes the SAI technique from the existing adaptive image interpolation methods.

Clearly, the computation bottleneck of the SAI algorithm is in solving (4.13). Inverting the 12×12 matrix (4.13) is expensive. Instead, we use the conjugate gradient method, which ensures global minimum for the objective function (4.10) is convex. In particular, by exploiting the overlaps of moving windows, we can launch the conjugate gradient algorithm from a good initial point to achieve fast convergence. Referring to Fig. 4.5, we see that eight of the twelve unknown pixels in the current octagonal window have at least one estimate obtained when the adjacent windows to the north, northwest, northeast and west were processed. Due to spatial coherence of the HR image, these estimates are statistically good initial values of the corresponding variables in the objective function. For the other four unknown pixels which have no estimates yet, we use results of a traditional interpolation method (e.g., bicubic interpolation) as the initial estimates. With this initialization the steepest descent algorithm can converge in three iterations on average in our experiments. Also note matrix $\mathbf{C}$ is quite sparse with only 49 out of 252 elements being nonzero. This sparsity of $\mathbf{C}$ can be exploited to save computations.

Another way of reducing computation complexity is to perform soft-decision estimation only in areas of high activities, because simple methods, such as bicubic interpolation, suffice to interpolate smooth two-dimensional waveforms. We classify the high activity areas based on the local variances estimated from LR pixels. If the local variance is above a threshold, the pixel is declared in the area of high activities. We empirically find that the variance threshold value of 100 realizes a good trade-off between complexity and performance. Fortunately, since most natural images have an exponentially decaying power spectrum, only a small fraction of pixels (10% to 25% under the above threshold) need to be interpolated by the soft-decision method to ensure good visual quality.

4.6 Experimental Results and Remarks

Extensive experiments were conducted to evaluate the proposed new image interpolation technique in comparison with its predecessors. For thoroughness and fairness of our comparison study, we selected a large set of test images, including some of more difficult cases for image interpolation. Fig. 4.6 lists eight example images in our test set, some of which were also used as test images in existing literatures of image interpolation.

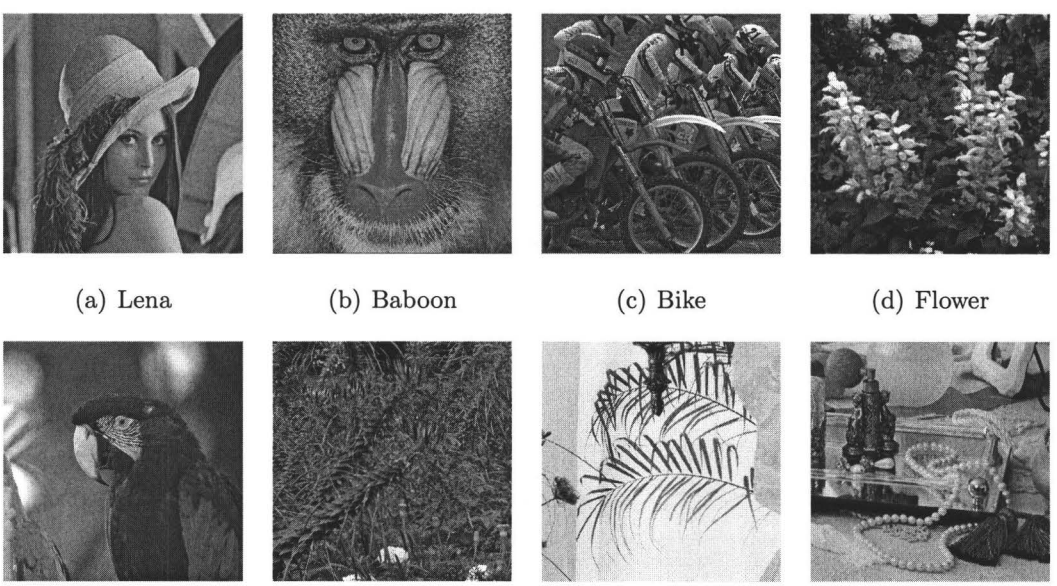

(a) Lena (b) Baboon (c) Bike (d) Flower

(e) Parrot (f) Bush (g) Leaves (h) Necklace

Figure 4.6: Eight sample images in the test set.

The comparison group includes four other image interpolation methods: bicubic interpolation [7], subpixel edge localization [33], new edge directed interpolation (NEDI) [3], and fused bidirectional interpolation [42]. Table 4.1 tabulates the PSNR results of the five different methods when applied to the eight test images of Fig. 4.6. On all instances, the proposed SAI algorithm consistently ranks the first among all methods in terms of PSNR performance. On images of rich high frequency components, such as Leaves and Bikes, the SAI algorithm exceeds the PSNR values of the

Table 4.1: PSNR (dB) results of the reconstructed HR images by different methods. The number in parentheses is the rank of the method. For the SAI algorithm, its gain in dB over the second best method is also given.

Image	Bicubic	Method in [33]	NEDI [3]	Method in [42]	SAI
Lena	33.92 (3)	33.09 (5)	33.76 (4)	33.92 (2)	**34.74** (1; 0.81dB)
Flower	32.30 (2)	30.18 (5)	30.47 (4)	31.89 (3)	**32.51** (1; 0.21dB)
Leaves	30.52 (4)	30.25 (5)	30.68 (3)	30.73 (2)	**32.16** (1; 1.43dB)
Baboon	22.92 (3)	22.84 (4)	23.10 (2)	22.79 (5)	**23.28** (1; 0.18dB)
Bush	26.34 (2)	25.79 (3)	25.53 (5)	25.79 (4)	**26.56** (1; 0.22dB)
Necklace	31.63 (2)	30.75 (5)	30.84 (4)	31.35 (3)	**31.89** (1; 0.36dB)
Bike	25.53 (3)	25.39 (4)	25.35 (5)	25.64 (2)	**26.53** (1; 0.89dB)
Parrot	35.80 (2)	35.26 (5)	35.61 (3)	35.46 (4)	**36.32** (1; 0.52dB)
Average	29.87 (2)	29.19 (5)	29.42 (4)	29.70 (3)	**30.51** (1; 0.64dB)

second best method by 1dB or more. Since PSNR is an average quality measure, we plot in Fig. 4.7 the spatial locations where the SAI algorithm produces significantly smaller interpolation errors than the competing methods for more localized image quality assessment. The intensity level of the plots represents the magnitude of reduction in interpolation error by the new method from the competing method. Fig. 4.7 clearly demonstrates the advantage of the SAI algorithm in reproducing the high frequency image constructs (edges and textures) over the other methods.

Given the fact that the human visual system is sensitive to errors near edges which signify object shapes and inter-object relationship, one can expect from the spatial patterns of Fig. 4.7 that the SAI algorithm should achieve superior visual quality. Figs. 4.8 through 4.11 compare the results of the five different image interpolation methods on test images Bike, Lena, Bush, and Flower, respectively. Different visual characteristics of the evaluated methods are exhibited near edges and fine textures in

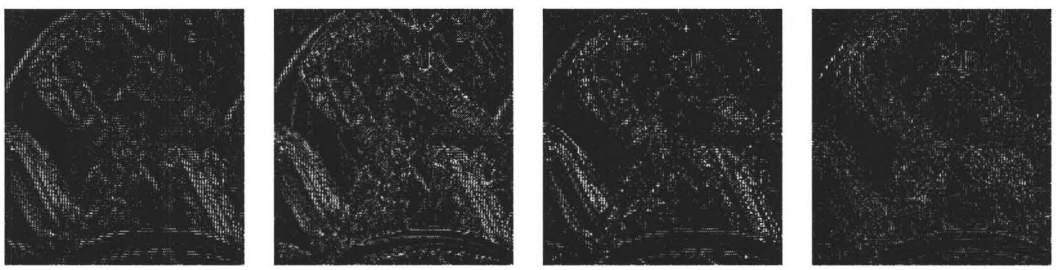

(a) Bicubic (b) Method [33] (c) Method [42] (d) NEDI [3]

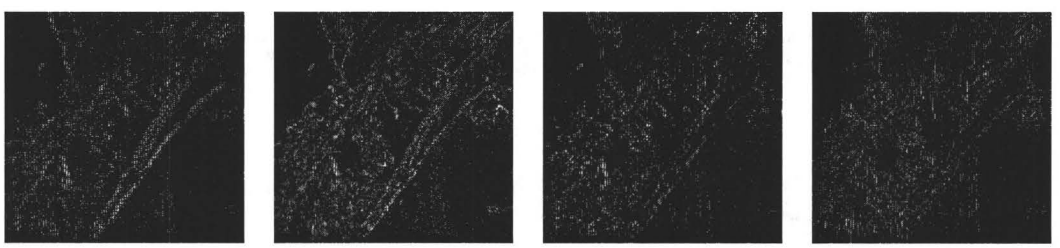

(e) Bicubic (f) Method [33] (g) Method [42] (h) NEDI [3]

Figure 4.7: Pixel locations where the SAI algorithm has smaller interpolation errors than the competing methods (only those of difference 3 or greater are plotted) on Bike and Lena images. The intensity level represents the magnitude of reduction in interpolation error by the proposed method from the competing method.

the test images.

The bicubic interpolation method tends to blur the image details more than other methods, and it also generates prominent jaggies along sharp edges. This method is in general inferior to the others in visual quality despite its PSNR measure is the second highest on average, next only to the proposed new method.

The method of subpixel edge localization [33] reproduces sharp edges, but the reconstructed edges are somewhat contrived and at times unnatural. This problem is exemplified by the reconstructed flower petals in Fig. 4.11(c), and by the rim of hat in test image Lena Fig. 4.9(c). This method consistently ranks lower than others in terms of PSNR.

The NEDI method [3] is very competitive in terms of visual quality. This is

primarily because it preserves long edges well. But in high activity areas where features have small curvatures or multiple edges intersect, this method sometimes generates speckle interpolation noises and ringing artifacts, as shown in Fig. 4.8(e) and Fig. 4.11(e), and more clearly in close-up parts of the reconstructed images in Fig. 4.12. Such flaws are the reason that this method only ranks the forth in PSNR in the comparison group of five methods, although it achieves pleasant visual effects on large edge structures.

The fused bidirectional interpolation method [42] takes a middle ground between the direction-less bicubic interpolation and edge-directed interpolation. It reproduces sharper large scale edges than the bicubic method, but the reconstruction is not as good as the method of [3] when the LR image contains enough information to correctly learn the edge direction. However, on small scale features where the edge direction learnt from the LR image is not reliable, this method can reduce speckle interpolation noises via the MMSE fusion process. It is interesting to note that the fusion method ranks in between the bicubic method and the method of [3] in PSNR.

As being evident in Figs. 4.8 through 4.11, the SAI algorithm eliminates most of the visual defects associated with the other methods. It reproduces visually more pleasant HR images than NEDI method that is considered as one of the best so far. Please refer to Fig. 4.12 for a side-by-side comparison between the two methods. Of particular significance is the fact that the SAI algorithm obtains superior visual quality on image features of large and small scales alike. This robustness is attributed to the soft-decision estimation technique that enforces the spatial coherence of estimated pixels according to the PAR model.

Although the proposed SAI algorithm is presented to double the horizontal and vertical resolutions, it can be readily generalized to scaling factor $\alpha = 2^z$ with z being a positive integer. One can simply apply the proposed SAI algorithm z times to scale the input image by α times. For an arbitrary scaling factor α (not an integer power of two), the interpolation can be done by first using the SAI algorithm to expand the

input image by 2^z times such that $2^z < \alpha < 2^{z+1}$, and then applying a conventional image interpolation algorithm, such as bicubic or bilinear interpolation, to scale up the output image of the new method by s times such that $2^z s = \alpha$. Fig. 4.13 is an example for scaling factor of 3, and it shows that the image interpolated by the SAI algorithm followed by bicubic interpolation has better visual quality than the image by bicubic interpolation only.

As described in section 4.4, the estimation of model parameters assumes that the spatial correlation between the HR pixels is approximately the same as between LR pixels. When this assumption is violated, the SAI algorithm may introduce some false edges or textures due to over-fitting of LR data. This over-fitting problem can be seen in Fig. 4.14. For this particular test image the spatial correlation changes after down sampling, which causes the SAI algorithm to produce erroneous textures. There is a way to detect where the over-fitting problem will likely occur. If the value of the cost function (4.5) at the convergence of the SAI algorithm is above a threshold, then chances are that the PAR model is not valid in the locality. As a recourse one can switch to a more conservative method such as bicubic interpolation to prevent the generation of false pixel structures. But this also tends to blur some sharp edges.

4.7 Conclusion

A novel soft-decision approach is proposed for adaptive image interpolation. When coupled with a PAR image model, the soft-decision approach estimates a block of missing pixels jointly by imposing an adaptively learnt spatial sample relation not only between known pixels and missing pixels but also between missing pixels themselves. This new image interpolation technique outperforms the existing methods in both PSNR measure and subjective visual quality over a wide range of scenes, by preserving the spacial coherence of the reconstructed high-resolution image on features of large and small scales alike.

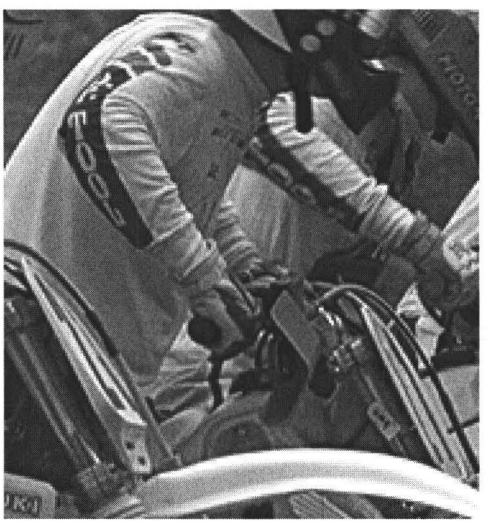

(a) Original HR image

(b) Bicubic interpolation

(c) Method in [33]

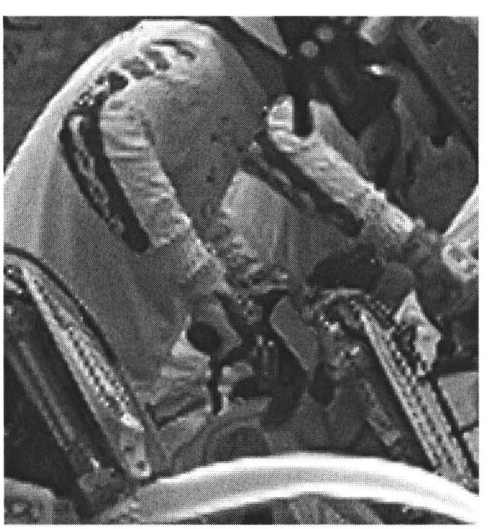

(d) Method in [42]

Figure 4.8: Comparison of different methods on Bike image (to be continued).

(e) NEDI

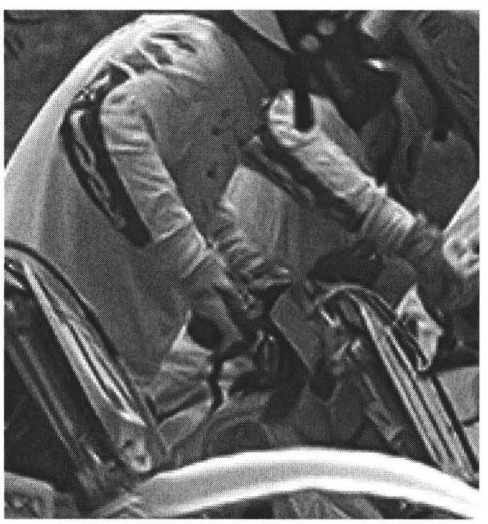

(f) SAI

Figure 4.8: Comparison of different methods on Bike image (Cont'd.).

(a) Original HR image

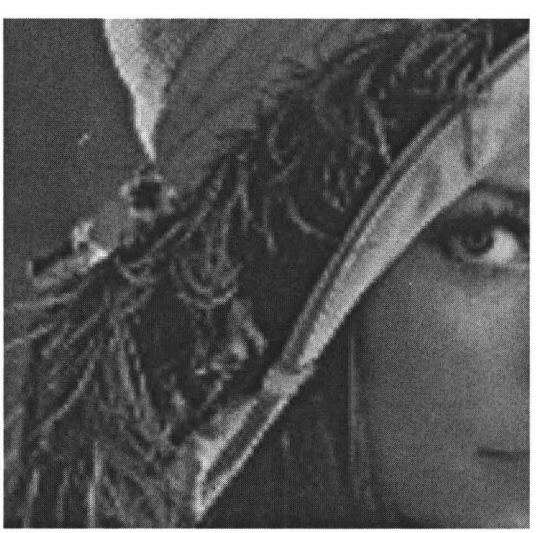

(b) Bicubic interpolation

Figure 4.9: Comparison of different methods on Lena image (to be continued).

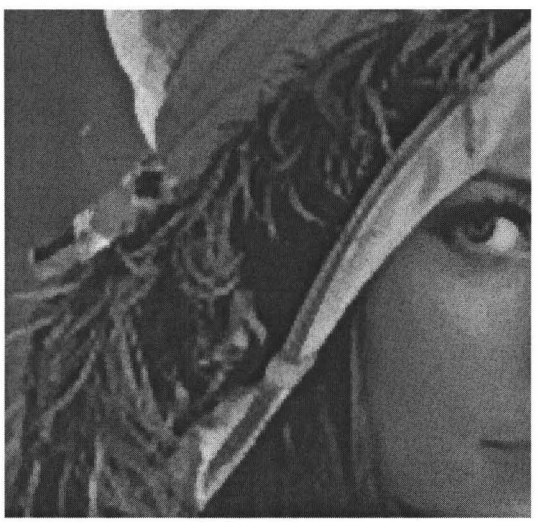

(c) Method in [33]

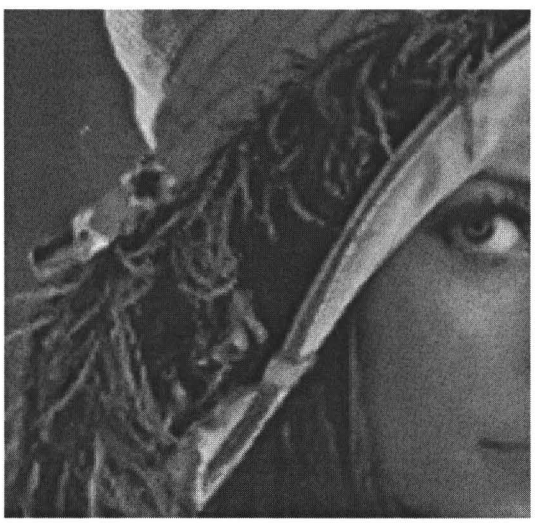

(d) Method in [42]

(e) NEDI

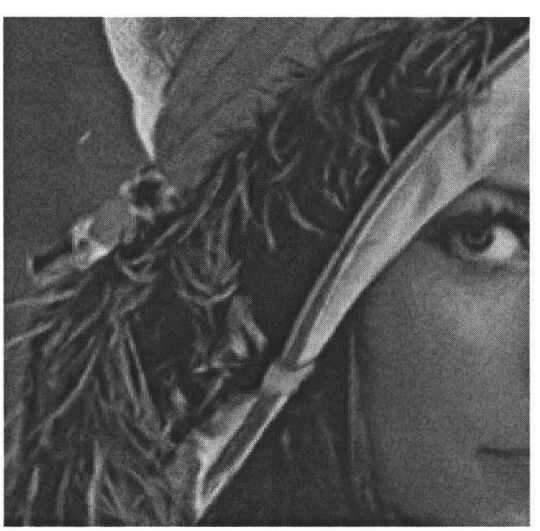

(f) SAI

Figure 4.9: Comparison of different methods on Lena image (Cont'd.).

(a) Original HR image

(b) Bicubic interpolation

(c) Method in [33]

(d) Method in [42]

Figure 4.10: Comparison of different methods on Bush image (to be continued).

(e) NEDI

(f) SAI

Figure 4.10: Comparison of different methods on Bush image (Cont'd.).

(a) Original HR image

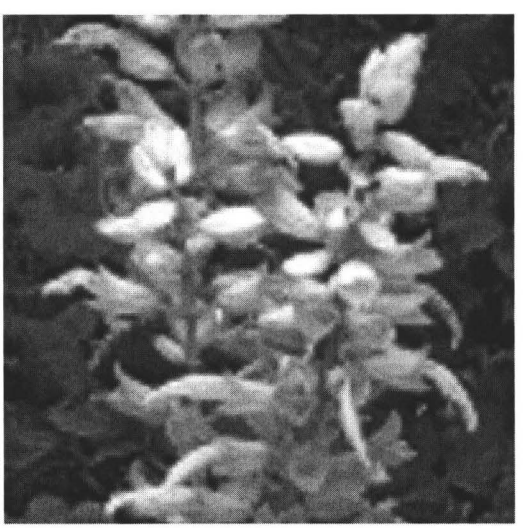

(b) Bicubic interpolation

Figure 4.11: Comparison of different methods on Flower image (to be continued).

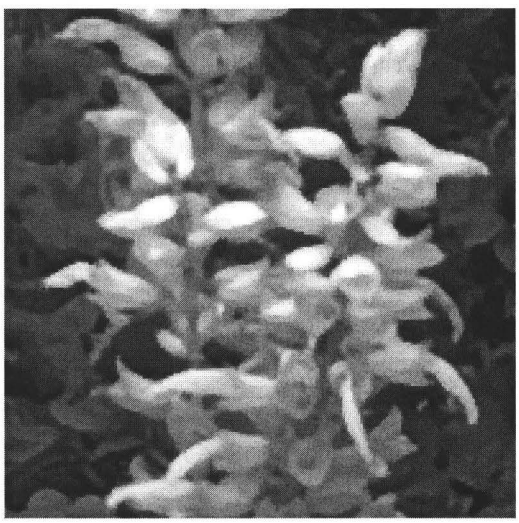

(c) Method in [33]

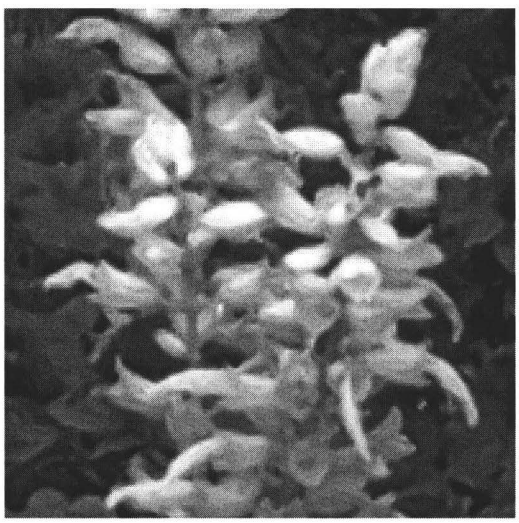

(d) Method in [42]

(e) NEDI

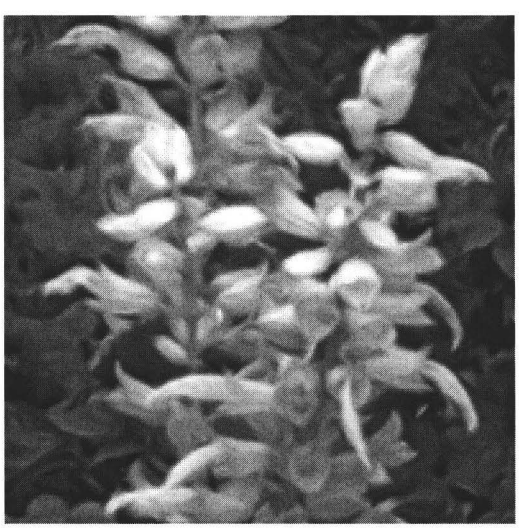

(f) SAI

Figure 4.11: Comparison of different methods on Flower image (Cont'd.).

(a) NEDI

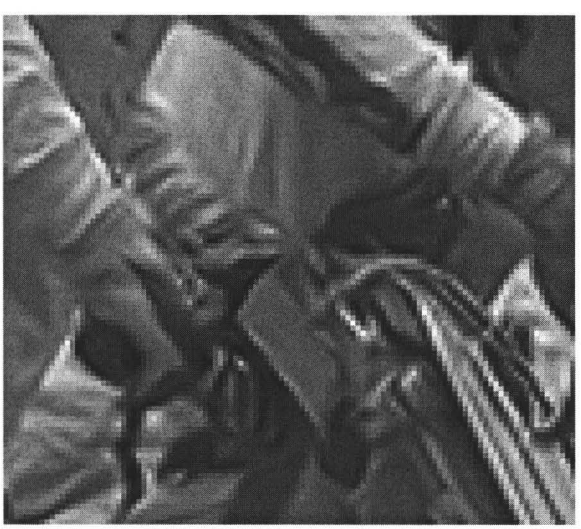

(b) SAI

Figure 4.12: Reconstructed images enlarged to compare the edge-directed interpolation method and the SAI algorithm (to be continued).

(c) NEDI

(d) SAI

(e) NEDI

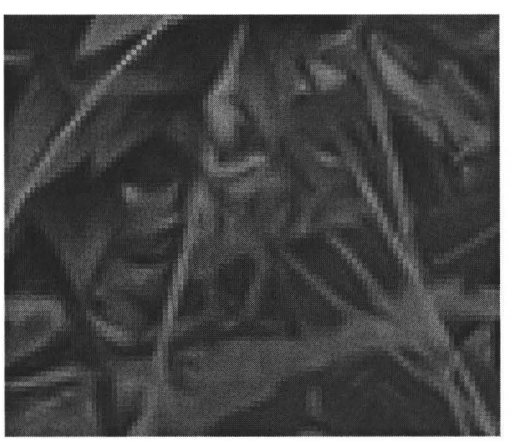

(f) SAI

Figure 4.12: Reconstructed images enlarged to compare the edge-directed interpolation method and the SAI algorithm (Cont'd.).

(a) (b)

Figure 4.13: Images scaled up by 3 times using different methods: (a) the bicubic method; (b) the SAI algorithm followed by the bicubic interpolation (i.e., first scaling by a factor of 2 and then by a factor of 1.5).

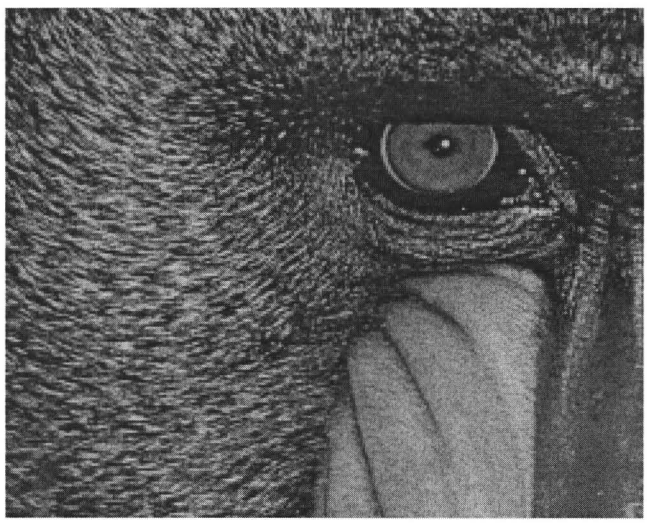

(a)

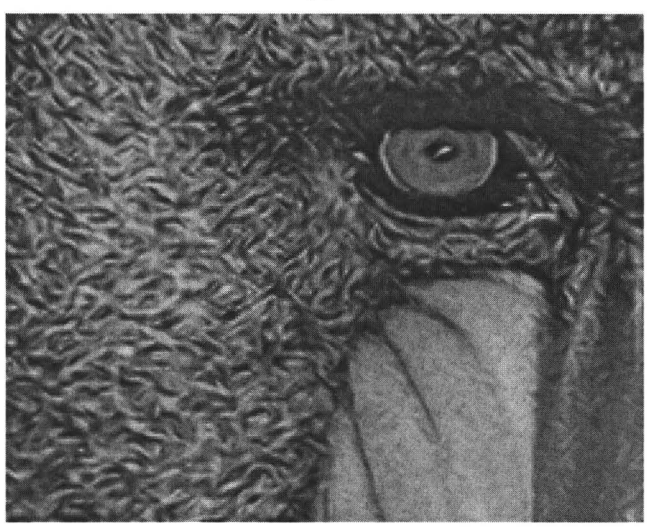

(b)

Figure 4.14: Visual effects of over-fitting of LR data. (a) Original image; (b) The output image of the SAI algorithm without safe guard against over-fitting.

Chapter 5

Model-based Non-linear Restoration

This chapter presents the most sophisticated image interpolation method developed in this thesis research. This method improves its predecessors, including the previous two methods, in two aspects. Firstly, a realistic model of LR image formation from the corresponding HR image is integrated into the interpolation process. As such, upsampling and deconvolution can be performed jointly rather than separately as in existing methods, which improves interpolation performance by factoring in the effect of the point spread function (PSF). Secondly, the new method can work with an arbitrary scaling factor while the previous methods are restricted to scaling factors that are power of two.

5.1 Overview

As discussed in the previous chapter, the adaptability of the SAI algorithm comes from a 2D PAR image model that can adapt to varying two-dimensional image signal waveform. However, the SAI algorithm still suffers from a serious deficiency of modeling like its predecessors [3, 41]: the image model is learnt from the LR image but

applied to reconstruct the HR image. The issue here is one of chicken and egg. On one hand, correct interpolation of missing pixels relies on a good model of HR image; on the other hand, the model can be built only if the missing pixels are known. To resolve this dilemma, we propose a new image interpolation technique that jointly estimates the parameters of the PAR model and the pixels of the HR image. We cast the joint estimation task as a constrained nonlinear least square problem having PAR model parameters and HR pixels both as unknown variables. The new technique of non-linear estimation for adaptive resolution upconversion (NEARU) aims to achieve the best possible statistical agreement between the estimated PAR model and the estimated HR image, constrained by the known LR image. For typical applications of image resolution upconversion, the constraint of NEARU is given by the PSF that produces the LR image from the HR image. Algorithmically, the problem of NEARU can be solved by the structured total least-square method.

The NEARU technique has two distinct advantages over its predecessors. Firstly, NEARU provides a unified platform for adaptive interpolation (upsampling) and deconvolution (sharpening). Up to now almost all published image interpolation algorithms ignored the effect of PSF. Previous authors presumably meant to perform deconvolution in a separate step after interpolation. However, this separation approach is problematic because image deconvolution is highly susceptible to noises. The problem is made even worse by the fact that the interpolation noises are signal dependent. We fix the flaw of the separation approach by performing interpolation and deconvolution joint in a single non-linear estimation framework, in which the impact of PSF on the PAR image model is directly factored in the objective function. Further, the unified framework is capable of pixel-level adaptation. As a result, the HR images reconstructed by NEARU are sharper, cleaner, and have far less artifacts than the existing methods. Secondly, the NEARU technique can resize the LR image by an arbitrary factor with ease in a single pass of the LR image, whereas other adaptive image interpolation techniques, such as the NEDI method in [3] and our previous

two methods, need to make two passes of the LR image and perform interpolation in different orientations, and they do not lend themselves conveniently to scaling factors other than power of two. The performance gap in visual quality between NEARU and other methods increases as the scaling factor gets larger. This is an important property in applications involving very large images, such as the printing of big posters for advertisement or homes, and cover pages in prepress.

The rest of the chapter is structured as follows. Section 5.2 formulates the problem of joint image interpolation-deconvolution as a model-based non-linear estimation problem. The selection of the image models is discussed. Section 5.3 develops a structured total least squares (STLS) solution for the formulated NEARU problem. Section 5.4 introduces a technique to estimate the PAR model parameters from the observed LR image. This technique is based on a property of 2D autoregressive process degraded by PSF. Section 5.5 reports experimental results and a comparison study on some existing popular image interpolation methods. Section 5.6 concludes.

5.2 Model-based nonlinear block estimation

In this chapter, we assume that the observed LR image is generated from a HR image by filtering with a known PSF and downsampling. Let I_h be the HR image to be reconstructed, and I_l be the observed LR image. We register the pixels in I_h and I_l in the same coordinate system. For convenience of notation, let the sampling center of each pixel be the location of this pixel. We denote the pixel of I_h located at (i, j) as $x(i, j)$, and the pixel of I_l located at $(\imath, \jmath)$ as $y(\imath, \jmath)$. The pixels of I_h have integer coordinates, i.e., $i = 1, 2, ..., M$ and $j = 1, 2, ..., N$, where M and N are the number of rows and columns of the HR image; the locations of LR pixels with an arbitrary scaling factor α are indexed by $(\imath, \jmath)$ such that $\imath = 1 + k\alpha$, $k = 0, 1, 2, ..., \lfloor M\alpha \rfloor - 1$ and $\jmath = 1 + k\alpha$, $k = 0, 1, 2, ..., \lfloor N\alpha \rfloor - 1$. An example of this sampling relationship between the HR and LR images is illustrated in Fig. 5.1. The scaling factor α in this

example is 1.5. In the figure, the circles identify the positions of the HR pixels and the crosses show the sampling locations of the LR pixels. Each LR pixel covers a block of its neighboring HR pixels via PSF.

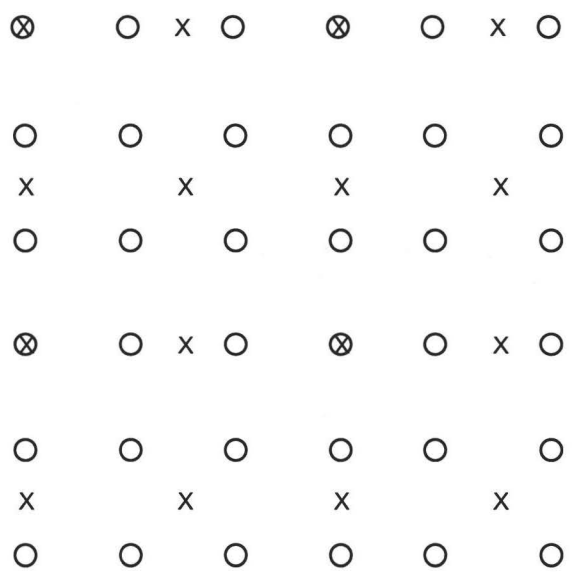

Figure 5.1: Sampling relationship between the HR and LR. The scaling factor shown here is 1.5. The circles are locations of HR pixels and the crosses are locations of LR pixels. Each LR pixel corresponds to a block of HR pixels through the filtering operation with a known PSF.

The premise of the NEARU method is that image signal is a 2D PAR process. As such, we take an approach of block or windowed estimation for image interpolation, which is the same as the previous SAI method. In a local window W, our task is to jointly estimate the parameters of the autoregressive process and the block of HR pixels $\boldsymbol{x} \in W$ such that the estimated PAR model can optimally fit the estimated $\boldsymbol{x}$. One can expect a good fit of $\boldsymbol{x} \in W$ to an autoregressive process because common image constructs, such as edges and surface textures, have consistent second order statistics in a locality. For the minimum mean squares criterion, the problem of joint image interpolation-deconvolution can be formulated as the following constrained

optimization problem:

$$\min_{\boldsymbol{x},\boldsymbol{a}} \sum_{(i,j)\in W} \left(x(i,j) - \sum_{u,v} a_{u,v} x(i-u, j-v) \right)^2 \qquad (5.1)$$
$$\text{subject to} \quad \boldsymbol{x} * \boldsymbol{h} = \boldsymbol{y}$$

where $\boldsymbol{a}$ is the vector of parameters of a 2D autoregressive model defined in local window W. The constraints $\boldsymbol{x} * \boldsymbol{h} = \boldsymbol{y}$ in (5.1) correspond to the physical formation of the LR image via a still camera, where $*$ is the convolution operator, and vector $\boldsymbol{x}$ consists of all the HR pixels and vector $\boldsymbol{y}$ of all the LR pixels inside window W. Since the operator $*$ is linear, $\boldsymbol{x} * \boldsymbol{h} = \boldsymbol{y}$ generates L equality constraints, L being the number of the LR pixels inside W (i.e., the length of vector $\boldsymbol{y}$).

However, at onset the objective function (5.1) presents a problem of data overfitting, or curse of dimensionality. If a PAR model of order t (i.e., the length of vector $\boldsymbol{a}$ is t) is used, then the number of variables in (5.1) is $|W| + t$, whereas the number of equations between these variables is only $|W| + L$. From the spatial configuration of LR pixels $\boldsymbol{y}$ in relation to HR pixels $\boldsymbol{x}$, we have $L \leq \frac{|W|}{\alpha^2}$. The ratio of the number of equations versus the number of unknown variables is bounded from above by

$$\frac{|W|(1+\frac{1}{\alpha^2})}{|W|+t} = \frac{1+\frac{1}{\alpha^2}}{1+\frac{t}{|W|}} \leq 1 + \frac{1}{\alpha^2} \qquad (5.2)$$

Since the scaling factor $\alpha > 1$ for image resolution upconversion, the number of equations (i.e., the number of samples in the underlying estimation problem) is very close to the number of unknown variables, almost independent of t. This exposes an acute data overfitting problem facing NEARU, which cannot be prevented merely by lowering the order of the PAR model t.

On a second reflection, fortunately, the two dimensions of the image signal afford us ways to circumvent the problem of data overfitting. One way to increase the number of equations or constraints on pixels $\boldsymbol{x} \in W$ is the use of multiple PAR models that associate pixels in different directions. Specifically, we introduce two PAR models of order 4, called the diagonal model $\mathcal{AR}_\times$ and the axial model $\mathcal{AR}_+$.

The models $\mathcal{AR}_\times$ and $\mathcal{AR}_+$ act on two disjoint neighborhoods of $x(i,j)$:

$$\begin{aligned}\mathbf{s}_+(i,j) &= [x(i,j-1), x(i-1,j), x(i,j+1), x(i+1,j)]^T \\ \mathbf{s}_\times(i,j) &= [x(i-1,j-1), x(i-1,j+1), x(i+1,j+1), x(i+1,j-1)]^T.\end{aligned} \tag{5.3}$$

Vectors $\mathbf{s}_\times(i,j)$ and $\mathbf{s}_+(i,j)$ consist of four 8-connected neighbors and four 4-connected neighbors of $x(i,j)$ in the HR image, respectively, explaining our terminology of diagonal and axial models. Incorporating these two PAR models into the original nonlinear estimation framework, we modify the objective function (5.1) to the following:

$$\begin{aligned}&\min_{\boldsymbol{x},\boldsymbol{\chi},\boldsymbol{\tau}}\Big\{\sum_{(i,j)\in W}(x(i,j)-\boldsymbol{\chi}^T\mathbf{s}_\times(i,j))^2+\sum_{(i,j)\in W}(x(i,j)-\boldsymbol{\tau}^T\mathbf{s}_+(i,j))^2\Big\} \\ &\text{subject to}\quad \boldsymbol{x}*\boldsymbol{h}=\boldsymbol{y}\end{aligned} \tag{5.4}$$

where $\boldsymbol{\chi}=(\chi_1,\chi_2,\chi_3,\chi_4)$ and $\boldsymbol{\tau}=(\tau_1,\tau_2,\tau_3,\tau_4)$ are parameters of the two PAR models $\mathcal{AR}_\times$ and $\mathcal{AR}_+$, respectively. From (5.1) to (5.4) the number of equations increases from $|W|+L$ to $2|W|+L$. While the number of equations is almost doubled, the number of unknown variables increases only by $t=4$. Consequently, the ratio of the number of equations versus the number of unknown variables is increased to

$$\frac{|W|(2+\frac{1}{\alpha^2})}{|W|+8}=\frac{2+\frac{1}{\alpha^2}}{1+\frac{8}{|W|}} \tag{5.5}$$

For example, if the above ratio is required to be 2 for robust estimation, we need to select a window size $|W|\geq 16\alpha^2$. To prevent the overfitting problem, we prefer a large window W in block estimation of NEARU. However, a large window W has a higher chance of violating the assumption that the image signal is a stationary AR process in W. In balance, we choose the window size that makes the above ratio in the range of 1.5 to 2.

The NEARU framework is general and the regularization term $\boldsymbol{h}$ in (5.4) can be any degradation function (e.g., PSF compounded by camera motion). To keep this chapter focused on resolution upconversion we consider only the effect of PSF via $\boldsymbol{h}$. The incorporation of PSF in the framework of NEARU unifies the operations of

image upconversion and deconvolution, which were otherwise performed in two separate steps in current practice. Unlike many existing image interpolation techniques, NEARU does not treat the pixels of the LR image as ground truth and will change these LR pixel values as a result of the non-linear least-squares estimation. Also, since the constraint $\boldsymbol{x} * \boldsymbol{h} = \boldsymbol{y}$ can accommodate any ratio between the HR and LR image sizes, NEARU offers a solution of joint upconversion-deconvolution for an arbitrary scaling factor.

To adapt to possible drifting statistics in image space, the NEARU technique solves the optimization problem (5.4) in blocks. Adjacent blocks may overlap one the other to avoid blocking effects. In each local window W, as stipulated by the objective function (5.4), the parameters of models $\mathcal{AR}_\times$ and $\mathcal{AR}_+$ are jointly estimated with HR pixels $\boldsymbol{x}$. This is a strategy to circumvent the chicken-and-egg dilemma of having to use the second order statistics of the LR image to interpolate the HR image, as proposed in [3]. Since NEARU estimates, in least-squares sense, a whole block of HR pixels $\boldsymbol{x} \in W$, rather than pixel by pixel in isolation, it is an alternative to Markov field approach for image interpolation.

Although we adopt two PAR models $\mathcal{AR}_\times$ and $\mathcal{AR}_+$ of order 4 only for the sake of preventing model overfit, the block estimation process of NEARU has the net effect of an adaptive non-separable two dimensional interpolation filter that has as many as L taps. Namely, each HR pixel is interpolated using all LR pixels $\boldsymbol{y} \in W$.

5.3 Structured total least-squares solution

By applying a Lagrangian multiplier λ, we convert the above constrained nonlinear least square problem to the following unconstrained nonlinear least square problem:

$$\min_{\boldsymbol{x},\boldsymbol{\chi},\boldsymbol{\tau}} \Big\{ \sum_{(i,j)\in W} (x(i,j) - \boldsymbol{\chi}^T \mathbf{s}_\times(i,j))^2 + \sum_{(i,j)\in W} (x(i,j) - \boldsymbol{\tau}^T \mathbf{s}_+(i,j))^2 + \lambda ||\boldsymbol{y} - \boldsymbol{x} * \boldsymbol{h}||^2 \Big\} \tag{5.6}$$

The value of λ is chosen according to the certainty about the underlying PSF $\boldsymbol{h}$. In the case that $\boldsymbol{h}$ is exactly known, λ can be set to a large value, such as 100.

For convenient representation we rewrite (5.6) in matrix form:

$$\min_{\boldsymbol{x},\chi,\tau}\Big\{\|\boldsymbol{x}-\mathbf{C}_1\boldsymbol{x}\|^2+\|\boldsymbol{x}-\mathbf{C}_2\boldsymbol{x}\|^2+\lambda\|\boldsymbol{y}-\mathbf{C}_3\boldsymbol{x}\|^2\Big\} \tag{5.7}$$

where $\mathbf{C}_1$ and $\mathbf{C}_2$ are two matrices with dimension of $|W|\times|W|$, $|W|$ being the number of HR pixels in W. Specifically,

$$\mathbf{C}_1(m,n)=\begin{cases}\chi_t, & \text{if } x_m \text{ is the } t^{th} \text{ element of } \mathbf{s}_\times(i,j) \text{ where } (i,j) \text{ is the coordinate}\\ & \text{of pixel } x_n,\ t=1,2,3,4.\\ 0, & \text{otherwise}\end{cases}$$

$$\mathbf{C}_2(m,n)=\begin{cases}\tau_t, & \text{if } x_m \text{ is the } t^{th} \text{ element of } \mathbf{s}_+(i,j) \text{ where } (i,j) \text{ is the coordinate}\\ & \text{of pixel } x_n,\ t=1,2,3,4.\\ 0, & \text{otherwise}\end{cases} \tag{5.8}$$

Matrix $\mathbf{C}_3$ in (5.7) corresponds to the convolution operation. Since the convolution is linear operation, we can construct a matrix $\mathbf{C}_3$ where $\mathbf{C}_3\boldsymbol{x}=\boldsymbol{x}*\boldsymbol{h}$. Specifically, the matrix $\mathbf{C}_3$ has the dimension of $L\times|W|$ and is constructed as following: $\mathbf{C}_3(m,n)=\boldsymbol{h}(i-\imath,j-\jmath)$, where (i,j) is the coordinate of pixel x_n and $(\imath,\jmath)$ is the coordinate of pixel y_m.

Define the residue vector $\boldsymbol{r}(\boldsymbol{x},\chi,\tau)$ as

$$\boldsymbol{r}(\boldsymbol{x},\chi,\tau)=\begin{bmatrix}\boldsymbol{r}_1(\boldsymbol{x},\chi)\\ \boldsymbol{r}_2(\boldsymbol{x},\tau)\\ \boldsymbol{r}_3(\boldsymbol{x})\end{bmatrix} \tag{5.9}$$

where

$$\begin{aligned}\boldsymbol{r}_1(\boldsymbol{x},\chi)&=(\mathbf{I}-\mathbf{C}_1)*\boldsymbol{x}\\ \boldsymbol{r}_2(\boldsymbol{x},\tau)&=(\mathbf{I}-\mathbf{C}_2)*\boldsymbol{x}\\ \boldsymbol{r}_3(\boldsymbol{x})&=\sqrt{\lambda}(\boldsymbol{y}-\mathbf{C}_3*\boldsymbol{x})\end{aligned} \tag{5.10}$$

and present the inverse problem (5.7) in the following quadratic form:

$$\min_{\boldsymbol{x},\chi,\tau} \boldsymbol{r}(\boldsymbol{x},\chi,\tau)^T \boldsymbol{r}(\boldsymbol{x},\chi,\tau) \tag{5.11}$$

The least-squares problem (5.11) is nonlinear, because HR pixels $\boldsymbol{x}$ and model parameters χ and τ are all unknown and there are product terms between $\boldsymbol{x}$ and χ and between $\boldsymbol{x}$ and τ. A general nonlinear least squares algorithm can be found in [75]. However, the problem (5.11) has some structures. Note that the residue vector $\boldsymbol{r}(\boldsymbol{x},\chi,\tau)$ is linear in $\boldsymbol{x}$ and the matrices $\mathbf{C}_1$ and $\mathbf{C}_2$ are functions of χ and τ only. These properties make (5.11) to be of the type of separable nonlinear least squares [76]. To exploit these structures, we develop an iterative algorithm based on the methodology of structured total least squares [77]. First, we linearize the residue vector $\boldsymbol{r}(\boldsymbol{x},\chi,\tau)$. Let $\Delta\boldsymbol{x}$, $\Delta\chi$, and $\Delta\tau$ represent small changes in $\boldsymbol{x}$, χ and τ respectively, the residue vector $\boldsymbol{r}(\boldsymbol{x},\chi,\tau)$ can be linearized as following:

$$\begin{aligned} \boldsymbol{r}(\boldsymbol{x}+\Delta\boldsymbol{x},\chi+\Delta\chi,\tau+\Delta\tau) &= \begin{bmatrix} \boldsymbol{r}_1(\boldsymbol{x}+\Delta\boldsymbol{x},\chi+\Delta\chi) \\ \boldsymbol{r}_2(\boldsymbol{x}+\Delta\boldsymbol{x},\tau+\Delta\tau) \\ \boldsymbol{r}_3(\boldsymbol{x}+\Delta\boldsymbol{x}) \end{bmatrix} \\ &= \begin{bmatrix} \boldsymbol{r}_1(\boldsymbol{x},\chi)+(\mathbf{I}-\mathbf{C}_1)\Delta\boldsymbol{x}-\mathbf{E}_1\Delta\chi \\ \boldsymbol{r}_2(\boldsymbol{x},\tau)+(\mathbf{I}-\mathbf{C}_2)\Delta\boldsymbol{x}-\mathbf{E}_2\Delta\tau \\ \boldsymbol{r}_3(\boldsymbol{x})-\sqrt{\lambda}\mathbf{C}_3\Delta\boldsymbol{x} \end{bmatrix} \end{aligned} \tag{5.12}$$

where E_1 and E_2 are two matrices with dimension of $|W|\times 4$ constructed as following: the m^{th} row of E_1 is $\mathbf{s}_\times(i,j)^T$ and the m^{th} row of E_2 is $\mathbf{s}_+(i,j)^T$, where (i,j) is the coordinate of pixel x_m.

Therefore, given the current estimates of the HR pixels $\boldsymbol{x}$ and the model parameters χ, τ, the minimization problem in (5.11) reduces to $\min_{\Delta\boldsymbol{x},\Delta\chi,\Delta\tau} \boldsymbol{r}(\boldsymbol{x}+\Delta\boldsymbol{x},\chi+\Delta\chi,\tau+\Delta\tau)$, which is

$$\min_{\Delta\boldsymbol{x},\Delta\chi,\Delta\tau} \left\| \begin{bmatrix} -\mathbf{I}+\mathbf{C}_1 & \mathbf{E}_1 & \mathbf{0} \\ -\mathbf{I}+\mathbf{C}_2 & \mathbf{0} & \mathbf{E}_2 \\ \sqrt{\lambda}\mathbf{C}_3 & \mathbf{0} & \mathbf{0} \end{bmatrix} \begin{bmatrix} \Delta\boldsymbol{x} \\ \Delta\chi \\ \Delta\tau \end{bmatrix} + \begin{bmatrix} -\boldsymbol{r}_1(\boldsymbol{x},\chi) \\ -\boldsymbol{r}_2(\boldsymbol{x},\tau) \\ -\boldsymbol{r}_3(\boldsymbol{x}) \end{bmatrix} \right\|^2 \tag{5.13}$$

The resulting $\Delta \boldsymbol{x}$, $\Delta \boldsymbol{\chi}$, and $\Delta \boldsymbol{\tau}$ are the updates of the estimates of HR pixels $\boldsymbol{x}$ and model parameters $\boldsymbol{\chi}$, $\boldsymbol{\tau}$ for the next iteration. In each iteration the least-squares problem (5.13) is linear with $\Delta \boldsymbol{x}$, $\Delta \boldsymbol{\chi}$, and $\Delta \boldsymbol{\tau}$ being variables, and hence it can be solved efficiently.

We present below in pseudocode the STLS algorithm for the proposed NEARU interpolation method. The HR pixels $\boldsymbol{x}$ and the PAR model parameters $\boldsymbol{\chi}$, $\boldsymbol{\tau}$ are jointly estimated in a local window W. At the initialization stage, given initial model parameters $\boldsymbol{\chi}^{(0)}$ and $\boldsymbol{\tau}^{(0)}$, the first estimates of $\boldsymbol{x}$ are produced by solving a linear least squares described in (5.14). In successive iterations, the updates of $\Delta \boldsymbol{x}$, $\Delta \boldsymbol{\chi}$, and $\Delta \boldsymbol{\tau}$ are obtained by solving another least square optimization problem (5.13). To speed up the algorithm we adopt the conjugate gradient method to solve these two linear least square problems, instead of directly using the closed form formula which requires inverting matrices of large size.

ALGORITHM STLS Joint estimation of a block of HR pixels and the PAR model parameters.

Input - Observed LR pixels $\boldsymbol{y}$ in window W, initial model parameters $\boldsymbol{\chi}^{(0)}$, $\boldsymbol{\tau}^{(0)}$, and the PSF $\boldsymbol{h}$.

Output - Estimated model parameters $\boldsymbol{\chi}$, $\boldsymbol{\tau}$, and the reconstructed HR pixels $\boldsymbol{x}$ in window W.

1. **Initialization:** Construct matrices $\mathbf{C}_1$, $\mathbf{C}_2$, and $\mathbf{C}_3$ from $\boldsymbol{\chi}^{(0)}$, $\boldsymbol{\tau}^{(0)}$, and $\boldsymbol{h}$. Solve the following linear least square problem for $\boldsymbol{x}^{(0)}$:

$$\min_{\boldsymbol{x}} \left\| \begin{bmatrix} \mathbf{0} \\ \mathbf{0} \\ \sqrt{\lambda}\boldsymbol{y} \end{bmatrix} - \begin{bmatrix} -\mathbf{I} + \mathbf{C}_1 \\ -\mathbf{I} + \mathbf{C}_2 \\ \sqrt{\lambda}\mathbf{C}_3 \end{bmatrix} \boldsymbol{x} \right\|^2 \tag{5.14}$$

2. **Iteration:** For the k-th step

   (a) Construct matrices $\mathbf{E}_1$ and $\mathbf{E}_2$ from the estimate: $\boldsymbol{x}^{(k-1)}$.

(b) Solve the linear least square optimization problem in (5.13) for $\Delta \boldsymbol{x}$, $\Delta \boldsymbol{\chi}$, and $\Delta \boldsymbol{\tau}$.

(c) Update: $\boldsymbol{x}^{(k)} = \boldsymbol{x}^{(k-1)} + \Delta \boldsymbol{x}$, $\boldsymbol{\chi}^{(k)} = \boldsymbol{\chi}^{(k-1)} + \Delta \boldsymbol{\chi}$, and $\boldsymbol{\tau}^{(k)} = \boldsymbol{\tau}^{(k-1)} + \Delta \boldsymbol{\tau}$.

(d) Construct matrices $\mathbf{C}_1$, $\mathbf{C}_2$, and calculate the new residue vector $\boldsymbol{r}^{(k)}$.

3. **Stop condition:** ($\|\Delta \boldsymbol{x}\| \leq \epsilon$, $\|\Delta \boldsymbol{\chi}\| \leq \epsilon$ and $\|\Delta \boldsymbol{\tau}\| \leq \epsilon$) or $\|r^{(k)}\|^2 > \|r^{(k-1)}\|^2$, where ϵ is a pre-defined stopping criterion.

5.4 Estimation of PAR Model Parameters

In general, the objective function (5.11) of NEARU is not convex, hence the way of initializing the iterative algorithm STLS is crucial to upconversion performance. The initialization steps involve the PAR model parameters. To proceed we need the following useful property of the 2D autoregressive process degraded by PSF $\boldsymbol{h}$.

Proposition 1. *If an original image is a 2D autoregressive (AR) process and it has been degraded by a given point spread function* $\boldsymbol{h}$*, then the degraded image is a 2D autoregressive moving average (ARMA) process. Its AR part has the same parameters as those of the original image, and its moving average (MA) part is determined by the parameters of* $\boldsymbol{h}$*.*

Proof: Consider a 2D AR process (HR image) $\boldsymbol{x}$ with parameters $\boldsymbol{a}$

$$x(i,j) = \sum_{u,v} a_{u,v} x(i-u, j-v) + e(i,j) \tag{5.15}$$

where $e(i,j)$ is white noise. Let $\boldsymbol{y}$ be the LR image generated from $\boldsymbol{x}$ by degradation with a 2D function (e.g., PSF) $\boldsymbol{h}$:

$$y(i,j) = \sum_{m,n} h(m,n) x(i-m, j-n). \tag{5.16}$$

It follows from

$$\begin{aligned}\sum_{u,v} a_{u,v} y(i-u, j-v) &= \sum_{u,v} a_{u,v} \sum_{m,n} h(m,n) x(i-u-m, j-v-n) \\ &= \sum_{m,n} h(m,n) \sum_{u,v} a_{u,v} x(i-u-m, j-v-n) \\ &= \sum_{m,n} h(m,n)(x(i-m, j-n) - e(i-m, j-n)) \\ &= y(i,j) - \sum_{m,n} h(m,n) e(i-m, j-n)\end{aligned} \tag{5.17}$$

that $\boldsymbol{y}$ is a 2D ARMA process

$$y(i,j) = \sum_{u,v} a_{u,v} y(i-u, j-v) + \sum_{m,n} h(m,n) e(i-m, j-n), \tag{5.18}$$

whose AR part is the same as $\boldsymbol{x}$ and whose MA part is given by $\boldsymbol{h}$. ■

The proposition suggests that we can estimate the PAR model parameters χ and τ for the original HR pixel block $\boldsymbol{x} \in W$ from the observed LR pixel block $\boldsymbol{y} \in W$. Therefore, we initialize the algorithm STLS by assuming $\boldsymbol{y}$ to be an autoregressive process of zero mean in local window W. Then by Proposition 1, we compute the initial PAR model parameters $\chi^{(0)}$ and $\tau^{(0)}$ via the following linear least square estimation:

$$\begin{aligned}\chi^{(0)} &= \arg\min_{\chi} \Big\{ \sum_{(\imath,\jmath)\in W} \big(y(\imath,\jmath) - \chi^T \mathbf{s}_\times(\imath,\jmath)\big)^2 \Big\} \\ \tau^{(0)} &= \arg\min_{\tau} \Big\{ \sum_{(\imath,\jmath)\in W} \big(y(\imath,\jmath) - \tau^T \mathbf{s}_+(\imath,\jmath)\big)^2 \Big\}\end{aligned}, \tag{5.19}$$

where $\mathbf{s}_\times(\imath,\jmath)$ and $\mathbf{s}_+(\imath,\jmath)$ are two four-dimensional vectors whose elements are the four 8-connected neighbors and four 4-connected neighbors of $y(\imath,\jmath)$ in the LR image, respectively. Note that these two vectors only contain the known LR pixels. The closed form solutions of (5.19) are

$$\begin{aligned}\chi^{(0)} &= (\mathbf{A}^T\mathbf{A})^{-1}\mathbf{A}^T\mathbf{y} \\ \tau^{(0)} &= (\mathbf{B}^T\mathbf{B})^{-1}\mathbf{B}^T\mathbf{y}\end{aligned} \tag{5.20}$$

where the column vector $\mathbf{y}$ consists of all the LR pixels $y(i,j)$ in the window W. Each row of the matrix $\mathbf{A}$ is the corresponding vector $\mathbf{s}_\times(i,j)$. And each row of the matrix $\mathbf{B}$ is the corresponding vector $\mathbf{s}_+(i,j)$.

5.5 Experimental Results and Remarks

In this section we evaluate the performance of the NEARU method in both PSNR measurement and visual quality. Same as in the previous chapter, we compare NEARU method with four existing interpolation methods: the bicubic interpolation method [7], the NEDI method [3], the fused bidirectional interpolation method of [42], and the subpixel edge localization method in [33]. All methods other than NEARU do not perform deconvolution in the interpolation process. To make fair comparisons, we also report the results of the other methods with a deconvolution step of Weiner filtering, assuming a known PSF in the simulation. A large set of test images was used to ensure the generality and validity of the experimental results. Fig. 5.2 lists ten sample images in the test set.

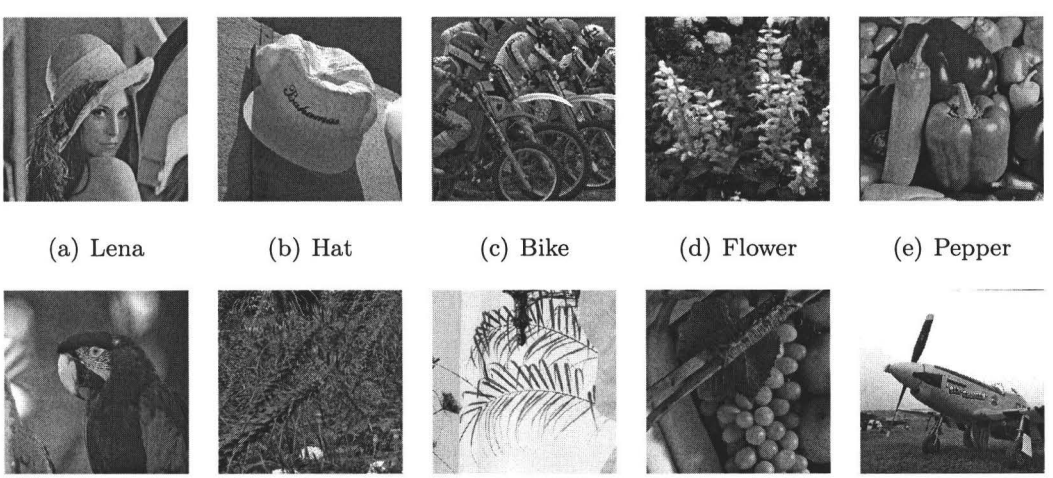

(a) Lena (b) Hat (c) Bike (d) Flower (e) Pepper

(f) Parrot (g) Bush (h) Leaves (i) Fruit (j) Flight

Figure 5.2: Ten sample images in the test set.

In our experiments LR images were simulated through low pass filtering and down-

sampling of the test images. The PSF used in the simulation is a 2D Gaussian filter with standard deviation of 0.6. Table 5.1 lists the PSNR results of the reconstructed HR images by the five methods. For the four methods that do not consider PSF we also include the PSNR values after Wiener deconvolution. Interestingly, Wiener deconvolution increases the PSNR of the bicubic interpolation method, but it actually decreases the PSNR of the NEDI method and the methods [33, 42] by 3dB or more. This manifests the deficiency of carrying out interpolation and deconvolution separately in tandem. On all of the test images the NEARU method outperforms the others methods without exception. The average gain of NEARU over the second best method in the group, which is the bicubic method with Wiener deconvolution, is 1.37 dB.

To assess the visual quality of the NEARU method in comparison with others, we display in Fig. 5.3 through Fig. 5.6 the output images of the NEARU, NEDI and bicubic methods on five test images. We include the NEDI method in the visual comparison group because its perceptual quality is among the best of the previously published methods. The images produced by the NEDI method look more blurred than those by the NEARU method for the obvious reason that the former ignores the effect of PSF. Applying Wiener deconvolution to NEDI sharpens the images but also generates severe speckle and ringing artifacts, which makes NEDI followed by deconvolution inferior to NEARU. Similar conclusions can be drawn between the bicubic interpolation method and NEARU. The NEDI method reproduces large scale edges noticeably better than the bicubic method, but its performance deteriorates on edges of high curvature and on small structures. This weakness can be seen by closely inspecting the eye lashes of Lena (Fig. 5.5(c)) and the writings on the hat (Fig. 5.4(c)). The new NEARU method appears to be a clear winner in visual quality, preserving edge geometry well and free of most of the artifacts made by the other methods. The visual quality assessment results also corroborate the objective measure of PSNR in Table I.

Table 5.1: PSNR (dB) of reconstructed HR images by different methods. For the first four methods the results with and without Wiener deconvolution are included.

Image	Bicubic		Method [33]		NEDI [3]		Method [42]		NEARU
	With Wiener	Without Wiener	With Wiener	Without Wiener	With Wiener	Without Wiener	With Wiener	Without Wiener	
Lena	34.40	33.40	29.01	33.11	30.89	33.66	33.08	33.96	**35.74**
Flower	32.25	31.60	25.41	29.68	26.25	29.85	30.39	31.24	**33.51**
Leaves	30.66	30.05	25.55	29.71	27.58	30.05	29.46	30.19	**32.99**
Bush	26.80	26.29	24.21	25.45	22.85	25.33	25.13	25.80	**27.41**
Bike	26.03	25.54	23.95	25.27	23.23	25.37	25.37	25.60	**27.48**
Parrot	35.87	35.52	32.53	34.83	32.70	35.34	34.43	35.24	**37.20**
Fruit	36.41	35.98	29.89	35.00	31.94	35.33	34.80	35.92	**38.23**
Hat	30.74	30.38	28.73	30.51	29.14	30.59	30.13	30.55	**31.92**
Flight	30.34	29.94	28.27	30.05	28.62	30.00	29.85	30.14	**31.62**
Pepper	33.80	33.55	28.76	33.11	31.12	33.31	33.01	33.69	**34.87**
Average	31.73	31.23	27.63	30.67	28.43	30.88	30.57	31.23	**33.10**

An advantage of the proposed NEARU method is its ability to upconvert an image by an arbitrary scaling factor α. In contrast, with exception of the bicubic interpolation method, the other previously published methods were designed to interpolate images only for scaling factor of power of 2. Therefore, we only compare the NEARU method with the bicubic method for scaling factors that are not power of 2. Fig. 5.7 and Fig. 5.8 show the interpolated Bike and Hat images by scaling factor of 1.8 and 3.2 respectively. The HR images produced by the NEARU method are visually far more pleasant than those by the bicubic method followed by Wiener deconvolution, having cleaner and sharper edges.

We also evaluate the visual quality of different methods for large scaling factors, $\alpha \geq 3$. There are applications that demand large scaling factors, such as reproduction of digital images on magazine cover pages in prepress and on large posters in advertisement. Fig. 5.9 shows a part of LR Bike image and its four times magnifications by the five methods. In this case, the method [33], the NEDI method and the method [42] are applied twice to perform image resolution upconversion by a factor of four. As demonstrated by Figs. 5.8 and 5.9, the improvement of the NEARU method over other methods in perceptual quality becomes even more convincing as scaling factor α increases. We call readers' attention to the capability of NEARU to faithfully reproduce high curvature edges (e.g., fonts) and large structures alike, free of artifacts plaguing the other methods.

In the experiments on arbitrary scaling factors, the test images are directly used as input LR images for the five methods. Here we do not know the true HR images nor the PSF function $\boldsymbol{h}$, as in proceeding simulations. Instead, we use a Gaussian PSF $\boldsymbol{h}$ to associate the input LR with the output HR images in (5.4). In our simulations the standard deviation σ of the Gaussian PSF is made proportional to scaling factor α, $\sigma = c\alpha$, $c \in [0.25, 0.5]$. The ratio $c = \sigma/\alpha$ governs the extent of the overlap of PSF kernels of two adjacent LR pixels. The results shown in Fig. 5.7, Fig. 5.8 and Fig. 5.9 correspond to $c = 0.33$. In practice, one can adjust the parameter c to control the

sharpness of the reconstructed HR image. Given the scaling factor α, a PSF of larger σ (i.e., larger c) will lead to a sharper HR image. Fig. 5.10 illustrates what happens to the reconstructed HR image when one changes the value of c.

5.6 Conclusion

A technique of model-based nonlinear estimation for adaptive resolution upconversion is proposed in this chapter. The image is modeled by two separate piecewise autoregressive models. The model parameters and the unknown HR pixels are jointly estimated for an image block. The problem is formulated as a nonlinear least square optimization problem and a structure total least square based solution is given. The proposed NEARU technique combines the adaptive upsampling and deconvolution into one pass and can resize the LR image by an arbitrary scaling factor. The new technique outperforms the existing techniques in both PSNR measure and subjective visual quality over a wide range of scenes, and is particularly suitable for large-scale resolution upconversion.

(a) Original Image

(b) NEARU

(c) NEDI [3]

(d) NEDI with Wiener deconvolution

Figure 5.3: Comparison of different methods on Bush image (to be continued).

(e) Bicubic

(f) Bicubic with Wiener deconvolution

Figure 5.3: Comparison of different methods on Bush image (Cont'd.).

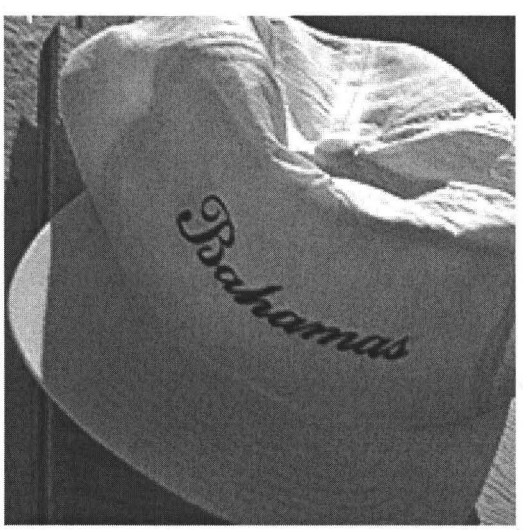

(a) Original Image

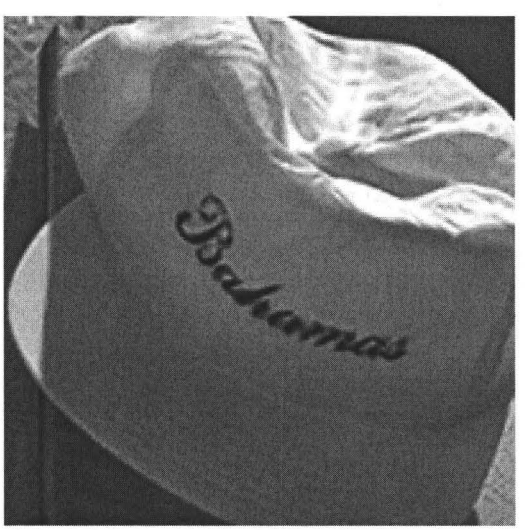

(b) NEARU

Figure 5.4: Comparison of different methods on Hat image (to be continued).

(c) NEDI [3]

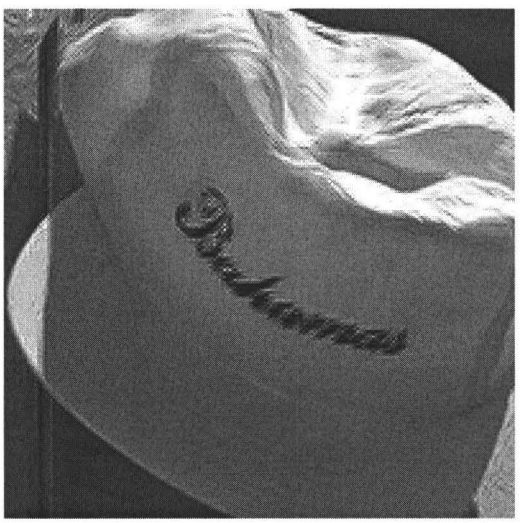

(d) NEDI with Wiener deconvolution

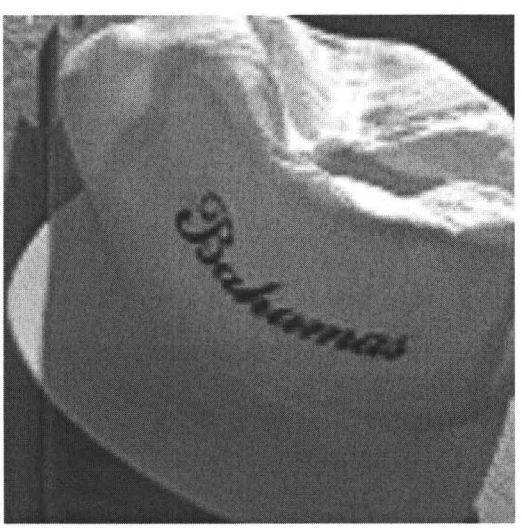

(e) Bicubic

(f) Bicubic with Wiener deconvolution

Figure 5.4: Comparison of different methods on Hat image (Cont'd.).

(a) Original Image

(b) NEARU

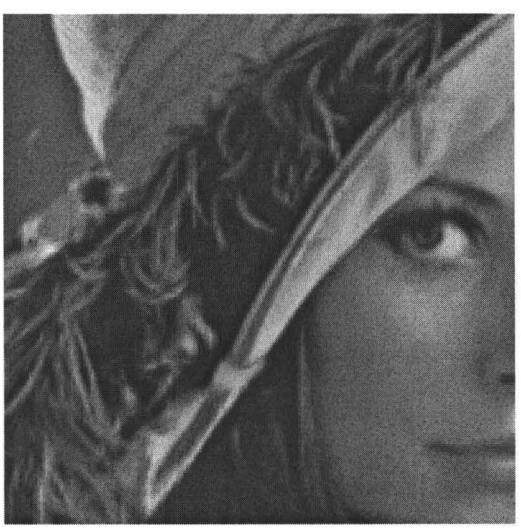

(c) NEDI [3]

(d) NEDI with Wiener deconvolution

Figure 5.5: Comparison of different methods on Lena image (to be continued).

(e) Bicubic

(f) Bicubic with Wiener deconvolution

Figure 5.5: Comparison of different methods on Lena image (Cont'd.).

(a) Original Image

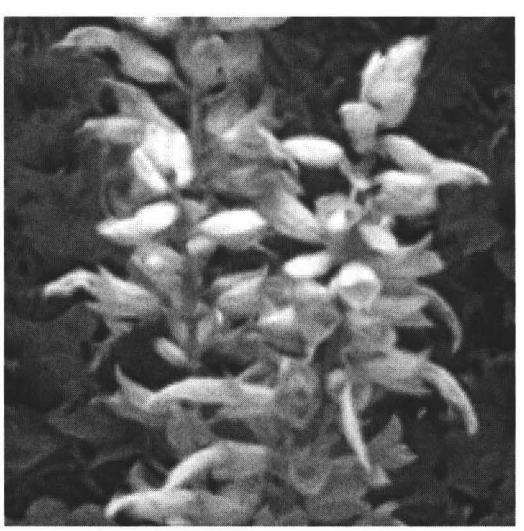

(b) NEARU

Figure 5.6: Comparison of different methods on Flower image (to be continued).

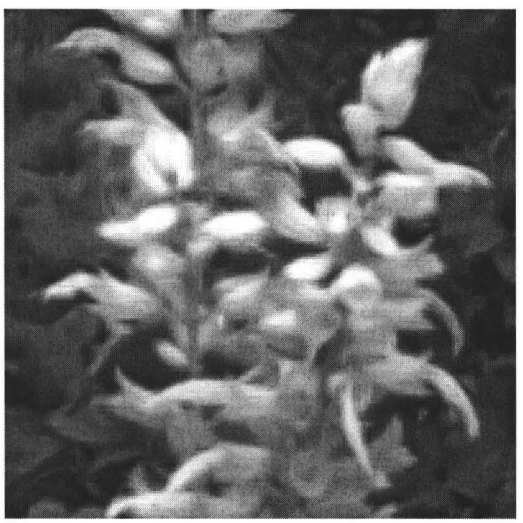

(c) NEDI [3]

(d) NEDI with Wiener deconvolution

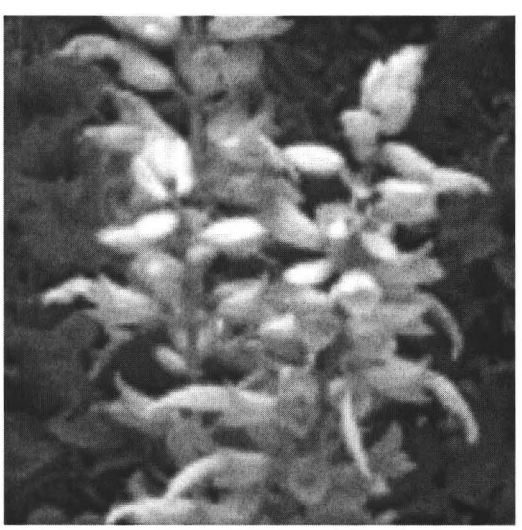

(e) Bicubic

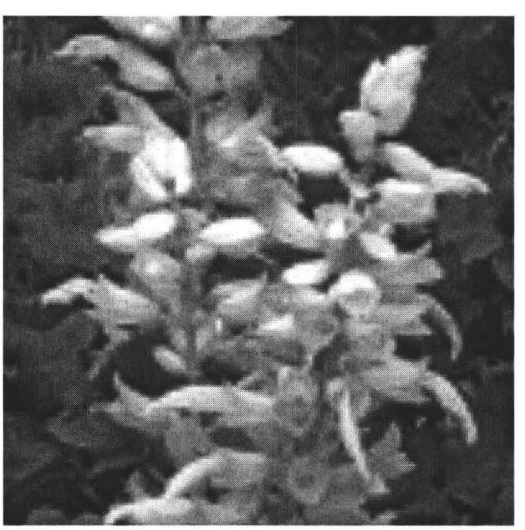

(f) Bicubic with Wiener deconvolution

Figure 5.6: Comparison of different methods on Flower image (Cont'd.).

(a) Bicubic with Wiener deconvolution

Figure 5.7: Interpolated Bike image with scaling factor $\alpha = 1.8$ (to be continued).

(b) NEARU

Figure 5.7: Interpolated Bike image with scaling factor $\alpha = 1.8$ (Cont'd.).

(a) Bicubic with Wiener deconvolution

Figure 5.8: Interpolated Hat image with scaling factor $\alpha = 3.2$ (to be continued).

(b) NEARU

Figure 5.8: Interpolated Hat image with scaling factor $\alpha = 3.2$ (Cont'd.).

(a) LR Image

(b) Bicubic with Wiener deconvolution

(c) Method [33] with Wiener deconvolution

(d) Method [42] with Wiener deconvolution

Figure 5.9: Comparison of different methods on Bike image with scaling factor $\alpha = 4.0$ (to be continued).

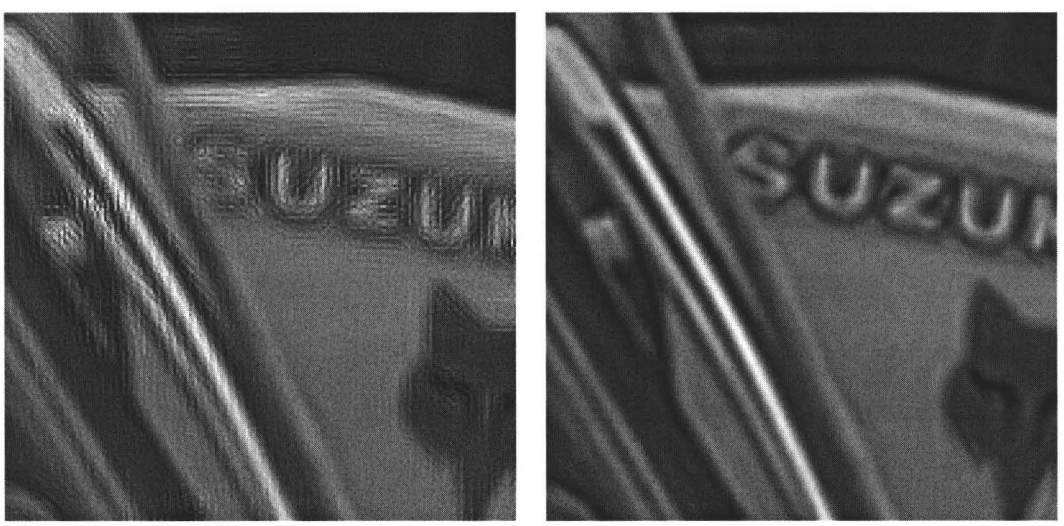

(e) NEDI with Wiener deconvolution (f) NEARU

Figure 5.9: Comparison of different methods on Bike image with scaling factor $\alpha = 4.0$ (Cont'd.).

(a) $c = 0.4$

(b) $c = 0.5$

(c) $c = 0.67$

Figure 5.10: Effects of changing c in $\sigma = c\alpha$, the standard deviation of a Gaussian PSF, here $\alpha = 1.5$.

Chapter 6

Compression by Collaborative Adaptive Down-sampling and Upconversion

In the remainder of this thesis our attention is turned to the use of image interpolation as a tool for low bit-rate image compression. In this chapter we study interpolation-based image compression of single description, and extend this work to multiple descriptions in the next chapter.

6.1 Overview

Over the past half century the prevailing engineering practice of image/video compression, as exemplified by all existing image and video compression standards, is to start with a dense 2D sample grid of pixels. Compression is done by transforming the spatial image signal into a space (e.g., spaces of Fourier or wavelet bases) in which the image has a sparse representation and by entropy coding of transform coefficients. Recently, researchers in the emerging field of compressive sensing challenged the wisdom of what they called "oversampling followed massive dumping" approach. They

showed, quite surprisingly, it is possible, at least theoretically, to obtain compact signal representation by a greatly reduced number of random samples [78].

In this chapter, we seek for compact image representation in an approach of sparse sampling in the spatial domain. The fact that most natural images have an exponentially decaying power spectrum suggests the possibility of interpolation-based compact representation of images. A typical scene contains predominantly smooth regions that can be satisfactorily interpolated from a sparsely sampled low-resolution image. The difficulty is with the reconstruction of high frequency contents. Of particular importance is faithful reconstruction of edges without large phase errors, which is detrimental to perceptual quality of a decoded image.

To answer the above challenge, we develop a new image compression methodology of collaborative adaptive down-sampling and upconversion. The CADU approach puts an emphasis on edge reconstruction for the perceptual importance of edges and also to exploit the anisotropy of edge spectrum. In the CADU encoder design we choose not to perform uneven irregular down sampling of an input image according to local spatial or frequency characteristics. Instead, we stick to conventional square pixel grid by uniform spatial down sampling of the image. Consequently, the resulting LR image can be readily compressed by any of existing image compression techniques, such as DCT-based JPEG and JPEG 2000. Yet the simple uniform down-sampling scheme is made adaptive by a directional low-pass prefiltering step prior to down-sampling. The other purpose of this preprocessing is to induce a mechanism of collaboration between the spatial uniform down-sampling process at the encoder and optimal upconversion process at the decoder.

The CADU decoder first decompresses the LR image and then upconverts it to the original resolution in constrained least squares restoration process, using a 2D PAR model, which is similar to the interpolation method described in previous chapter. Two-dimensional autoregressive modeling was a known effective technique of predictive image coding [72, 79]. For the CADU decoder, the PAR model plays a role

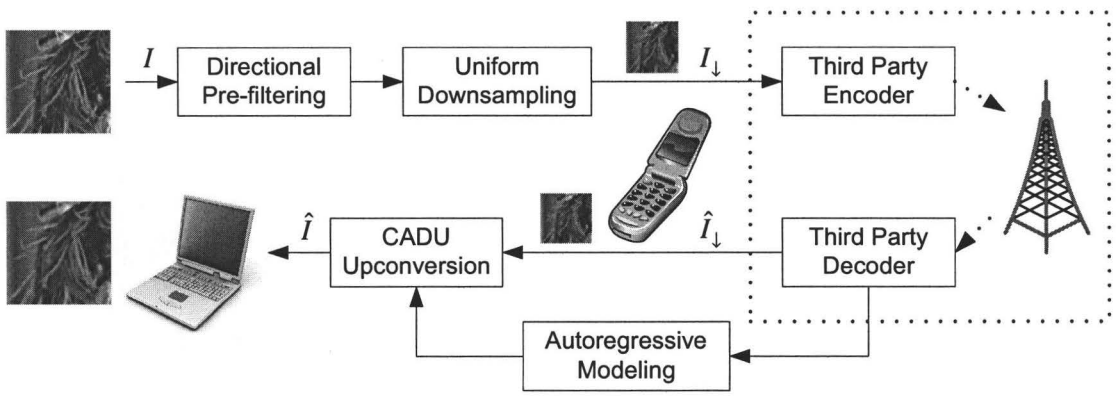

Figure 6.1: Block diagram of the proposed CADU image compression system.

of adaptive non-causal predictor. What is novel and unique of the CADU approach is that the predictor is only used at the decoder side, and the non-causal predictive decoding is performed in collaboration with the prefiltering of the encoder.

Fig. 6.1 presents a block diagram of the proposed CADU image compression system, summarizing the above ideas and depicting the collaboration between the encoder and decoder.

The CADU image compression technique, although operating on down-sampled images, obtains some of the best PSNR results and visual quality at low to medium bit rates. CADU outperforms the JPEG 2000 standard, even though the latter is fed images of higher resolution and is widely regarded as an excellent low bit-rate image codec [80].

Since the down-sampled image has the conventional form of square pixel grid and can be fed directly to any existing image codec, standard or proprietary, the CADU upconversion process is entirely up to the decoder. Thus, as shown in Fig. 6.1, the proposed CADU image coding approach can work in tandem with any third party image/video compression techniques. This flexibility makes standard compliance a non-issue for the new CADU method. We envision that CADU becomes a useful enhancer of any existing image compression standard for improved low bit-rate performance.

An important application of CADU is visual communication in wireless networks, where the bandwidth is at a premium and end devices have diverse display capabilities, ranging from small screens of cell phones to regular screens of laptops. As illustrated in Fig. 6.1, the same standard-compliant code stream $\hat{I}_{\downarrow}$ feeds displays of different resolutions. The only difference is that high-resolution displays invoke CADU upconversion while low-resolution displays do not. This design happens to be compatible with network hardware levels since high-resolution displays are typically associated with more powerful computers. In such a heterogenous wireless environment scalable or layered image compression methods (e.g., JPEG 2000) are inefficient, because the refinement portion of the scalable code stream still consumes bandwidth and yet generates no benefits to low-resolution devices.

Because the down-sampled image is only a small fraction of the original size, CADU greatly reduces the encoder complexity, regardless what third-party codec is used in conjunction. This property allows the system to shift the computation burden from the encoder to decoder, making CADU a viable asymmetric compression solution when the encoder is resource deprived. Furthermore, the superior low bit-rate performance of the CADU approach seems to suggest that a camera of unnecessarily high resolution can ironically produce inferior images than a lower resolution camera, if given a tight bit budget. This rather counter-intuitive observation should be heeded when one designs visual communication devices/systems with severe constraints of energy and bandwidth.

The related previous works were reviewed in Section 2.3 of Chapter 2. Those works were largely motivated by the susceptibility of DCT-based block codecs to severe artifacts at low bit rates. However, in our view, for applications of very tight bit budget, one should adopt wavelet-based codecs, such as JPEG 2000, which are well known for their clear superiority over DCT-based codecs in both subjective and objective quality at low bit rates. Now the question is whether it is also advantageous to downsample an image prior to wavelet-based compression at low bit rates. This

chapter will answer this question affirmatively. In fact, according to our experimental results, the CADU technique coupled with JPEG 2000 consistently has higher PSNR than all existing techniques for bit rates below 0.3 bpp, and it achieves better visual quality than others for bit rates up to 0.5 bpp.

The chapter is organized as follows. Section 6.2 describes the CADU encoder of uniform down-sampling with adaptive direction prefiltering. Section 6.3 presents the restoration process in decoder: a constrained least squares upconversion algorithm driven by a PAR image model. We report and discuss the experimental results in Section 6.4.

6.2 Uniform Down-Sampling with Adaptive Directional Prefiltering

Out of practical considerations, we make a more compact representation of an image by decimating every other row and every other column of the image. This simple approach has an operational advantage that the down-sampled image remains a uniform rectilinear grid of pixels, and can readily be compressed by any of existing international image coding standards. To prevent the down-sampling process from causing aliasing artifacts, it seems necessary to low-pass pre-filter an input image to half of its maximum frequency f_{max}. However, on a second reflection, one can do somewhat better. In areas of edges, the 2D spectrum of the local image signal is not isotropic. Thus we seek to perform adaptive sampling, within the uniform down-sampling framework, by judiciously smoothing the image with directional low-pass prefiltering prior to down-sampling.

To this end, we design a family of 2D directional low-pass prefilters under the criterion of preserving the maximum 2D bandwidth without the risk of aliasing. Let $w_L(\theta)$ and $w_H(\theta)$ be the side lengths of the rectangular low-passed region of the 2D filter in the low- and high-frequency directions of an edge of angle θ, respectively.

The maximum area of this low-passed region without aliasing is $A = w_L(\theta)w_H(\theta) = \pi^2$. It is easy to show that there are only eight values of θ (corresponding to three combinations of $w_L(\theta)$ and $w_H(\theta)$ values) to achieve $w_L(\theta)w_H(\theta) = \pi^2$ while avoiding aliasing. These eight cases are tabulated in Table 6.1. Fig. 6.2 illustrates the above directional low-pass filter design for $\theta = 0, \tan^{-1}\frac{1}{2}, \frac{\pi}{4}$ (the low-passed frequency range for other angles can be obtained by rotation). The spectra in the diagrams are those of the straight line of angle θ.

Table 6.1: The design of directional low-pass 2D pre-filters

θ	$0\ ;\ \frac{\pi}{2}$	$\pm\tan^{-1}\frac{1}{2}\ ;\ \pm\tan^{-1}2$	$\pm\frac{\pi}{4}$
$w_L(\theta)$	π	$\pi/\sqrt{5}$	$\pi/\sqrt{2}$
$w_H(\theta)$	π	$\sqrt{5}\pi$	$\sqrt{2}\pi$

In addition, the directional low-pass filter design serves two other purposes: 1) Most efficient packing of signal energy in presence of edges; 2) Preservation of subjective image quality for the edge is an important semantic construct. Moreover, as we will see in the next section, the use of low-pass prefilters establishes sample relations that play a central role in the decoding process of constrained least squares upconversion.

Many implementations of directional low-pass prefilters are possible. For instance, the following directional low-pass prefilter can be used

$$h_\theta(i,j) = m\,\mathrm{sinc}\left(\frac{i\cos\theta + j\sin\theta}{s_i}\right)\mathrm{sinc}\left(\frac{-i\sin\theta + j\cos\theta}{s_j}\right)\Psi(i,j) \tag{6.1}$$

where m is the normalization factor to keep the filter in unit energy, and $\Psi(i,j)$ is a window function (such as the *sinc* window function). The parameters s_i and s_j are:

$$s_i = \frac{w_H(\theta)}{2\pi}, \quad s_j = \frac{w_L(\theta)}{2\pi} \tag{6.2}$$

In the directional prefiltering step, the CADU encoder first computes the gradient at the sampled position. If the amplitude of the gradient is below a threshold, the

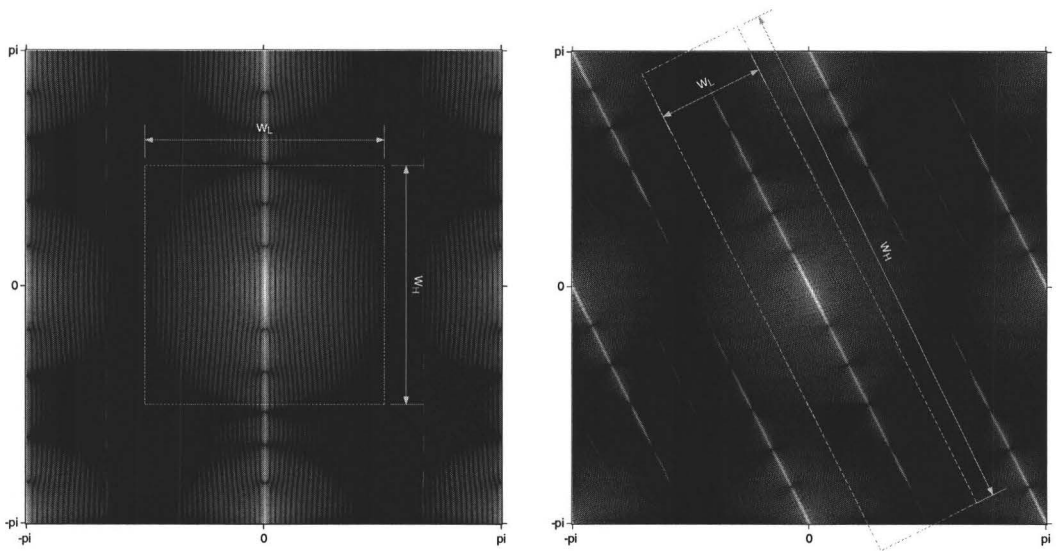

(a) $\theta = 0$ (b) $\theta = \tan^{-1}\frac{1}{2}$

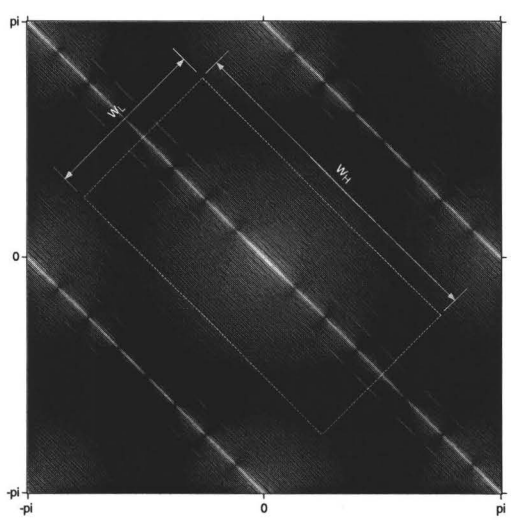

(c) $\theta = \frac{\pi}{4}$

Figure 6.2: Directional filters of maximum passed region $w_L(\theta)w_H(\theta) = \pi^2$.

isotropic low-pass filter $\boldsymbol{h}_0$ is applied. Otherwise, the gradient direction is quantized and the corresponding filter $\boldsymbol{h}_\theta$ in Table 6.1 is selected and applied.

Despite its simplicity, the CADU compression approach via uniform down-sampling is not inherently inferior to other image compression techniques in rate-distortion performance, as long as the target bit rate is below a threshold. The argument is based on the classical water-filling principle in rate-distortion theory. To encode a set of K independent Gaussian random variables $\{X_1, X_2, \cdots, X_K\}$, $X_k \sim N(0, \sigma_k)$, the rate-distortion bounds, when the total bit rate being $R = \sum_{k=1}^{K} R_k$ and the total mean-squares distortion being $D = \sum_{k=1}^{K} D_k$, are given by

$$\begin{cases} R(D) = \displaystyle\sum_{k=1}^{K} \max\left\{0, \frac{1}{2}\log_2 \frac{\sigma_k^2}{\tau}\right\} \\ D(R) = \displaystyle\sum_{k=1}^{K} \min\{\tau, \sigma_k^2\} \end{cases} \tag{6.3}$$

Most natural images have a rapidly (e.g., exponentially) decaying power spectrum $\Phi(\omega)$. Suppose that the input image is i.i.d. in the Fourier domain and its power spectrum is monotonically decreasing. Therefore, given a target rate r^*, if the rate-distortion function of the image signal satisfies

$$D(r^*) > \int_{\pi/2}^{\pi} \Phi(\omega) d\omega, \tag{6.4}$$

then uniform down-sampling by the factor of two will not limit the rate-distortion performance in information theoretical sense. Indeed, our experimental results (see Section 6.4) demonstrate that the CADU approach outperforms the state-of-the-art JPEG 2000 standard in the low to medium bit rate range.

6.3 Constrained Least Squares Upconversion with Autoregressive Modeling

In this section we develop the decoder of the CADU image compression system. Let $I_\downarrow$ be the decompressed $\frac{M}{2} \times \frac{N}{2}$ subsampled image, and I be the original $M \times N$ image.

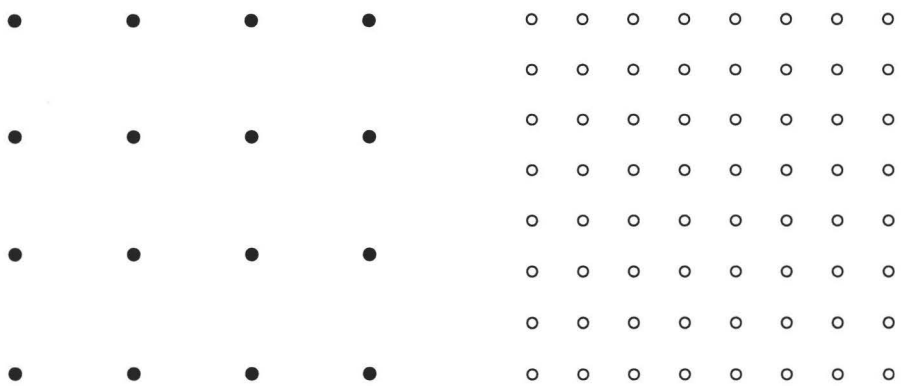

(a) Downsampled prefiltered image (b) Original image

Figure 6.3: The relationship between the down-sampled pre-filtered image and the original image. The illustrated kernel size of the filter is 3x3. A low-resolution pixel (black dots in (a)) is the filtered value of the corresponding 9 original pixels (white dots in (b)).

The sample relation between I and $I_{\downarrow}$ is illustrated by Fig. 6.3. The decoder needs to upconvert $I_{\downarrow}$ to the original resolution of I, which is the same problem as stated in the previous chapter for scaling factor of 2. Therefore, we apply the interpolation method described in the previous chapter to this upconversion problem. For convenience, we re-state the following notations of the previous chapter. $\boldsymbol{x}$ denotes the pixels of the original image I. $\boldsymbol{y}$ stands for the decoded pixels in the down-sampled pre-filtered image $I_{\downarrow}$. $\mathbf{s}_{\times}(i,j)$ and $\mathbf{s}_{+}(i,j)$ are two vectors of four 8-connected neighbors and 4-connected neighbors of $x(i,j)$, respectively. Now, the upconversion problem can be formulated as follows:

$$\begin{aligned} &\min_{\boldsymbol{x},\boldsymbol{\chi},\boldsymbol{\tau}} \Big\{ \sum_{(i,j)\in W} (x(i,j) - \boldsymbol{\chi}^T \mathbf{s}_{\times}(i,j))^2 + \sum_{(i,j)\in W} (x(i,j) - \boldsymbol{\tau}^T \mathbf{s}_{+}(i,j))^2 \Big\} \\ &\text{subject to} \qquad \|\boldsymbol{x} * \boldsymbol{h} - \boldsymbol{y}\|^2 = \|\boldsymbol{\eta}_W(r)\|^2 \quad \text{for } \boldsymbol{x} \in W \end{aligned} \tag{6.5}$$

where $\boldsymbol{\chi} = (\chi_1, \chi_2, \chi_3, \chi_4)$ and $\boldsymbol{\tau} = (\tau_1, \tau_2, \tau_3, \tau_4)$ are parameters of the two PAR models $\mathcal{AR}_{\times}$ and $\mathcal{AR}_{+}$, respectively. Comparing with (5.4), we introduce a term $\boldsymbol{\eta}_W(r)$ in (6.5) to stand for quantization errors incurred on lossy compressed $\boldsymbol{y}$ in local window W. Clearly, the compression noise $\boldsymbol{\eta}_W(r)$ is a function of rate r.

The two PAR models in (6.5) characterize the axial and diagonal correlations respectively, as depicted in Fig. 6.4. These two models act, in a predictive coding perspective, as non-causal adaptive predictors. This gives rise to an interesting interpretation of the CADU decoder: adaptive non-causal predictive decoding constrained by the prefiltering operation of the encoder.

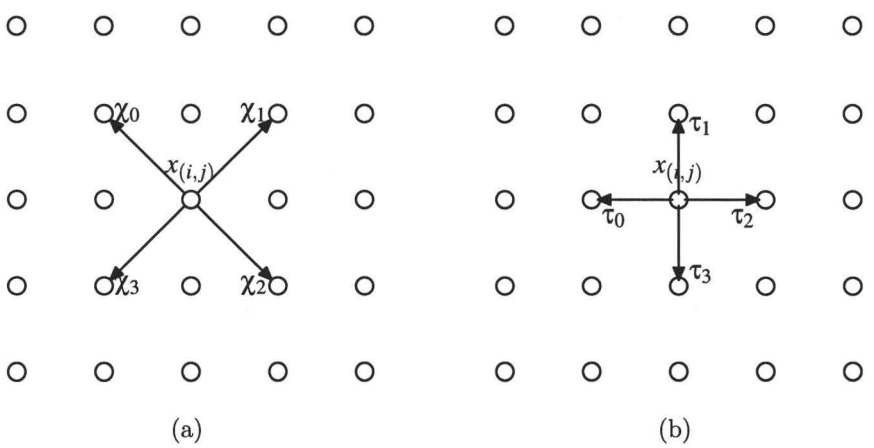

Figure 6.4: Sample relationships with PAR model parameters: (a) $\boldsymbol{\chi} = (\chi_1, \chi_2, \chi_3, \chi_4)$, (b) $\boldsymbol{\tau} = (\tau_1, \tau_2, \tau_3, \tau_4)$.

Similar to (5.6), by applying a Lagrange multiplier λ, (6.5) can be converted to the following unconstrained least square problem

$$\min_{\boldsymbol{x},\boldsymbol{\chi},\boldsymbol{\tau}} \Big\{ \sum_{(i,j)\in W} (x(i,j) - \boldsymbol{\chi}^T \mathbf{s}_\times(i,j))^2 + \sum_{(i,j)\in W} (x(i,j) - \boldsymbol{\tau}^T \mathbf{s}_+(i,j))^2 + \lambda ||\boldsymbol{y} - \boldsymbol{x} * \boldsymbol{h}||^2 \Big\} \quad (6.6)$$

Since $\boldsymbol{y}$ is lossy compressed, the value of λ should be chosen according to the bit rate r. The quantization noise $\boldsymbol{\eta}_W(r)$ is a decreasing function in the bit rate r. As r increases, the decoder weighs the constraint $\|\boldsymbol{x} * \boldsymbol{h} - \boldsymbol{y}\|^2 = \|\boldsymbol{\eta}_W(r)\|^2$ more by increasing the value of λ.

For each pixel $y_i \in I_\downarrow$, $\boldsymbol{h}_\theta$ is adaptively chosen from the pool of prefilters listed in Table 6.1: $\boldsymbol{h}_0$ for smooth waveform and others for different quantized edge directions, as described in the proceeding section. The decoder needs to know the chosen $\boldsymbol{h}_\theta$ for optimal reconstruction, and it can determine the adaptive directional filter used at

the encoder by applying the same gradient operator as the encoder to the decoded image $I_{\downarrow}$. This achieves the synchronization of the encoder and decoder with high probability without sending any side information.

The CADU system design is asymmetric: the encoder is a simple and inexpensive process, while the decoder involves solving a rather large-scale optimization problem described in (6.6).

6.4 Experimental Results and Discussions

The proposed image coding method was implemented and evaluated in both PSNR and subjective quality. We compared the CADU method with the adaptive downsampling-based image codec proposed by Lin and Dong [67]. The latter was reportedly the best among all previously published downsampling-interpolation image codecs [63, 64] in both objective and subjective quality. Note that all existing image codecs of this type were developed for DCT-based image compression, whereas the CADU method is applicable to wavelet-based codecs as well. Therefore, we also include in our comparative study JPEG 2000, the quincunx coding method [81], and the method of uniform down-sampling at the encoder and bicubic interpolation at the decoder. The bicubic method in the comparison group and the CADU method used the same simple encoder: JPEG 2000 coding of uniformly down-sampled prefiltered image. The difference is in the upconversion process: the former method performed bicubic image interpolation followed by a deconvolution step using Weiner filter to reverse the prefiltering, instead of solving a constrained least squares image restoration problem driven by autoregressive models as described in the proceeding section.

Although the proposed CADU method favors the reconstruction of edges, we chose, for fairness and generality of our comparative study, a large set of test images of various scene compositions. Here we report experimental results for four representative images, which represent all common image features in balance: edges of all

scales, smooth regions, and granular textures, as one can see in Fig. 6.5.

Table 6.2 lists the PSNR results of seven methods: DCT-based old JPEG standard (column JPEG), the method of Lin and Dong [67] (the 2nd column), the CADU method coupled with DCT-based JPEG (column CADU-JPG) JPEG 2000 (column J2K), JPEG 2000 coupled with uniform downsampling and bicubic interpolation (column Bicubic), the quincunx method [81] (column Quincunx), and the CADU method coupled with JPEG 2000 (column CADU-J2K). The results are tabulated against various bit rates from 0.1 bpp to 0.3 bpp. For the first two methods of the group, some table entries at very low bit rates are "N/A" because the DCT-based JPEG cannot even operate at such low rates for the image tested.

The PSNR comparison between Lin-Dong's method and the CADU-JPG method is somewhat mixed. CADU-JPG has a small advantage over Lin-Dong's method in most cases, but the former lost to the latter by small margin for test images Flower and Bike when the rate is equal to and greater than 0.25 bpp. Although these two methods outperform old JPEG without downsampling, but they both produced significantly lower PSNR than wavelet-based JPEG 2000 without downsampling. Obviously, one should use JPEG 2000 when the bit budget is low in practice. For the state of the art in low bit rate image compression, the reader should pay closer attention to the results of the wavelet group in Table 6.2. At low rates, the CADU-J2K method achieves up to 0.5 dB higher PSNR than JPEG 2000. This improvement is quite remarkable given that JPEG 2000 is highly regarded for its outstanding performance at low rates [2]. Among the four competing methods in the wavelet group, the bicubic interpolation method has the lowest PSNR in most cases. Given that the CADU-J2K and bicubic interpolation methods use the same prefilters and the same JPEG 2000 encoder, the performance gap between the two manifests the efficacy of least squares non-causal predictive decoding constrained by adaptive directional low-pass prefiltering.

The quincunx coding method also outperforms JPEG 2000 at low to modest bit rates, but it requires a much more expensive, non-standard encoder.

Table 6.2: The PSNR (dB) results for different compression methods.

Image	Rate (bpp)	Methods						
		DCT-based			Wavelet-based			
		JPEG	Method [67]	CADU-JPG	J2K	Bicubic	Quincunx	CADU-J2K
Lena	0.10	N/A	N/A	27.69	30.19	30.13	30.29	30.42
	0.15	25.57	28.77	29.48	31.85	31.82	32.02	32.19
	0.20	28.77	30.67	30.72	33.21	32.88	33.28	33.35
	0.25	30.58	31.63	31.66	34.27	33.43	34.23	33.98
	0.30	31.81	32.39	32.48	35.02	33.82	34.91	34.46
Leaves	0.10	N/A	N/A	23.83	25.67	25.69	25.71	26.05
	0.15	N/A	N/A	25.61	27.51	27.26	27.91	28.02
	0.20	24.14	26.33	26.78	28.99	28.29	29.33	29.43
	0.25	26.64	27.62	27.87	30.16	28.92	30.75	30.45
	0.30	27.86	28.58	28.73	31.35	29.42	32.01	31.22
Flower	0.10	N/A	N/A	22.42	24.16	24.10	23.99	24.25
	0.15	N/A	N/A	24.24	25.67	25.72	25.62	25.92
	0.20	22.08	25.13	25.47	26.98	26.71	26.88	27.09
	0.25	24.84	26.40	26.43	27.98	27.78	27.87	28.04
	0.30	26.01	27.27	27.08	28.78	28.65	28.72	28.84
Bike	0.10	N/A	N/A	20.20	21.38	21.34	21.30	21.55
	0.15	N/A	N/A	21.25	22.42	22.37	22.30	22.63
	0.20	20.74	21.83	21.97	23.28	23.25	23.29	23.61
	0.25	21.84	22.73	22.53	24.08	23.81	24.09	24.18
	0.30	22.66	23.46	23.03	24.68	24.33	24.77	24.90

Next let us assess the subjective quality of the methods evaluated. Fig. 6.5 presents the decoded images by different methods at bit rate 0.2 bpp. First, we notice that the wavelet-based methods have superior visual quality to the DCT-based methods, which is consistent with the PSNR comparison results in Table 6.2. In the wavelet group, the CADU-J2K method produces the visually most pleasing images. At low bit rates both JPEG 2000 and the bicubic interpolation method produce objectionable visual artifacts (e.g., jaggies and ringings) in edge areas, whereas the CADU-J2K method is largely free of those defects. Even when the bit rate gets higher and JPEG

2000 starts to have higher PSNR than the CADU-J2K method, its visual quality still appears inferior, as demonstrated by examples in Fig. 6.6. The superior visual quality of the CADU-J2K method is due to the good fit of the piecewise autoregressive model to edge structures and the fact that the human visual system is highly sensitive to phase errors in reconstructed edges. We believe that the CADU-J2K image coding approach of down-sampling with directional prefiltering at the encoder and edge-preserving upconversion at the decoder offers an effective and practical solution for subjective image coding.

Some viewers may find that JPEG 2000 produces somewhat sharper edges compared with CADU-J2K, although at the expense of introducing more and worse artifacts. However, one can easily tip the quality balance in visual characteristics to favor CADU-J2K by performing an edge enhancement of the results of CADU-J2K. Fig. 6.7 presents some sample results of JPEG 2000 and CADU-J2K at the bit rate of 0.2 bpp after edge enhancement. For better judgement these images should be compared with their counterparts in Fig. 6.5. As expected, the high-pass operation of edge enhancement magnifies the structured noises accompanying edges in images of JPEG 2000. In contrast, edge enhancement sharpens the images of CADU-J2K without introducing objectionable artifacts, which further improves the visual quality.

The CADU-J2K decoder has much higher complexity than the decoder based on bicubic interpolation. A close inspection of the reconstructed images by the CADU-J2K decoder and the bicubic method reveals that the two methods visually differ only in areas of edges. Therefore, an effective way of expediting the CADU-J2K decoder is to invoke least squares non-causal predictive decoding, which is the computation bottleneck of CADU, only in regions of high activity, and resort to fast bicubic interpolation in smooth regions. If a decoder is severely constrained by computational resources, it can perform bicubic interpolation everywhere in lieu of the CADU restoration process. Such a resource scalability of the decoder is desired in application scenarios when decoders of diverse capabilities are to work with the same

code stream.

(a) JPEG (b) Method [67]

(c) CADU-JPG (d) J2K

Figure 6.5: Comparison of different methods at 0.2bpp (to be continued).

6.5 Conclusions

We proposed a new, standard-compliant approach of coding uniformly down-sampled images while still outperforming JPEG 2000 in both PSNR and visual quality at low

to modest bit rates. This success is due to the novel upconversion process of least square non-causal predictive decoding constrained by adaptive directional low-pass prefiltering. Our findings suggest that a lower sampling rate can actually produce higher quality images at certain bit rates.

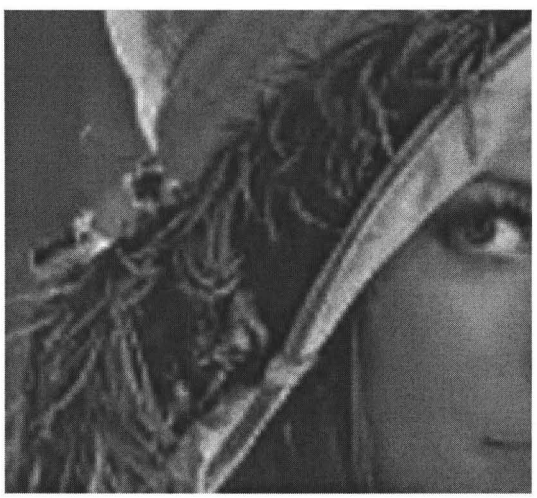

(e) Bicubic-J2K

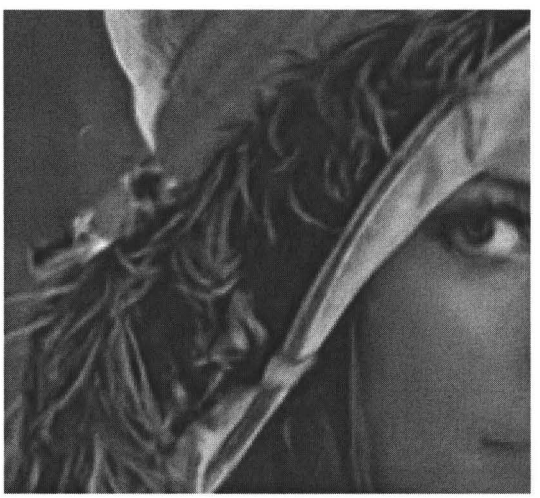

(f) CADU-J2K

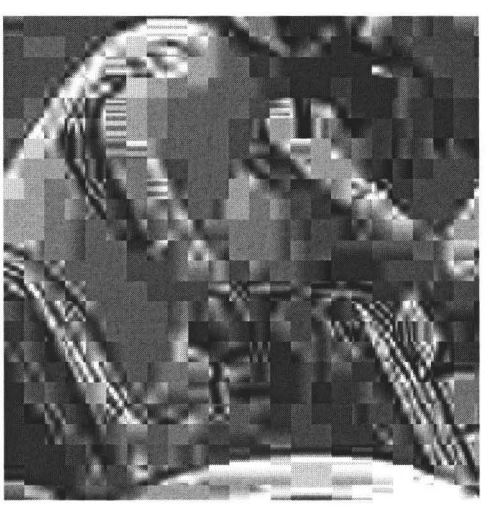

(g) JPEG

(h) Method [67]

Figure 6.5: Comparison of different methods at 0.2bpp (to be continued).

(i) CADU-JPG

(j) J2K

(k) Bicubic

(l) CADU-J2K

Figure 6.5: Comparison of different methods at 0.2bpp (to be continued).

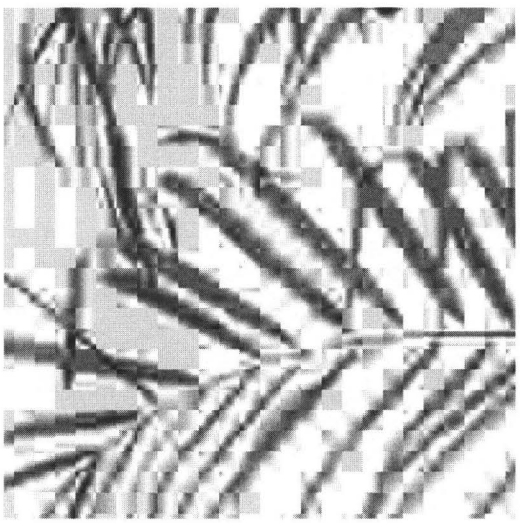

(m) JPEG

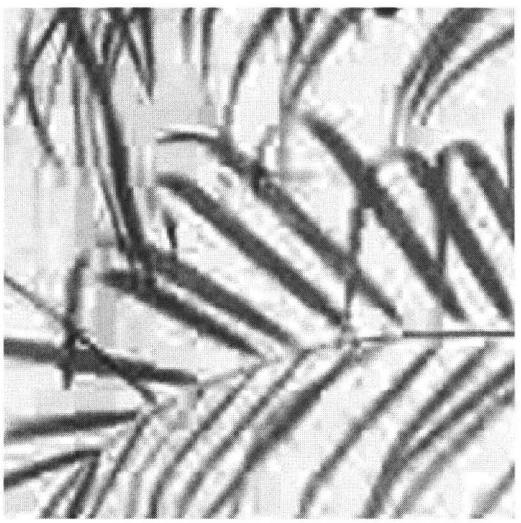

(n) Method [67]

(o) CADU-JPG

(p) J2K

Figure 6.5: Comparison of different methods at 0.2bpp (to be continued).

(q) Bicubic

(r) CADU-J2K

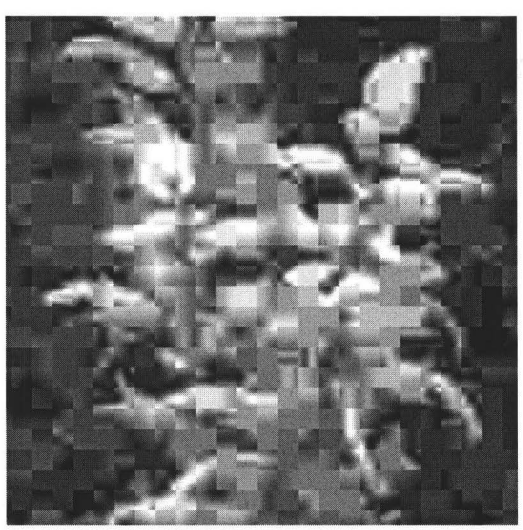

(s) JPEG

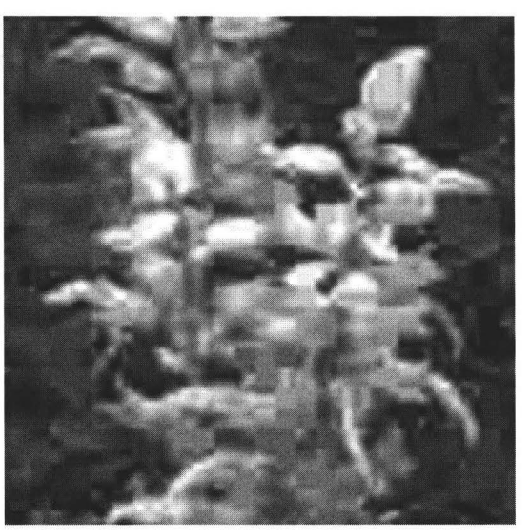

(t) Method [67]

Figure 6.5: Comparison of different methods at 0.2bpp (to be continued).

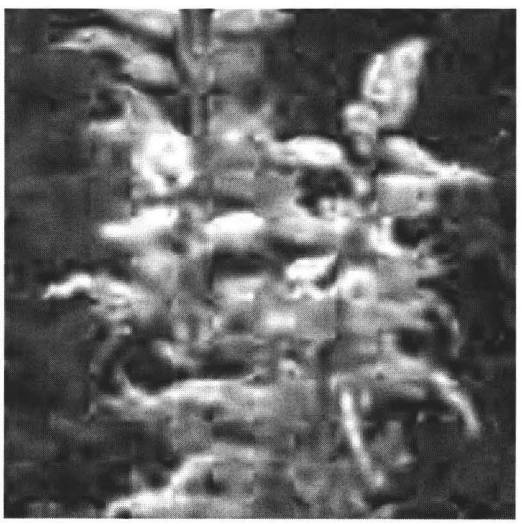

(u) CADU-JPG

(v) J2K

(w) Bicubic

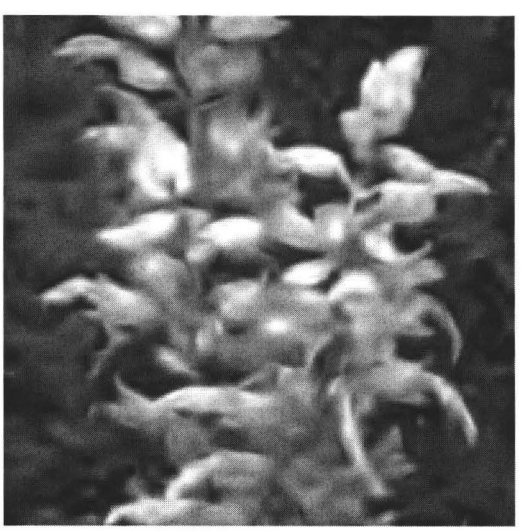

(x) CADU-J2K

Figure 6.5: Comparison of different methods at 0.2bpp (Cont'd.).

(a) J2K (0.3bpp, 35.02 dB)

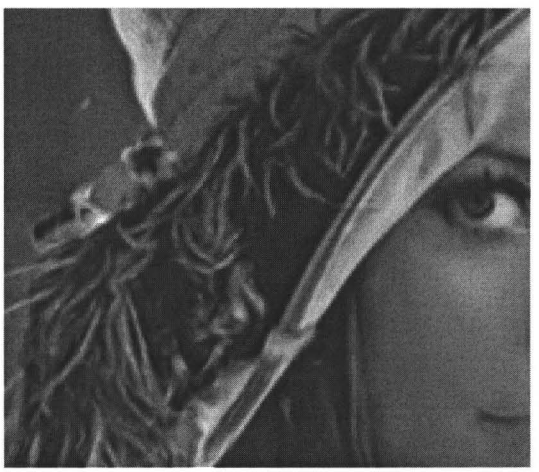

(b) CADU-J2K (0.3bpp, 34.46 dB)

(c) J2K (0.35bpp, 32.32 dB)

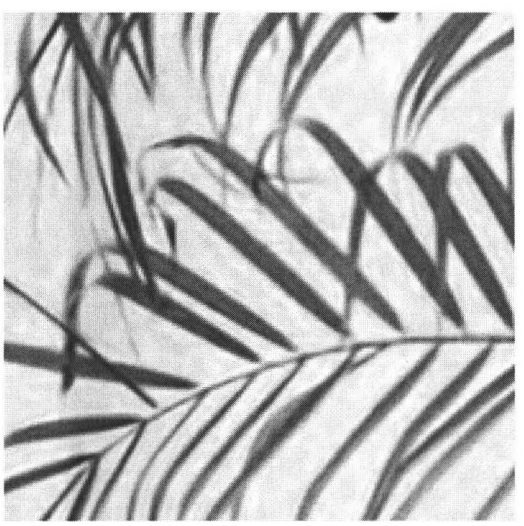

(d) CADU-J2K (0.35bpp, 31.36 dB)

Figure 6.6: Comparison of different methods. Note the superior visual quality of the CADU method even though it has a lower PSNR (to be continued).

(e) J2K (0.45bpp, 26.45 dB) (f) CADU-J2K (0.45bpp, 26.02 dB)

Figure 6.6: Comparison of different methods. Note the superior visual quality of the CADU method even though it has a lower PSNR (Cont'd.).

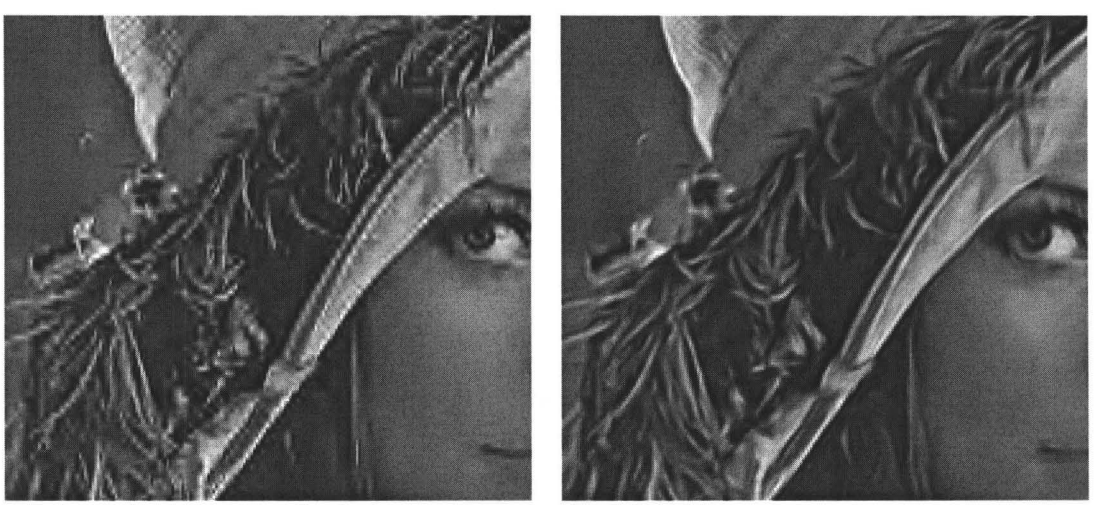

(a) J2K (b) CADU-J2K

Figure 6.7: Edge-enhanced versions of the output images of JPEG 2000 and CADU at 0.2bpp. These images are to be compared with their counterparts in Fig. 6.5 (to be continued).

(c) J2K

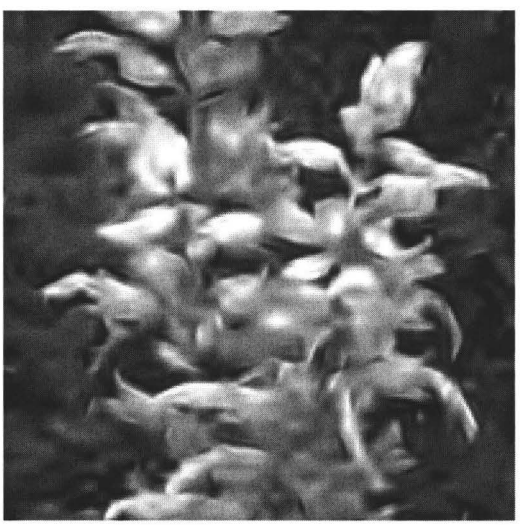

(d) CADU-J2K

(e) J2K

(f) CADU-J2K

Figure 6.7: Edge-enhanced versions of the output images of JPEG 2000 and CADUat 0.2bpp. These images are to be compared with their counterparts in Fig. 6.5 (Cont'd.).

Chapter 7

Spatial Multiplexing Multiple Description Coding

In this chapter, we extend our study on interpolation-based image compression from conventional single description coding to multiple description coding , and propose a practical standard-compliant image MDC technique. Multiple descriptions of an image are generated in the spatial domain by an adaptive prefiltering and uniform down sampling process, similar to the CADU approach described in the previous chapter. The resulting side descriptions are conventional square sample grids that are interleaved with one the other. As such each side description can be coded by any of the existing image compression standards. The side decoder is same as the decoder in CADU approach. The central decoder is algorithmically similar to the side decoder, but it improves the reconstruction quality by using received side descriptions as additional constraints when solving the underlying inverse problem.

7.1 Overview

One of the landmarks of modern digital multimedia technology is ubiquitous visual communications over lossy public networks (e.g., the Internet). The needs for

network-aware coding techniques to mitigate the problem of packet losses have generated much interest in MDC of images and videos. But all existing image MDC techniques [82, 83, 84, 85] are not compliant to existing image compression standards, either being completely different approaches or requiring a significant degree of modifications to an existing standard.

Because all image compression standards, such as DCT-based JPEG and wavelet-based JPEG 2000, require the input image to be a rectangular grid of pixels, the only standard-compliant approach of image MDC is to generate side descriptions by uniform down-sampling in the image space, as illustrated in Fig. 1.4. The question is whether the spatial multiplexing scheme of Fig. 1.4 can be made a practical and competitive solution for multiple description (MD) compression of images. In this chapter we will give an affirmative answer to the above question.

Our new MDC technique, called spatial multiplexing multiple description, is schematically described in Fig. 7.1. An input image is prefiltered with an adaptive directional low-pass filter described in Section 6.2. In SMMD scheme, this preprocessing serves dual purposes: 1) introduction of correlations between side descriptions, and 2) better energy packing of image signal. The filtered image is then split by a simple multiplexer into $K \geq 2$ SMMD side descriptions, each of which is a down-sampled subimage of square lattice. Any third party image compression method, standard or proprietary, can be used to compress the K subimages, generating K side description code streams. These SMMD K descriptions are transmitted from a source node to a destination node via diversity links in an erasure network. The SMMD side decoder is exactly same as the decoder in CADU approach. Specifically, it decompresses the received subimage and subsequently solves an inverse problem of restoring the original image using the correlation between subimages introduced by the prefiltering and a two-dimensional PAR model. The SMMD central decoder performs a joint demultiplexing-restoration of multiple interleaved decompressed subimages. Algorithmically, the SMMD central decoder is very similar to the SMMD side de-

coder, but it improves the restoration quality by using received multiple subimages (side descriptions) as additional regularization constraints when solving the ill-posed inverse problem.

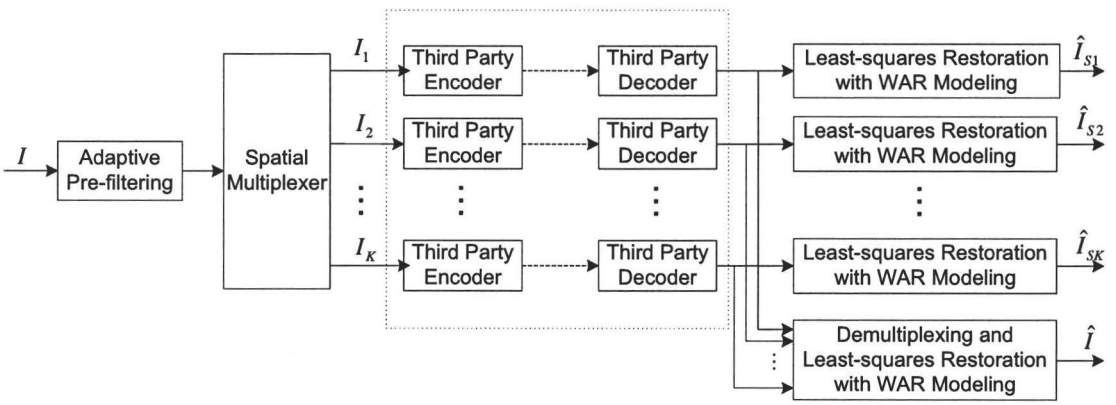

Figure 7.1: SMMD Framework.

As clearly illustrated by Fig. 7.1, the SMMD encoder and decoder are independent of the third party conventional single-description image compression method used, thus they are compatible with any image compression standard.

Since the prefiltering process and the side decoder are same as that in CADU method, we focus on describing the central decoder in the following section, and then report and discuss the experimental results in Section 7.3. Section 7.4 concludes.

7.2 SMMD Central Decoder

For the clarity of presentation and without loss of generality, we discuss the SMMD central decoder for the case of two descriptions (see Fig. 7.2). The following development and results can be easily generalized to any number of descriptions.

The block diagram of the SMMD central decoder is shown in Fig. 7.2. Upon receiving both descriptions, the central decoder demultiplexes the two decompressed subimages (side descriptions) $\hat{I}_1$ and $\hat{I}_2$, and reconstructs a quincunx subimage $\hat{I}_Q$.

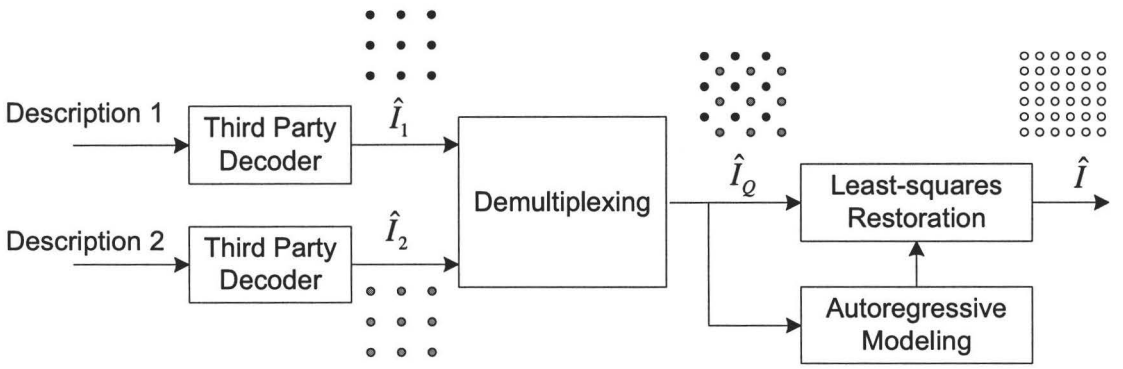

Figure 7.2: Block diagram of the SMMD central decoder.

Then the original image I is reconstructed from $\hat{I}_Q$ by a similar inverse filtering technique as the side decoder.

The subimage $\hat{I}_Q$ can be formed by directly merging the two decoded descriptions $\hat{I}_1$ and $\hat{I}_2$. However, since the two subimages $\hat{I}_1$ and $\hat{I}_2$ are spatially interleaved, one can also be estimated from the other by interpolation. Suppose that a pixel y_i in $\hat{I}_Q$ corresponds to a sample $\hat{y}_i^{(k)}$ in side description $\hat{I}_k$, $k = 1, 2$. We can interpolate y_i from the other description and obtain another estimate $\hat{y}_i^*$. We fuse $\hat{y}_i^{(k)}$ and $\hat{y}_i^*$ to make a more robust estimate of y_i:

$$y_i = w\hat{y}_i^{(k)} + (1 - w)\hat{y}_i^* \tag{7.1}$$

where w is a context-based weight. The context consists of three features:

$$\begin{aligned} d_i &= |\hat{y}_i^{(k)} - \hat{y}_i^*| \\ c_i &= (\hat{y}_i^{(k)} + \hat{y}_i^*)/2 \\ \mu_i &= \frac{1}{2|W|} \sum_{i \in W} (\hat{y}_i^{(k)} + \hat{y}_i^*). \end{aligned} \tag{7.2}$$

We quantize the context into four classes, and select the weight w based on the

classification:

$$w = \begin{cases} w_1 & \text{if} \quad d_i <= 2 \\ w_2 & \text{if} \quad 2 < d_i <= T \ \cap \ |\mu_i - c_i| <= d_i/2 \\ w_3 & \text{if} \quad 2 < d_i <= T \ \cap \ |\mu_i - c_i| > d_i/2 \\ w_4 & \text{if} \quad d_i > T \end{cases} \tag{7.3}$$

The threshold T and the four weights w_1 through w_4 in (7.3) are optimized using a training set.

As in the proceeding chapter, denote by $\boldsymbol{y}$ the pixels in the quincunx image $\hat{I}_Q$ and $\boldsymbol{x}$ the pixels in the original image I. Then the problem formulation for SMMD central decoding is the same as (6.5). But there are important differences between the SMMD central and side decoding when it comes to solving (6.5) and estimating model parameters. Firstly, the term $\|\boldsymbol{x} * \boldsymbol{h} - \boldsymbol{y}\|^2 = \|\boldsymbol{\eta}_W(r)\|^2$ in (6.5) now has twice as many constraints as in the case of side decoding. This is because the SMMD central decoder works with the quincunx subimage $\hat{I}_Q$ instead of $\hat{I}_1$ or $\hat{I}_2$. Since these constraints are imposed by directional prefiltering, the availability of more constraints improves the estimate made by the inverse filtering of (6.5) that is an ill-posed problem to begin with. Secondly, the estimates of the PAR model parameters are also improved by the availability of both side descriptions $\hat{I}_1$ and $\hat{I}_2$. Fig. 7.3 shows the spatial configuration between y_i and its neighbors for the SMMD central decoder, in which the relationship between y_i and its neighbor $y^{\times}_{i \diamond t}$ in $\hat{I}_Q$ has the same space scale as that between x_i and its neighbors $x^{\times}_{i \diamond t}$ in I. Therefore, the the model parameters $\boldsymbol{\chi}$ can be better estimated for the central decoder than for the side decoder. The above are the reasons for the reduction of distortion from the side decoder to the central decoder.

7.3 Experimental Results and Discussions

Experiments were carried out on natural images to evaluate the proposed SMMD technique in comparison with two recently published multiple description image cod-

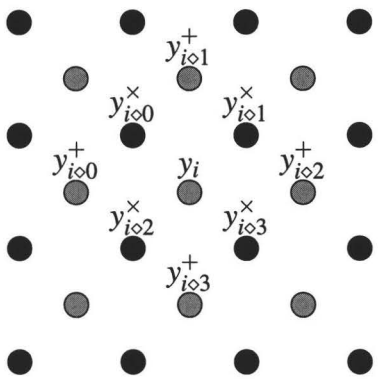

Figure 7.3: The relationship between low-resolution pixel y_i with its neighbors in $\hat{I}_Q$.

ing techniques [84] and [85]. The latter two techniques produced some of the best MDC image coding results so far. The reported SMMD results are for two symmetric side descriptions as described in the proceeding sections. Each resulting side description is encoded by the JPEG 2000 standard.

Fig. 7.4 plots the side PSNR and central PSNR of the different MDC techniques versus the central bit rate (bpp) for four test images. For all the test images, both the side and central descriptions of the SMMD technique achieve higher PSNR than the other two MDC techniques at low to modest bit rates. For the same performance of the central decoder, the SMMD side decoder can outperform the other two side decoders by more than 1dB in PSNR at low bit rates. However, at high rates, the currently implemented SMMD system performed worse than the other two methods in PSNR. This performance can be improved by different spatial multiplexing schemes. The study on this line is underway.

With its emphasis on edge reconstruction, the SMMD technique appears to produce superior visual quality than its competitors in both side and central descriptions. This is the case even when the SMMD technique has a lower PSNR than the others. To verify this please refer to Fig. 7.5 through Fig. 7.7 in which some decoded images by the three MDC techniques are compared. Common compression artifacts at low bit rates, such as jaggies along edges, are greatly reduced by the SMMD technique.

When losing one description, the SMMD side decoder still preserves edges well and reconstructs the original image with good visual quality. This can be seen by comparing Fig. 7.5(e) with Fig. 7.5(f), and Fig. 7.6(e) with Fig. 7.6(f). However, a side description is insufficient to reproduce very high frequency components due to the spatial downsampling. In this case, the visual quality of the reconstructed image can be improved significantly by the central decoder when both descriptions are available. Fig. 7.8 presents three such examples. The high frequency clothes stripes, and the details such as eyelashes and spokes are reconstructed much better by the central decoder than the side decoder.

7.4 Conclusion

A spatial multiplexing multiple description scheme for image MDC is proposed in this chapter. Multiple descriptions are generated by uniformly downsampling in image space with adaptive prefiltering. Side decoder reconstructs the input image by solving an inverse problem with 2D piecewise autoregressive modeling. Central decoder demultiplexes the multiple descriptions first, and then reconstructs the input image in a way similar to side decoder, but improves the reconstruction quality with additional constraints.

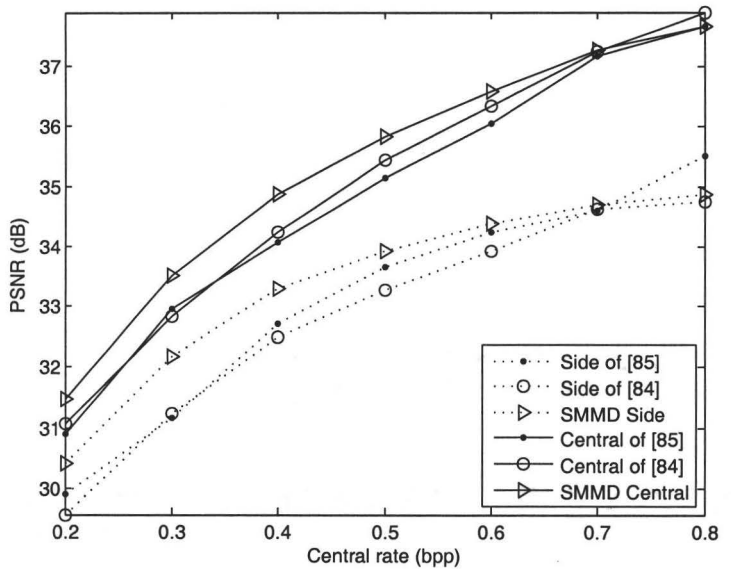

(a) Lena

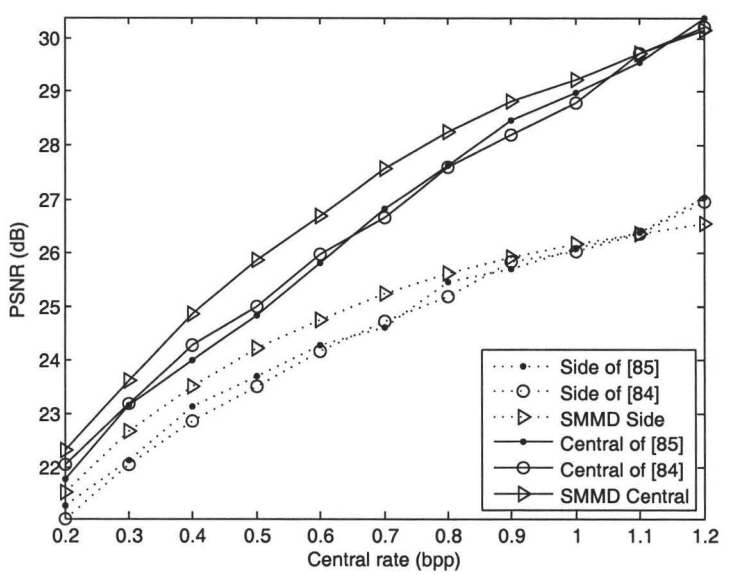

(b) Bike

Figure 7.4: Comparison of different methods in both side and central PSNR (dB) versus the central rate (bpp) (to be continued).

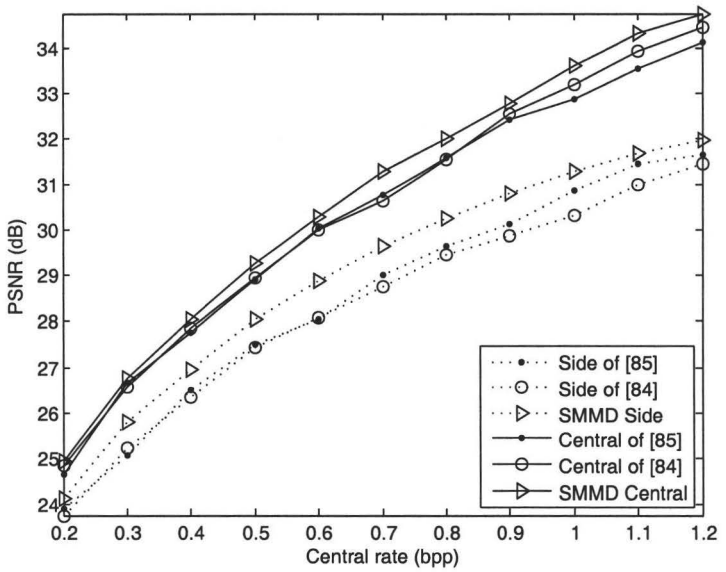

(c) Flower

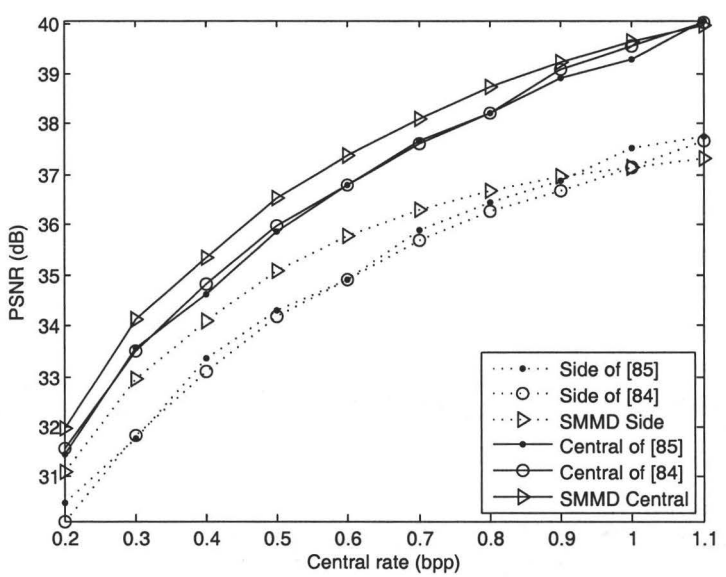

(d) Fruit

Figure 7.4: Comparison of different methods in both side and central PSNR (dB) versus the central rate (bpp) (Cont'd.).

(a) Side description of [84]

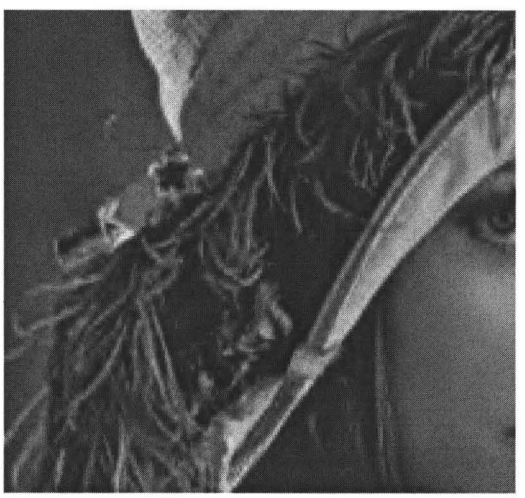

(b) Central description of [84]

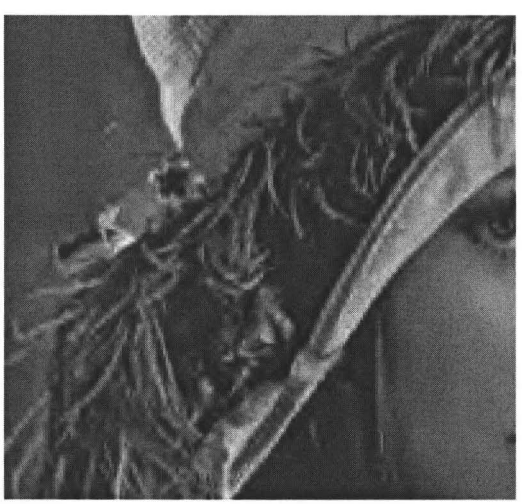

(c) Side description of [85]

(d) Central description of [85]

Figure 7.5: Comparison of decoded Lena images at 0.25 bpp/description (to be continued).

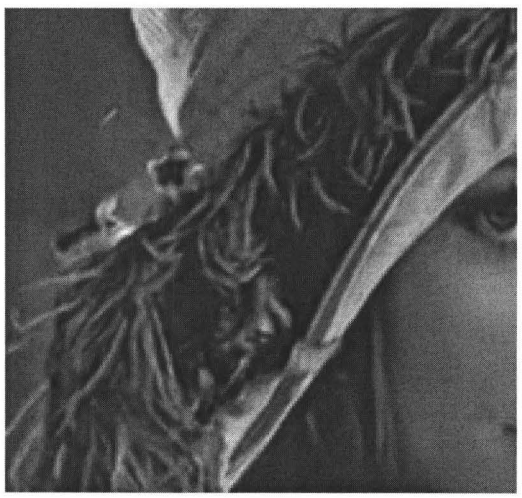

(e) SMMD side description

(f) SMMD central description

Figure 7.5: Comparison of decoded Lena images at 0.25 bpp/description (Cont'd.).

(a) Side description of [84]

(b) Central description of [84]

Figure 7.6: Comparison of decoded Fruit images at 0.4 bpp/description (to be continued).

(c) Side description of [85]

(d) Central description of [85]

(e) SMMD side description

(f) SMMD central description

Figure 7.6: Comparison of decoded Fruit images at 0.4 bpp/description (Cont'd.).

(a) Side Description of [85] (PSNR: 26.87dB)

(b) Side Description of [84] (PSNR: 26.79dB)

(c) SMMD Side Description(PSNR:26.59dB)

Figure 7.7: Comparison of decoded Bike images at 0.6 bpp/description. Note that the SMMD side decoder produces superior visual quality even though it has lower PSNR than the other two MDC techniques.

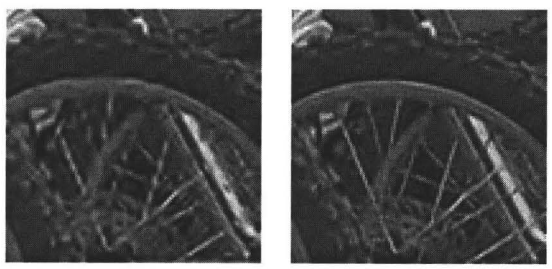

(a) Side (b) Central

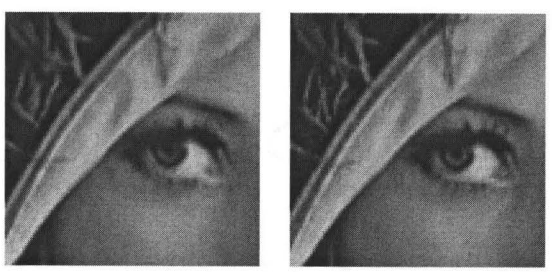

(c) Side (d) Central

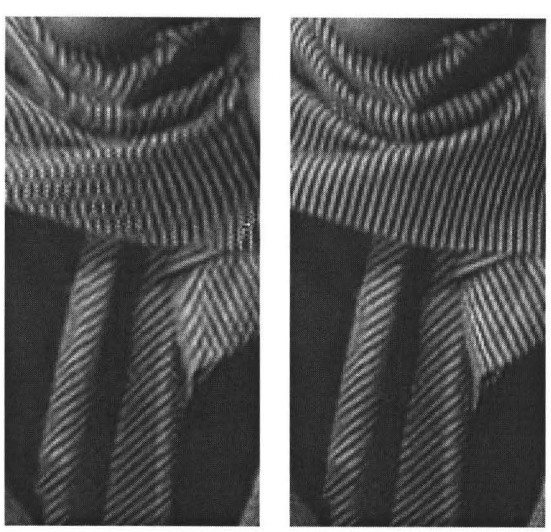

(e) Side (f) Central

Figure 7.8: Comparison of the performance of SMMD central decoder and side decoder.

Chapter 8

Conclusions and Future Work

8.1 Conclusions

The research of this thesis advances the state-of-the-art of image interpolation technology and significantly improves the accuracy and visual quality of existing methods. Three new image interpolation methods are proposed: the first one is a classification approach that chooses an interpolation direction based on texture orientation; the second method is a soft-decision approach that estimates missing pixels in blocks rather than individually to ensure spatial coherence of the reconstructed image; the third method takes a new model-based nonlinear image restoration approach in which the model parameters and the unknown HR pixels are jointly estimated. These new methods have been implemented and thoroughly evaluated in comparison with those published in the literature. Extensive experiments have been conducted and the results convincingly demonstrate the advantages of the proposed methods over their predecessors.

In addition, we study and explore the use of image interpolation as a technique for image compression, in particular for two important scenarios: low bit-rate visual communication and network-aware multiple description coding. The study results in two novel standard-compliant interpolation-based compression methods, one for low

to medium bit rates and the other for multiple descriptions. They generate some of the best rate-distortion performance reported in the literature in their respective categories.

Although most of our results are satisfying and among the best so far in the fields, they can still, we believe, be improved and extended to other topics of image/video processing. The piecewise autoregressive image model plays a central role in the development of the SAI and NEARU methods. But the estimation of model parameters in an LR image is prone to the problem of data overfitting. Currently, we circumvent the problem by using two separate models of lower order and weighing them. But a more principled solution should be a unified model whose order is determined in minimize description length principle. Any progress in this regard will further improve the interpolation performance in the future. Another possibility is to choose from a pool of one-dimensional models of higher order. This may allow us to fully exploit the anisotropic property of the image signal and interpolate in the direction of highest statistical redundancy.

Discerning readers may have found our technique of NEARU is a general model-based image restoration framework. With some modifications this framework can be applied to other image restoration problems, such as video superresolution, denoising, deconvolution, deblurring, color demosaicking, and reconstruction of compressive sensing. This line of research is underway.

Bibliography

[1] X. Wu and N. Memon, "Context-based adaptive lossless image coding," *IEEE Transactions on Communications*, vol. 45, no. 4, pp. 437–444, April 1997.

[2] D. Tabuman and M. Marcellin, *JPEG2000: Image compression fundamentals, standards and parctice.* Kluwer Academic Publishers, 2002.

[3] X. Li and M. T. Orchard, "New edge-directed interpolation," *IEEE Transactions on Image Processing*, vol. 10, pp. 1521–1527, October 2001.

[4] B. Meyer and P. Tischer, "TMW – a new method for lossless image compression," in *Proceedings of 1997 Picture Coding Symposium*, Berlin, Germany, October 1997.

[5] H. Stark and P. Oskoui, "High-resolution image recovery from image-plane arrays using convex projections," *J. Opt. Soc. Am. A*, vol. 6, no. 11, pp. 1715–1726, Nov. 1989.

[6] A. V. Oppenheim, A. S. Willsky, and S. H. Nawab, *Signals & Systems*, 2nd ed. Prentice Hall, 1997.

[7] R. G. Keys, "Cubic convolution interpolation for digital image processing," *IEEE Transactions on Acoustic, Speech and Signal Processing*, vol. ASSP-29, no. 6, pp. 1153–1160, December 1981.

[8] X. Zhang and X. Wu, "Image interpolation by adaptive 2-D autoregressive modeling and soft-decision estimation," *IEEE Transactions on Image Processing*, vol. 17, no. 6, pp. 887–896, June 2008.

[9] X. Wu and X. Zhang, "Image interpolation using texture orientation map and kernel Fisher discriminant," in *Proc. IEEE Int. Conf. Image Processing*, vol. 1, 2005, pp. I–49–52.

[10] X. Zhang and X. Wu, "Structure preserving image interpolation via adaptive 2D autoregressive modeling," in *Proc. IEEE Int. Conf. Image Processing*, vol. 4, 2007, pp. IV–193 – IV–196.

[11] X. Wu, X. Zhang, and X. Wang, "Model-based non-linear estimation for adaptive resolution upconversion and deconvolution," *IEEE Trans. on Image Processing*, (under review).

[12] X. Zhang and X. Wu, "Can lower resolution be better?" in *Proc. IEEE Data Compression Conf.*, 2008, pp. 302–311.

[13] X. Wu, X. Zhang, and X. Wang, "Image compression via adaptive down-sampling and constrained least squares upconversion," *IEEE Trans. on Image Processing*, (to appear).

[14] X. Zhang and X. Wu, "Standard-compliant multiple description image coding by spatial multiplexing and constrained least-squares restoration," in *Proc. IEEE Int. Workshop on Multimedia Signal Processing (MMSP)*, 2008.

[15] E. Meijering, "A chronology of interpolation: from ancient astronomy to modern signal and image processing," in *Proceedings Of The IEEE*, vol. 90, March 2002, pp. 319–342.

[16] R. C. Gonzalez and R. E. Woods, *Digital Image Processing*, 2nd ed. Prentice Hall, 2002.

[17] S. K. Park and R. A. Schowengerdt, "Image reconstruction by parametric cubic convolution," *Comput. Vis., Graphics, Image Procesing*, vol. 23, no. 3, pp. 258–272, 1983.

[18] R. A. Gabel, "Equiripple two-dimensional interpolation filters," in *IEEE Int. Conf. Acoustics, Speech, and Signal Processing (ICASSP)*, vol. 8, 1983, pp. 387–390.

[19] S. E. Reichenbach and F. Geng, "Two-dimensional cubic convolution," *IEEE Trans. Image Processing*, vol. 12, no. 8, pp. 857–865, Aug. 2003.

[20] J. Shi and S. E. Reichenbach, "Image interpolation by two-dimensional parametric cubic convolution," *IEEE Tran. Image Processing*, vol. 15, no. 7, pp. 1857–1870, July 2006.

[21] H. S. Hou and H. C. Andrews, "Cubic splines for image interpolation and digital filtering," *IEEE Transactions on Acoustic, Speech and Signal Processing*, vol. 26, no. 6, pp. 508–517, December 1978.

[22] E. Maeland, "On the comparison of interpolation methods," *IEEE Trans. Medical Imaging*, vol. 7, pp. 213–217, 1988.

[23] M. Unser, A. Aldroubi, and M. Eden, "Enlargement or reduction of digital images with minimum loss of information," *IEEE Tran. Image Processing*, vol. 4, no. 3, pp. 247–258, Mar. 1995.

[24] M. Unser, "Splines: a perfect fit for signal and image processing," *IEEE Signal Processing Magazine*, pp. 22–38, Nov. 1999.

[25] B. Vrcelj and P. P. Vaidyanathan, "Efficient implementation of all-digital interpolation," *IEEE Tran. Image Processing*, vol. 10, no. 11, pp. 1639–1646, Nov. 2001.

[26] C. G. T. M. Lehmann and K. Spizter, "Survey: interpolation methods in medical image processing," *IEEE Transactinos on Medical Imaging*, vol. 18, pp. 1049–1075, November 1999.

[27] T. M. Lehmann, C. Gönner, and K. Spitzer, "Addendum: B-spline interpolation in medical image processing," *IEEE Trans. Medical Imaging*, vol. 20, no. 7, pp. 660–665, July 2001.

[28] G. Ramponi, "Warped distance for space-variant linear image interpolation," *IEEE Trans. Image Processing*, vol. 8, no. 5, pp. 629–639, May 1999.

[29] J. Han and S. Baek, "Parametric cubic convolution scaler for enlargement and reduction of image," *IEEE Trans. Consumer Electronics*, vol. 46, no. 2, pp. 247–256, May 2000.

[30] H. SHi and R. Ward, "Canny edge based image expansion," in *IEEE Int. Symposium on Circuits and Systems*, vol. 1, 2002, pp. I–785 – I–788.

[31] J. W. Hwang and H. S. Lee, "Adaptive image interpolation based on local gradient features," *IEEE Signal Processing Letters*, vol. 11, no. 3, pp. 359–362, March 2004.

[32] C. Vázquez, E. Dubois, and J. Konrad, "Reconstruction of nonuniformly sampled images in spline spaces," *IEEE Trans. Image Processing*, vol. 14, no. 6, pp. 713–725, June 2005.

[33] K. Jensen and D. Anastassiou, "Subpixel edge localization and the interpolation of still images," *IEEE Transactions on Image Processing*, vol. 4, pp. 285–295, March 1995.

[34] J. Allebach and P. W. Wong, "Edge-directed interpolation," in *Proc. IEEE Int. Conf. Image Processing*, vol. 3, 1996, pp. 707–710.

[35] S. Dube and L. Hong, "An adaptive algorithm for image resolution enhancement," in *Singals, Systems and Computers*, vol. 2, 2000, pp. 1731–1734.

[36] S. Carrato and L. Tenze, "A high quality 2x image interpolator," *IEEE Signal Processing Letters*, vol. 7, pp. 132–135, June 2000.

[37] F. Malgouyres and F. Guichard, "Edge direction preserving image zooming: a mathematical and numerical analysis," *SIAM J. Numer. Anal.*, vol. 39, pp. 1–37, 2001.

[38] Q. Wang and R. Ward, "A new edge-directed image expansion scheme," in *IEEE Int. Conf. Image Processing (ICIP)*, vol. 3, 2001, pp. 899–902.

[39] D. D. Muresan, "Fast edge directed polynomial interpolation," *IEEE Int. Conf. Image Processing (ICIP)*, vol. 2, pp. II–990–3, Nov. 2005.

[40] Q. Wang and R. K. Ward, "A new orientation-adaptive interpolation method," *IEEE Trans. Image Processing*, vol. 16, no. 4, pp. 889–900, Apr. 2007.

[41] D. D. Muresan and T. W. Parks, "Adaptively quadratic (AQua) image interpolation," *IEEE Transactions on Image Processing*, vol. 13, no. 5, pp. 690–698, May 2004.

[42] L. Zhang and X. Wu, "Image interpolation via directional filtering and data fusion," *IEEE Transactions on Image Processing*, vol. 15, no. 8, pp. 2226–2238, August 2006.

[43] Y. Cha and S. Kim, "Edge-forming methods for image zooming," *Journal of Mathematical Imaging and Vision*, vol. 25, no. 3, pp. 353–364, Oct. 2006.

[44] ——, "Edge-forming methods for color image zooming," *IEEE Trans. Image Processing*, vol. 15, no. 8, pp. 2315–2323, Aug. 2006.

[45] M. Li and T. Q. Nguyen, "Markov random field model-based edge-directed image interpolation," *IEEE Trans. Image Processing*, vol. 17, no. 7, pp. 1121–1128, July 2008.

[46] W. K. Carey, D. B. Chuang, and S. S. Hemami, "Regularity-preserving image interpolation," *IEEE Transactions on Image Processing*, vol. 8, no. 9, pp. 1293–1297, September 1999.

[47] Y. Zhu, S. C. Schwartz, and M. T. Orchard, "Wavelet domain image interpolation via statistical estimation," in *Proceedings of International Conference on Image Processing*, vol. 3, September 2001, pp. 840–843.

[48] D. D. Muresan and T. W. Parks, "Prediction of image detail," in *Proceedings of International Conference on Image Processing*, vol. 2, September 2000, pp. 323–326.

[49] S. G. Chang and Z. Cvetković, "Locally adaptive wavelet-based image interpolation," *IEEE Trans. Image Processing*, vol. 15, no. 6, pp. 1471–1485, June 2006.

[50] A. Temizel and T. Vlachos, "Wavelet domain image resolution enhancement," *IEE Proc. Vis. Image Signal Processing*, vol. 153, no. 1, pp. 25–30, Feb. 2006.

[51] A. Tsai, A. Y. Jr., and A. S. Willsky, "Curve evolution implementation of the Mumford-Shah functional for image segmentation, denoising, interpolation, and magnification," *IEEE Trans. Image Processing*, vol. 10, no. 8, pp. 1169–1186, Aug. 2001.

[52] W. T. Freeman, T. R. Jones, and E. C. Pasztor, "Example-based superresolution," *IEEE Comput. Graphics Appl.*, vol. 22, no. 2, pp. 56–65, Mar. 2002.

[53] S. Baker and T. Kanade, "Limits on super-resolution and how to break them," *IEEE Trans. Patttern Analysis and Machine Intelligence*, vol. 24, no. 9, pp. 1167–1183, Sept. 2002.

[54] J. Sun, N. Zheng, and H. S. H. Tao, "Image hallucination with primal sketch priors," in *IEEE Proceedings on Computer Vision and Pattern Recognition*, vol. 2, June 2003, pp. II–7 29–36.

[55] C. Lin, K. Fan, H. Pu, S. Lu, and S. Liang, "An HVS-directed neural-network-based image resolution enhancement scheme for image resizing," *IEEE Trans. Fuzzy Systems*, vol. 15, no. 4, pp. 605–615, Aug. 2007.

[56] R. R. Schultz and R. L. Stevenson, "A bayesian approach to image expansion for improved definition," *IEEE Trans. Image Processing*, vol. 3, no. 3, pp. 233–242, May 1994.

[57] K. Ratakonda and N. Ahuja, "POCS based adaptive image manification," in *Proc. IEEE Int. Conf. Image Processing*, vol. 3, 1998, pp. 203–207.

[58] D. Calle and A. Montanvert, "Superresolution inducing of an image," in *Proc. IEEE Int. Conf. Image Processing*, vol. 3, 1998, pp. 232–235.

[59] F. Fekri, R. M. Mersereau, and R. W. Schafer, "A generalized interpolative vector quantization method for jointly optimal quantization, interpolation, and binarization of text images," *IEEE Trans. Image Processing*, vol. 9, no. 7, pp. 1272–1281, July 2000.

[60] N. A. Woods, N. P. Galatsanos, and A. K. Katsaggelos, "Stochastic methods for joint registration, restoration, and interpolation of multiple undersampled images," *IEEE Trans. Image Processing*, vol. 15, no. 1, pp. 201–213, Jan. 2006.

[61] H. Takeda, S. Farsiu, and P. Milanfer, "Kernel regression for image processing and reconstruction," *IEEE Trans. Image Processing*, vol. 16, no. 2, pp. 349–366, Feb. 2007.

[62] J. Kopf, M. Cohen, D. Lischinski, and M. Uyttendaele, "Joint bilateral upsampling," *ACM Transactions on Graphics (Proceedings of SIGGRAPH)*, vol. 26, no. 3, pp. 96–1 – 96–6, July 2007.

[63] B. Zeng and A. N. Venetsanopoulos, "A JPEG-based interpolative image coding scheme," in *Proc. IEEE ICASSP*, vol. 5, 1993, pp. 393–396.

[64] A. M. Bruckstein, M. Elad, and R. Kimmel, "Down-scaling for better transform compression," *IEEE Trans. Image Processing*, vol. 12, no. 9, pp. 1132–1144, Sept. 2003.

[65] A. S. A, M. E. B, P. M. C, R. W. A, and C. F. A, "Improved high-definition video by encoding at an intermediate resolution," in *Proc. SPIE Visual Communications and Image Processing*, vol. 5308, 2004, pp. 1007–1018.

[66] Y. Tsaig, M. Elad, and P. Milanfar, "Variable projection for near-optimal filtering in low bit-rate block coders," *IEEE Trans. Circuits Syst. Video Technol.*, vol. 15, no. 1, pp. 154–160, Jan. 2005.

[67] W. Lin and D. Li, "Adaptive downsampling to improve image compression at low bit rates," *IEEE Trans. Image Processing*, vol. 15, no. 9, pp. 2513–2521, Sept. 2006.

[68] L. Gan, C. Tu, J. Liang, T. D. Tran, and K.-K. Ma, "Undersampled boundary pre-/post-filters for low bit-rate dct-based coders," *IEEE Trans. Image Processing*, vol. 16, no. 2, pp. 428–441, Feb. 2007.

[69] A. K. Jain and F. Farrokhnia, "Unsupervised texture segmentation using Gabor filters," *Pattern Recognition*, vol. 24, no. 12, pp. 1167–1186, 1991.

[70] M. Xu, X. Wu, and P. Fränti, "Context quantization by kernel Fisher discriminant," *IEEE Tran. Image Processing*, vol. 15, no. 1, pp. 169–177, January 2006.

[71] S. Mika, G. Rätsch, J. Weston, B. Schölkopf, A. J. Smola, , and K. R. Müller, "Invariant feature extraction and classification in kernel spaces," in *Advances in neural information processing systems*, vol. 12. MIT Press, 2000, pp. 526–532.

[72] X. Wu, K. U. Barthel, and W. Zhang, "Piecewise 2D autoregression for predictive image coding." in *Proceedings of the IEEE Int. Conf. on Image Processing*, vol. 3, Chicago, Oct. 1998, pp. 901–904.

[73] A. Said and W. Pearlman, "An image multiresolution representation for lossless and lossy compression," *IEEE Trans. Image Processing*, vol. 5, pp. 1303–1330, September 1996.

[74] I. Matsuda, H. Mori, J. Maeda, and S. Itoh, "Design and evaluation of minimum-rate predictors for lossless image coding," *Trans. IEICE (DII)*, vol. J85-D-II, no. 3, pp. 448–456, March 2002, (in Japanese).

[75] J. More, "The Levenberg-Marquardt algorithm: implementation and theory," *Numerical Analysis*, pp. 105–116, 1977.

[76] G. Golub and V. Pereyra, "Separable nonlinear least squares: the variable projection method and its applications," *Inverse Problems*, vol. 19, no. 2, pp. 1–26, Feb. 2003.

[77] J. Rosen, H. Park, and J. Glick, "Structured total least norm for nonlinear problem," *SIAM J. Matrix Anal. Appl.*, vol. 20, no. 1, pp. 14–30, Jan. 1998.

[78] E. Cands, "Compressive sampling," in *Proceedings of the Int. Congress of Mathematics*, Madrid, Spain, 2006, pp. 1433–1452.

[79] X. Li and M. T. Orchard, "Edge-direted prediction for lossless compression of natural images," *IEEE Transactions on Image Processing*, vol. 10, no. 6, pp. 813–817, June 2001.

[80] D. Santa-Cruz., R. Grosbois, and T. Ebrahimi, "JPEG 2000 performance evaluation and assessment," *Signal Processing: Image Communication*, vol. 1, no. 17, pp. 113–130, 2002.

[81] X. Zhang, X. Wu, and F. Wu, "Image coding on quincunx lattice with adaptive lifting and interpolation," in *IEEE Data Compression Conference 2007*, Mar. 2007, pp. 193–202.

[82] S. D. Servetto, K. Ramchandran, V. Vaishampayan, and K. Nahrstedt, "Multiple description wavelet based image coding," *IEEE Trans. Image Processing*, vol. 9, no. 5, pp. 813–826, May 2000.

[83] C. Tian and S. S. Hemami, "A new class of multiple description scalar quantizer and its application to image coding," *IEEE Signal Processing Letter*, vol. 12, no. 4, pp. 329–332, Mar. 2007.

[84] J. Wang and J. Liang, "Filter banks for prediction-compensated multiple description coding," in *IEEE Data Compression Conf*, 2008, pp. 392–401.

[85] T. Tillo, M. Grangetto, and G. Olmo, "Multiple description image coding based on Lagrangian rate allocation," *IEEE Trans. Image Processing*, vol. 16, no. 3, pp. 673–683, March 2007.